PhD Thesis
Optimising the Target and Capture Sections of the Neutrino Factory

Ole Martin Hansen

University of Oslo & CERN

12th January 2016

Abstract

The Neutrino Factory is designed to produce an intense high energy neutrino beam from stored muons. The majority of the muons are obtained from the decay of pions, produced by a proton beam impinging on a free-flowing mercury-jet target and captured by a high magnetic field. It is important to capture a large fraction of the produced pions to maximize the intensity of the neutrino beam.

Various optimisation studies have been performed with the aim of maximising the muon influx to the accelerator and thus the neutrino beam intensity. The optimisation studies were performed with the use of Monte Carlo simulation tools.

The production of secondary particles, by interactions between the incoming proton beam and the mercury target, was optimised by varying the proton beam impact position and impact angles on the target. The proton beam and target interaction region was studied and showed to be off the central axis of the capture section in the baseline configuration. The off-centred interaction region resulted in off-centred secondary particles. A new proton beam definition was introduced to bring the secondary particle back on the central axis. The path length was increased by varying the proton beam impact position and impact angles on the target while keeping the production of secondary particles centred. The optimisations increased the muon influx to the accelerator. In addition shape fluctuations of the free-flowing mercury jet target was introduced and studied. The study showed only a small performance decrease.

The capture efficiency of the capture and tapering sections was studied by using alternative solenoid magnet geometries, alternative solenoid magnet configurations and therefore alternative magnetic field tapering variants to the baseline configuration. In addition an alternative shielding layout was proposed. The optimised capture and tapering sections increases the capture efficiency by using a simple three solenoid magnet configuration and a rapidly tapered magnetic field.

The Muon Ionisation Cooling Experiment (MICE) is an on-going proof of principle experiment. The MICE cooling channel is designed according to a feasibility study which assumes an incoming muon beam with symmetric momentum distribution. The MICE beam line delivers a muon beam with a skewed momentum distribution to the experiment. Therefore the MICE beam line was tuned by varying the magnetic field strength in the first dipole to provide a symmetrical momentum distribution to MICE. Both Monte Carlo simulations and data from MICE were used in the study. In addition the pion contamination levels of the MICE muon beams were studied by using results from Monte Carlo simulations.

Contents

Acknowledgements

Chapter 1

Introduction

This chapter contains an introduction to the Neutrino Factory (NF). The focus is on pion production, pion-decays to muons and pre-acceleration of the muon beam. Other parts are only briefly discussed. A very brief introduction of neutrino physics and components used for particle acceleration are provided to familiarise the reader with the notation. It is in no way complete and the reader is encouraged to read the referenced sources to gain insight into these subjects. References to recommended in-depth coverage of the relevant subjects can be found in the beginning of each section.

1.1 Neutrino Physics

Characterisation of the neutrinos is a major challenge for modern particle physics experiments [1]. Experiments have not been able to estimate all the parameters needed to accurately characterise the neutrinos, the challenge has been left for future neutrino facilities like a Neutrino Factory.

1.1.1 Neutrino Oscillations

Neutrinos are only affected by the weak nuclear force and gravity which makes them difficult to detect and study. Numerous experiments including reactor, accelerator, atmospheric and solar neutrino experiments have shown that neutrino flavours change when given sufficient time [1]. For this flavour change to happen the neutrinos have to be massive, the leptons have to mix and the flavour eigenstates must be super-positions

3

of the mass eigenstates. From quantum mechanics the equation

$$|\nu_\alpha> = \sum_i U^*_{\alpha i}|\nu_i>, \tag{1.1}$$

gives an $\alpha \times i$ sized matrix where $i = 1,2,3$ refers to the mass eigenstates and the neutrino flavours are $\alpha = e, \mu$ and τ. $U^*_{\alpha i}$ is the mass probability amplitude, written on matrix form in equation 1.2. This 3×3 matrix is called the Pontecorvo–Maki-Nakagawa–Sakata (PMNS) matrix or the mixing matrix.

$$U^*_{\alpha i} = \begin{bmatrix} c_{12}c_{13} & s_{12}c_{13} & s_{13}e^{-i\delta} \\ -s_{12}c_{23}-c_{12}s_{23}s_{13}e^{i\delta} & c_{12}c_{23}-s_{12}s_{23}s_{13}e^{i\delta} & s_{23}c_{13} \\ s_{12}s_{23}-c_{12}c_{23}s_{13}e^{i\delta} & -c_{12}s_{23}-s_{12}c_{23}s_{13}e^{i\delta} & c_{23}c_{13} \end{bmatrix} \begin{bmatrix} e^{\frac{i}{2}\alpha_1} & 0 & 0 \\ 0 & e^{\frac{i}{2}\alpha_2} & 0 \\ 0 & 0 & 1 \end{bmatrix}, \tag{1.2}$$

where $s_{ij} = \sin\theta_{ij}$, $c_{ij} = \cos\theta_{ij}$, θ_{ij} is the rotation angle and δ is the phase for charge-parity (CP) violation, i and j refer to their contributions to ν_e, $i \neq j$ and i,j$\in [1,3]$.

A solution to the Schrödinger equation gives a neutrino wave like properties. These properties come from the phase containing both position **x** and time t, thus changing the probability amplitude. The following equation gives a description of the dynamic system

$$|\nu_\alpha> = \sum_i e^{i(\mathbf{p_i}\cdot\mathbf{x}-E_i t)}U^*_{\alpha i}|\nu_i> . \tag{1.3}$$

Equation 1.4 gives the probability of neutrino flavour change in vacuum from $\alpha \to \beta$ at time t.

$$\begin{aligned} P([\alpha \to \beta],t) &= \left|< \nu_\alpha(0)|\nu_\beta(t) >\right|^2, \\ &= \delta_{\alpha\beta} - 4\sum_{i>j} Re(U^*_{\alpha i}U_{\beta i}U_{\alpha j}U^*_{\beta j})\sin^2\frac{\Delta m^2_{ij}L}{4E} \\ &+ 2\sum_{i>j} Im(U^*_{\alpha i}U_{\beta i}U_{\alpha j}U^*_{\beta j})\sin\frac{\Delta m^2_{ij}L}{2E}, \end{aligned} \tag{1.4}$$

where m_i is the neutrino mass for eigenstate i, $\Delta m^2_{ij} = m^2_i - m^2_j$, $L \approx t$ is the travelled length and E is the energy of the neutrino. The phase is responsible for the oscillation. The imaginary part is the CP asymmetry, if the imaginary part is zero no CP-violation takes place.

When dealing with only two neutrinos, which undergoes a neutrino flavour change, an approximate equation can be used which is easier to understand. The mixing matrix is

$$U = \begin{bmatrix} \cos\theta & \sin\theta \\ -\sin\theta & \cos\theta \end{bmatrix}, \tag{1.5}$$

where θ is the mixing angle. Thus the flavour eigenstates are expressed as a rotation of the mass eigenstates

$$
\begin{aligned}
|\nu_\alpha> &= \cos\theta|\nu_1> + \sin\theta|\nu_2>, \\
|\nu_\beta> &= -\sin\theta|\nu_1> + \cos\theta|\nu_2>.
\end{aligned} \tag{1.6}
$$

The probability of a neutrino flavour change is reduced to

$$
P(\alpha \to \beta|\alpha \neq \beta) = \sin^2(2\theta)\sin^2(\frac{\Delta m^2 L}{4E}), \tag{1.7}
$$

or written in SI-units

$$
P(\alpha \to \beta|\alpha \neq \beta) = \sin^2(2\theta)\sin^2(1.27\frac{\Delta m^2 L}{E}), \tag{1.8}
$$

where L is the distance between the neutrino source and the neutrino detector in km, E is the neutrino energy in GeV and Δm^2 is the mass squared difference in eV^2. In equation 1.8 the unit change came through the re-introduction of $\hbar$ and c which gives the constant 1.27. In figure 1.1 the oscillatory behaviour of the probability $P(\alpha \to \beta)$ for the two neutrino flavour approximation is shown.

1.1.2 Experimental results

Several experiments have contributed to increase the understanding of Neutrino physics. These involve reactor, accelerator, atmospheric and solar neutrino experiments, all details can be found in [2]. At the time of writing the best-fit parameter values are summarised in table 1.1.

The coming and on-going neutrino experiments are trying to fill the gap and determine the remaining parameters, namely:
- The Dirac CP-violation δ.
- The sign of Δm_{31}^2.
- The sign and value of Δm_{32}^2, and finally perform,
- High precision measurements of all mixing parameters.
The recent and encouraging determination of a non-zero θ_{13} allows for the determination of the charge-parity violation phase δ in future facilities like the NF.
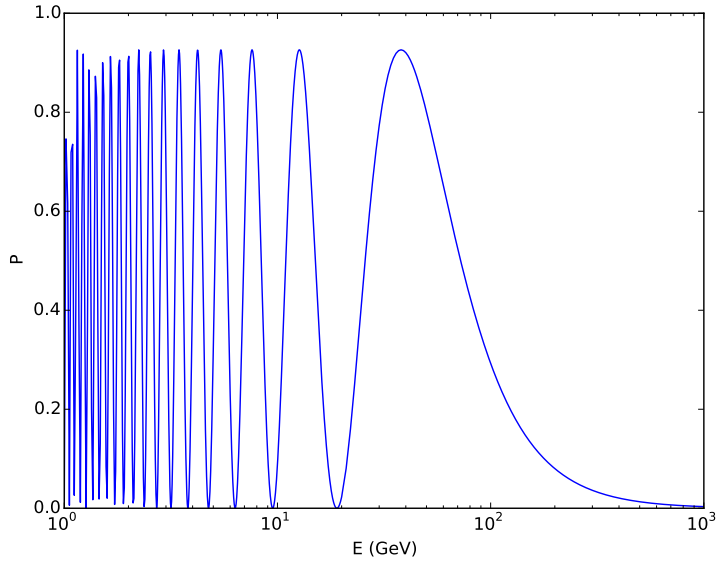
Figure 1.1: Oscillating probability $P(\alpha \to \beta)$ for two neutrino flavours when varying E. The parameters has the values $\Delta m = 2.35 \times 10^{-3}$ eV^2, L=2000 km and $\sin^2(2\theta) = 0.93$.

Table 1.1: Best-fit values for neutrino mixing. The hyphen means the value is unknown and the absolute value is used for Δm^2_{31} because of the mass hierarchy problem.

Parameter	Value $\pm 1\sigma$
$\sin^2 \theta_{12}$	$0.312^{+0.018}_{-0.015}$
$\sin^2 \theta_{13}$	$0.0251^{+0.007}_{-0.008}$
$\sin^2 \theta_{23}$	$0.42^{+0.08}_{-0.03}$
Δm^2_{21} [eV^2]	$7.58^{+0.22}_{-0.26} \times 10^{-5}$
Δm^2_{32} [eV^2]	-
$|\Delta m^2_{31}|$ [eV^2]	$2.35^{+0.12}_{-0.09} \times 10^{-3}$
δ	-

1.2 The Neutrino Factory

This section is based on the documents [3], [4] and [5] which contain detailed descriptions of the Neutrino Factory.

The Neutrino Factory (NF) is proposed as a future high intensity, high energy neutrino source to probe the remaining (and known) parameters in the mixing matrix U. The mixing matrix parameters are charge-parity (CP) invariance violation parameter δ, the mass weight m_i and the mass hierarchy (MH) through Δm_{ij}^2 (and the mixing angles θ_{ij}) as described in section 1.1.

The known parameters are probed for increased precision and the unknown parameters to obtain a descriptive mathematical model of the neutrino oscillation phenomenon and possibly new physics. New physics would mean for example non-unitarity of the mixing matrix and sterile neutrinos, non-standard matter effects and non-standard charged current interactions. The NF is, at the present time, the best option which is sensitive to all these parameters and new physics. More details follow in 1.2.3 where the NF is compared with other neutrino facilities.

1.2.1 Accelerator layout

A thorough description of the NF front-end which begins at the pion capture and ends after pre-acceleration follows in subsection 1.2.2.

The baseline of the NF is shown in figure 1.2. It consists of a high power *proton driver* delivering short bunches of protons (1-3 ns) to the *target* section, where the protons bombard a heavy metal target for production of secondary particles.

The (charged) secondary particles are captured by a high magnetic field in the *capture* section, before the magnetic field is gradually decreased or tapered from 20 T to 1.5 T, over a distance of approximately 15 m. This 15 m magnetic field *tapering* region contains a series of solenoids, consistently weakening downstream, to capture both sign charged particles. Additionally the tapering reduces the beam's transverse divergence while increasing the beam phase-space volume and the longitudinal momentum p_z. All this stems from the fringe field effect between the solenoids, discussed more in subsection 1.3.2.

After the tapering section the pions are left to decay to muons in the $B_d = 1.5$ T *drift* section. In the drift section the pions/muons also develop an energy-position correlation because of the beam's large energy spread, meaning faster particles ahead and slower particles at the tale.

Downstream of the drift section the beam enters the pre-accelerator containing the *buncher*, the *rotator* and the *cooler* sections in succession. The pre-accelerator manip-
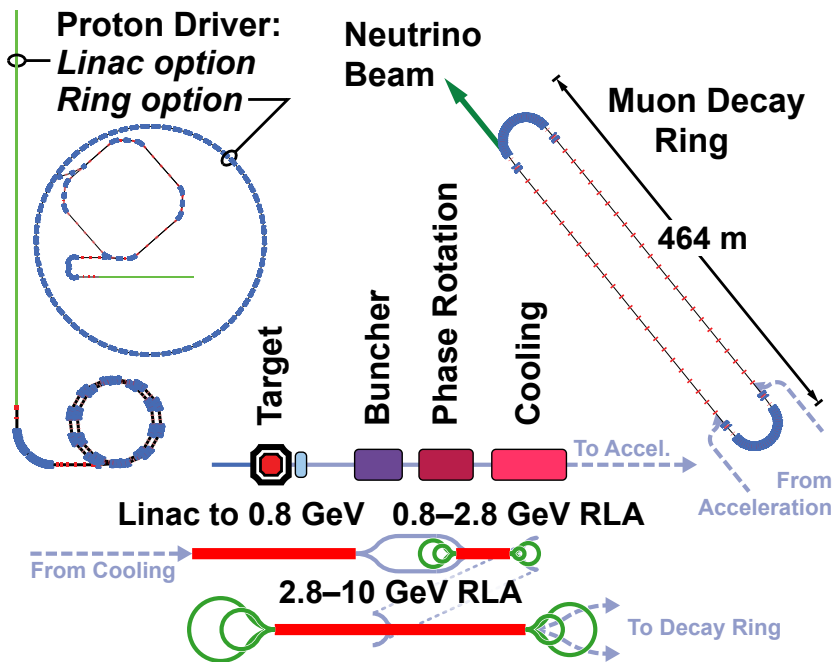
Figure 1.2: The Neutrino Factory layout [6].

ulates the beam phase-space with RF-cavities while focussing the beam with a series of solenoids.

In the buncher the continuous and large energy-position spread is transformed to a train of muon bunches. After the buncher the low (high) energy muons lagging behind (in front) are accelerated (decelerated) in the rotator such that the bunches have the same mean energy. The beam's divergence is then reduced by low Z-material inserts in between the RF-cavities in the cooler. The beam loses energy when it traverses the inserts, reducing the transverse p_T and longitudinal momentum p_z. The longitudinal momentum p_z is restored by acceleration, thus decreasing the beam divergence gradually over 130 cavities. The beam leaves the pre-accelerator with a mono-chromatic mean-momentum ready for acceleration.

Muon acceleration of the bunched, mono-chromatic, low emittance ε beam bunches is done in several acceleration stages up to a final energy $E = 10$ GeV. In the linear accelerator (linac) the muons are accelerated to $E = 0.8$ GeV, then further acceleration follows in two Recirculating Linear Accelerators (RLA). The first RLA accelerates muons to an energy of $E = 2.8$ GeV and the second RLA accelerates muons to an energy $E = 10$ GeV.

Once accelerated the muons are injected into a race-track shaped storage ring. The storage ring has two long straight sections pointing in the direction of the far and near detectors. The high energy muons decay along the long straight sections to neutrinos,

$$\mu^+ \rightarrow e^+ + \nu_e + \overline{\nu_\mu}, \tag{1.9}$$
$$\mu^- \rightarrow e^- + \overline{\nu_e} + \nu_\mu, \tag{1.10}$$

and travel in approximately the same direction as their parent muons due to the Lorentz boost; towards the detectors. The current baseline layout has two near detectors and one far detector. The near detectors are located at each end of the straight sections of the storage ring, one for each polarity. The near detectors are placed 100 m from the end of the straight sections and the far detector is placed 2000 km from the end of the straight sections [7].

The present baseline foresees 10^{21} muon decays per year, putting constraints on the muon source and the proceeding muon transport. The muon source is pion decays, thus the performance of pion production and pion capture are vital to achieve this goal.

1.2.2 The Neutrino Factory front-end

A detailed description of the NF front-end follows. It contains the target, the capture, the taper, the drift, the buncher, the rotator and the cooling sections.

The Target, Pion Capture and Magnetic Field tapering

The target is a circulating free-flowing mercury-jet embedded in a high magnetic field. A nozzle controls the direction and the dimension of the jet such that it crosses the NF central z-axis with an angle θ_T. The nozzle controls the target radius $r_T \approx 5$ mm at the defined *target centre* position $(x, y, z) = (0, 0, -375)$ mm and makes sure the mercury flows to the mercury pool for re-circulation as shown in figure 1.3. The feasibility of
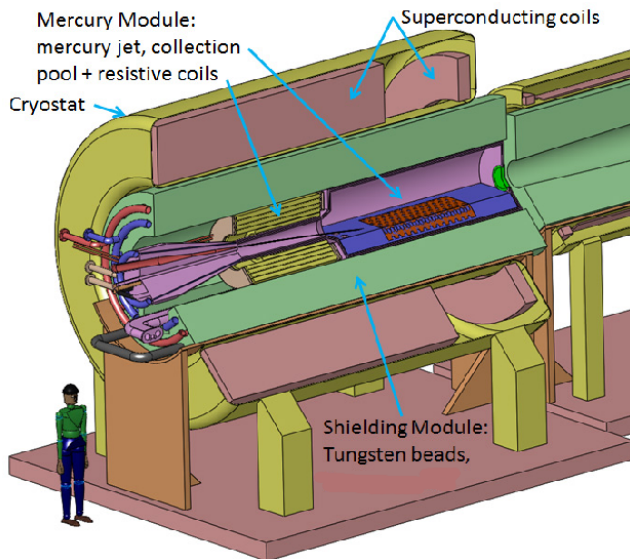
Figure 1.3: The NF target and capture layout, showing the normal conducting magnets, the SC magnets, the Hg-collection pool/beam dump, the shielding, the Hg-jet nozzle, the proton beam and the beam pipe [8].

having a 4 MW proton beam impinging on a free-flowing mercury-jet target in a high magnetic field was successfully proven by the MERIT experiment at the CERN PS [9].

The capture section consists of superconducting (SC) solenoids and three normal conducting coils producing a maximum magnetic field of $\mathbf{B_c} = 20$ T, where the vector component B_z points parallel to the central axis. Figure 1.4 shows the on-axis magnetic field for the Feasibility Study 2 (ST2) and the Study 2a (ST2a) set-ups [4]. ST2 is an end-to-end study of the Neutrino Factory complex and the ST2a is a follow-up study of the capture section of the Neutrino Factory proposing an improved magnet set-up. In

this thesis the capture sections of the ST2 and ST2a are used. The peak field is at the target centre, where the beam-target interaction or particle production region is located. From the target centre and downstream the field is adiabatically tapered.
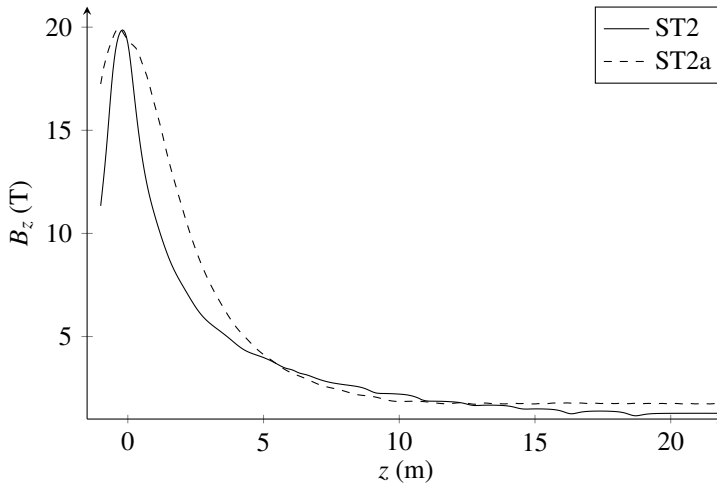
Figure 1.4: The ST2a and ST2 on-axis magnetic field B_z with respect to z.

Radiation protection of the SC solenoids is a major engineering challenge due to the 4 MW proton beam power. The current baseline shielding material is tungsten-carbide and the material is cooled by water. The geometry of the cylindrical inner shielding shown in figure 1.3, protects the large capture SC solenoid from radiation. The shielding thickness is 555 mm.

The beam pipe has the shape of a cone with increasing radius from $r_{bp1} = 75$ mm to $r_{bp2} = 300$ mm over the length of the tapering[1]. Figure 1.5 shows the beam pipe cone for the slowly growing beam in the tapered magnetic field.

---

[1]Higher outer radii have been proposed and the SC solenoid shielding configuration research is still ongoing. If not properly shielded the SC solenoid will receive heavy damage, limiting its life time and/or making it quench.

Figure 1.5: The ST2a beam pipe cone of the magnetic field tapering section and the straight beam pipe in the drift section where the magnetic field is constant.

Figure 1.6 shows the beam pipe cone for the slowly growing beam in the tapered magnetic field and the geometry of the solenoid magnets producing the tapered magnetic field. The shielding is between the beam pipe and the SC solenoids.
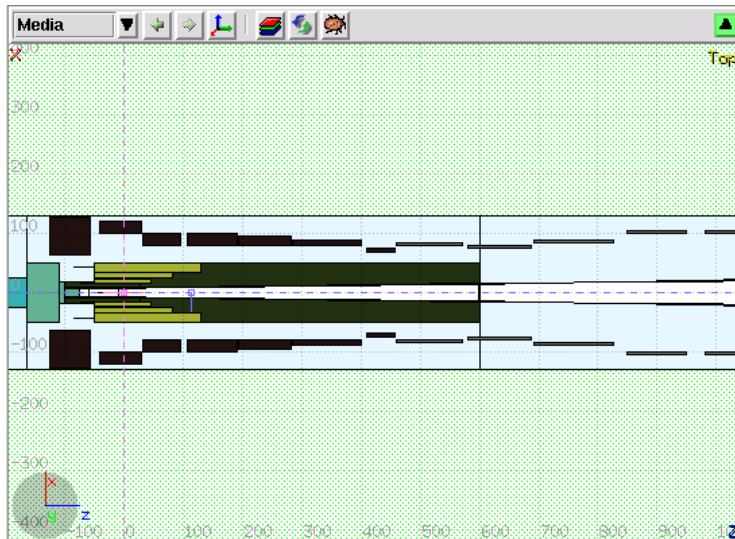
Figure 1.6: A vertical cut of the ST2a configuration including the SC solenoids, the normal resistive coils, the beam pipe and the shielding. The picture is taken from the implementation of the ST2a configuration in *flair*, a FLUKA interface viewer [10].

A high energy proton beam $E_b = 5 - 15$ GeV impinges on the mercury-jet target producing a shower of secondary particles; most particles hit the shielding and are dissipated around the beam-target interaction and peak field region. The beam pipe radius limits the helix radius of the secondary particles and thus the transverse momentum of the particles transported downstream in the NF.

The Drift

The series of SC solenoids in the drift section, have a constant magnetic field strength of 1.5 T corresponding to the tapering end and the buncher beginning.

Pions decay to muons and develop a position-energy correlation necessary for making a train of bunches in the buncher section. This correlation depends on the length between the particle production and the buncher. A short (long) drift leaves less (more) time for the pions to decay, but a denser (sparser) muon beam, see figure 1.7. Simulations were done with the monte carlo simulation tool G4beamline (G4BL) [11] based on Geant4 [12]. The thicker banana-shaped regions, lower left corner, hold most of
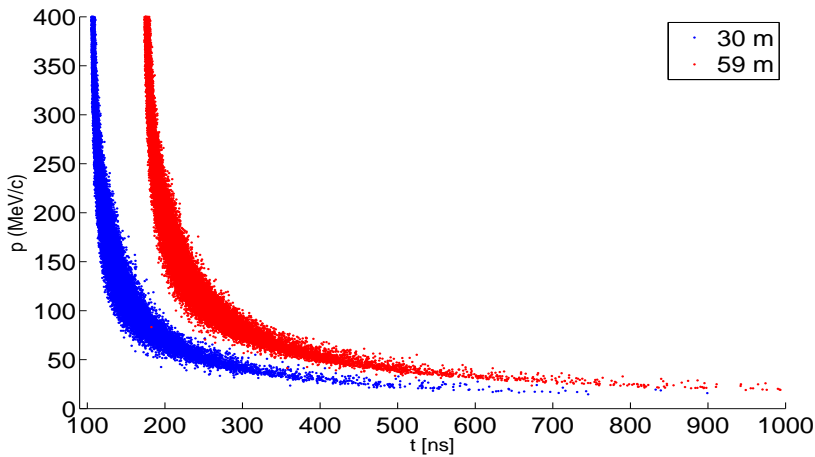
Figure 1.7: Scatter plot of muon momentum p versus time t with different drift section lengths $L_{D1} = 30$ m (blue) and $L_{D2} = 59$ m (red).

the surviving muons. The tale is longer at 59 m than at 30 m, indicating that low momentum muons are lagging more and more behind. A longer drift section gives a sparser muon beam.

The Buncher

The buncher is the first section which manipulates the muon phase-space using RF cavities. The buncher consists of 37 cavities for an overall length of $L_B = 33$. The cavities are 0.4-0.45 m long and are placed in 0.75 m long cells. Each cavity operates

in a focussing magnetic field $B = 1.5$ T made by a series of solenoid magnets over the whole length of the buncher.

The buncher splits the continuous beam into a train of densely packed muon bunches. Dense bunches are created by accelerating (decelerating) the low (high) energy muons in the kinetic energy interval $E_k \in [50, 400]$ MeV with the intent to provide monochromatic bunches. The buncher contains 37 cavities with 13 decreasing RF frequency-steps $f_{RF} \in [319.6, 233.6]$ MHz. The decreasing RF frequencies are synchronous with the particles in the beam. A linearly increasing gradient $V_{RF} \in [4, 7.5]$ MV/m allows a pseudo-adiabatic formation of bunches, forming a train of length less than 80 m.

Figure 1.8 shows the bunched beam at the buncher end. The buncher discriminates
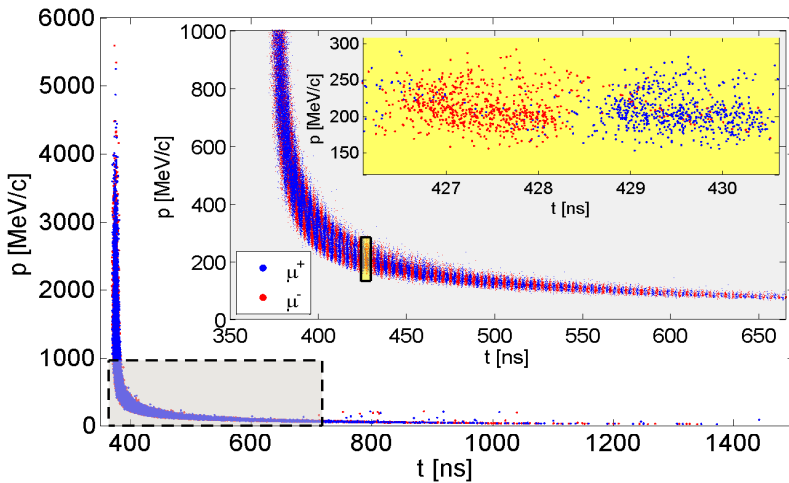
Figure 1.8: Muon beam at the end of the buncher. The blue (μ^+) and red (μ^-) scatter-plots show the particle species separated in time (space). High energy muons are not bunched properly. The grey inset shows the adjacent negative and positive bunches clearer. The yellow frame shows the profile of the micro bunches.

between the positive and negative muons and separates them, making interleaved single species bunches.

The Rotator

The rotator ensures the tail bunch and the head bunch have the same momentum at the rotator end. The bunched beam enters the rotator where the transition RF frequencies are matched. The RF cavities in the rotator are slightly out of phase such that the bunches ahead (behind) experience deceleration (acceleration). The section name comes from the rotation in the phase-momentum space giving the same mean-energy bunch train shown in figure 1.9.
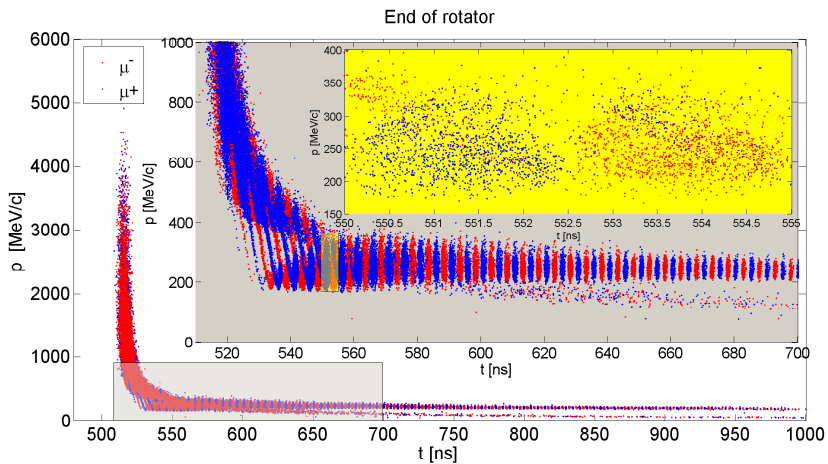
Figure 1.9: The muon beam outflux of the rotator. The blue (μ^+) and red (μ^-) scatterplots show how the particle species are separated in time. The lower momentum muon bunches have been accelerated to the same energy as the leading bunch. The grey inset shows the adjacent negative and positive bunches clearer. The yellow frame shows the profile of the micro bunches.

The section is $L_R = 42$ m long and contains a total of 56 cavities. The cavities are 0.5 m long and placed in cells of 0.75 m. The RF frequency is in the interval $f_{RF} \in [230.2, 202.3]$ MHz, grouped in 15 frequencies decreasing along the rotator, all cavities have a gradient of 12 MV/m. The bunches are accelerated to the momentum $p_0 \approx 233$ MeV/c.

The Cooler

The short muon life time of 2.2 μs means rapid cooling is needed. Muon cooling is
a technical challenge still remaining to be proven. A proof-of-principle experiment is
under work at Rutherford Appleton Laboratory (RAL) in the UK [13]. See section 4.1
for more details on ionisation cooling and its principles.

50 cells occupy the cooling section. Each cell contains 4 absorbers, one cavity and
two solenoids with a cell length of 1.5 m giving a total section-length of $L_c = 75$ m.
The RF-frequency is set to match the preceding rotator-end RF-frequency of 201 MHz
and the gradient is constant $V_{RF} \approx 10$ MV/m. Figure 1.10 shows the time-momentum
space after the cooler.
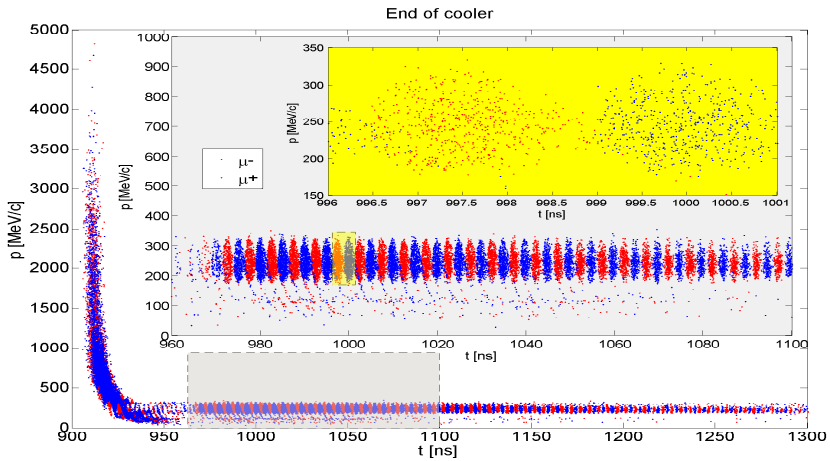

Figure 1.10: The muon beam at the cooler end. The blue (μ^+) and red (μ^-) scatter-plots
show the particle species separated in time (and space). The grey inset figure shows the
lower left rectangular grey area to see the adjacent negative and positive bunches. On a
smaller scale one can see the profile of the micro bunches shown in the yellow frame.

Opposite polarity solenoids produce an alternating magnetic field with an amp-
litude of 2.8 T. These solenoids focus the large sized beam on to the absorbers where
the beam loses energy through ionisation. At the same time multiple scattering will
deflect particles and increase the beam size (heating). RF cavities accelerate muons to
restore the lost longitudinal momentum, the transverse momentum is not restored, thus
reducing the divergence at each absorber.

The two opposing effects have been studied to make sure cooling (decreasing phase-space) is dominant, meaning suppression of multiple scattering and increasing energy loss. Low-Z liquid hydrogen is a candidate for the absorber material.

1.2.3 Performance of the Neutrino Factory

Several alternatives to the Neutrino Factory have been proposed. In this subsection the performance of the Neutrino Factory is compared with super beams alternatives.

In figure 1.11 the NF is compared with several neutrino super beam facilities, specifically LBNE, LBNO, T2HK and ESSνSB. Detailed explanation of each set-up can be found in [14] where the ultimate luminosity of all experiments is assumed and the running time for each experiment is set to 10 years. The NF has the highest parameter precision of CP-violation $\Delta\delta \sim 3\text{-}7°$ at 1σ. The expanded super beam experiments T2HK+NuSTORM has the second highest precision of $\Delta\delta \sim 6\text{-}16°$ and Daedalus+T2HK has the third highest precision of $\Delta\delta \sim 7\text{-}11°$. The super beams can reach a precision of $\Delta\delta \sim 8\text{-}17°$. The NF also has a θ_{13} accuracy of <3 % at 1σ [15]. The NF is the ultimate neutrino facility.

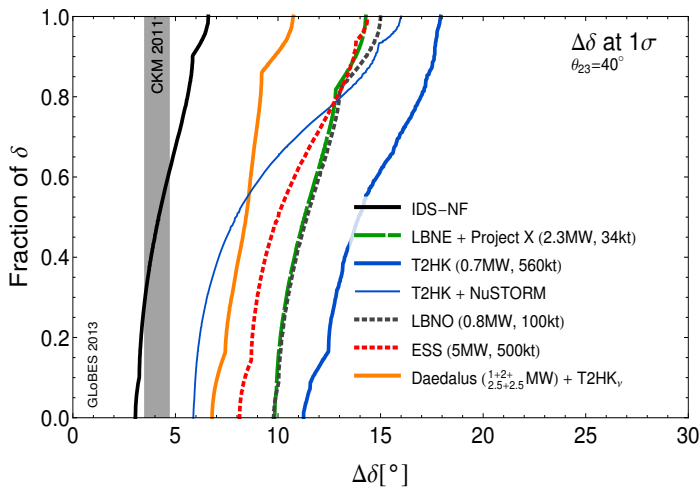Figure 1.11: Expected sensitivity of a measurement of δ at various alternative experiments. The fraction of the possible values of δ for which a given precision can be reached at 1σ is shown. The NF has the highest sensitivity.

1.2.4   Summary

Currently there are several "discoveries" available for the (future) neutrino programme. The mass hierarchy and CP-violation are yet open challenges. If $e^{i\delta}$ turns out to be different than one, leptonic CP-violation could explain parts of the observed asymmetry of matter/anti-matter.

Additionally the nature of the neutrinos and the unitarity of the mixing matrix are unknowns. Neutrinos could be Dirac or Majorana particles and in the case of non-unitarity additional neutrinos can be hypothesised.

The Neutrino Factory uses primary protons bombarding a free-flowing mercury-jet target for the production of the secondary pions. The pions then decay to muons which are accelerated and stored. The neutrinos are then obtained from the circulating muons in the storage ring.

The Neutrino Factory is the ultimate neutrino facility, providing better parameter sensitivities than more conventional alternatives. Ionisation cooling is an integer part of the NF, but the principle has never been proven.

1.3   Technical components of the Neutrino Factory

The important components of the Neutrino Factory relevant for this thesis, are radio frequency cavities and solenoids. Solenoids are used to produce the magnetic field in the capture, the tapering and the drift sections. The performance of the capture, the tapering and the drift sections is optimised by varying the magnetic field strength and shape in these sections. The radio frequency cavities are used to control the particle energy in the pre-accelerator, the accelerator and the storage ring. These components are briefly discussed in this section.

1.3.1   Radio Frequency Cavities

The Radio Frequency cavities are used to accelerate (decelerate) charged particles with an alternating electric field, see figure 1.12 where the first RF-cavity made for the Muon Ionisation Cooling Experiment (MICE) is shown.

The phase of the Radio-Frequency (RF) cavity is finely tuned to a reference particle's momentum p_{ref} to accelerate (decelerate) particles within a chosen momentum spread $p_{ref} \pm \Delta p$. The RF-cavity gives the charged particles an energy 'kick'. Usually several cavities are operating in series where the phase is tuned to match the step-wise energy increase from each 'kick' received.
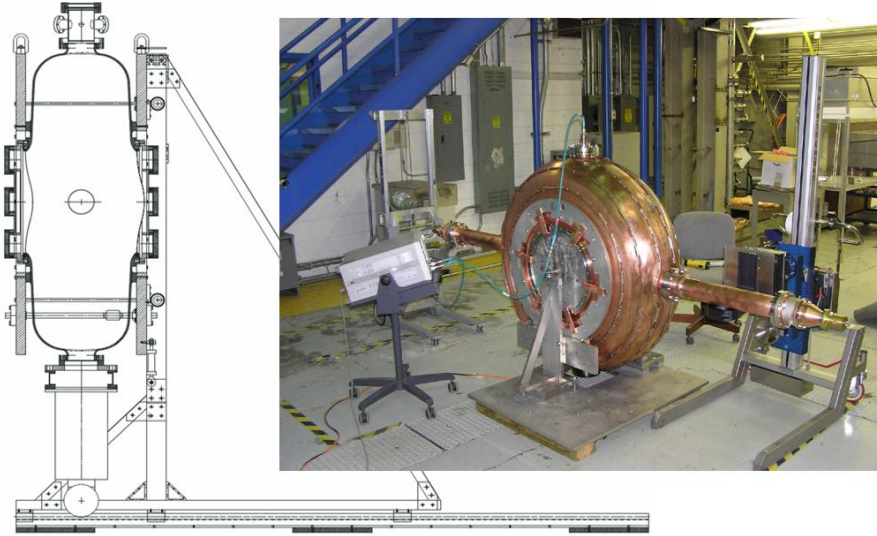
Figure 1.12: Example RF-cavity from MICE, both a cartoon and the real cavity[16].

1.3.2 Solenoids

A solenoid is a cylindrical device consisting of conductors wound into the shape of a helix. Inside the helix it produces a magnetic field pointing along the central axis. The field strength and direction depend on the electrical current strength and polarisation. Solenoids are weakly focussing and an integral part of the Neutrino Factory design.

When a charged particle with transverse and longitudinal velocity (v_T and v_z) components travels inside the solenoid with magnetic field $\mathbf{B} \approx B_z$ (the z-axis points parallel to the centre-line of the solenoid), the charged particle is bent by the magnetic field forming a helical trajectory, assuming the electric field $\mathbf{E} \approx 0$.

Close to the solenoid endpoints the magnetic field is divergent and fringe fields develop a transverse magnetic field component B_T while B_z decreases as shown in figure 1.13. This will obviously influence the particle trajectory, for example by increasing (decreasing) the helix radius r_h, and the velocity $\mathbf{v}$ depending on the vector field $\mathbf{B}$. The Neutrino Factory takes advantage of the solenoid fringe-field effect to change the beam divergence and the beam size, see section 1.2.
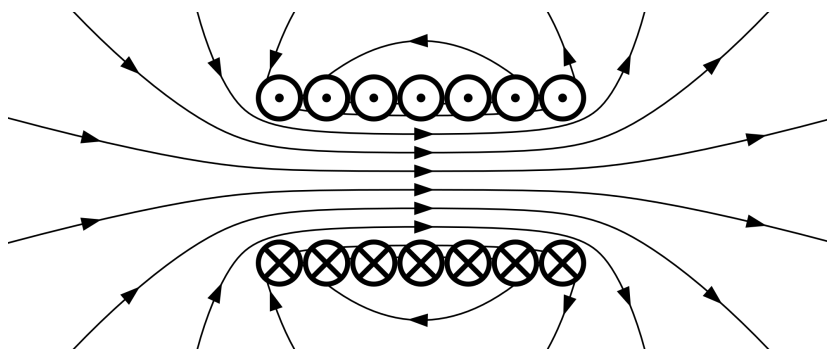
Figure 1.13: Cartoon of the magnetic field lines of a solenoid under the influence of an electric current I. Showing the electric current polarisation and the resulting magnetic field direction.

Chapter 2

Neutrino Factory Target Optimisation

The production and capture of pions are crucial to maintain the necessary muon density to reach the goal of $\sim 10^{21}$ muon decays/year. This chapter contains optimisation studies aimed at increasing the muon influx to the buncher to increase the overall muon density. The overall muon density is increased by optimising the beam-target interactions. The main results are published in [17]. In addition it introduces acceptance cuts based on the acceptance range of the accelerator.

The focus is the optimisation of pion production in the target section of the Neutrino Factory. Pion production is optimised by varying the incoming proton beam's entry position and entry angles on the target, thus introducing variations on pion production.

A free-flowing mercury jet target may be distorted by a magnetic field, changing the shape from a circular cylinder to an elliptic cylinder [18]. In addition the mercury jet's radius has been reported to fluctuate along the jet [9]. Both may influence the production of pions. These scenarios are studied and the findings are reported.

The NF proton driver delivers a short pulsed proton beam at energies between 5-15 GeV. The proton beam frequency is $f_{pb} \approx 50$ Hz amounting to a power of $P \approx 4$ MW at a proton energy of 8 GeV for 3.125×10^{15} protons/s. The high beam power makes the target material subject to heavy stresses, where 20% of the beam power is dissipated in the mercury jet. The remaining power is dissipated in the mercury-pool beam-dump and target surroundings [19]. Studies have shown that a stationary target rod is unable to dissipate the expected dissipated power $P_{Hg} \approx 0.8$ MW and is unsuitable. A recirculating target of cooled heavy metal providing a "new" and cooled target between beam

pulses, as the free-flowing mercury-jet option, is the current baseline. Other target options are also under investigation, for example a fluidised granular tungsten target. The fluidised granular target can be recirculating and shaped as a powder jet, similar to a mercury-jet [20]. A disadvantage of using mercury is the handling constraints and requirements. A granular tungsten target would have less stringent handling requirements [21].

Optimisation studies demand frequent performance analyses, comparing a fixed system (baseline) with one or more alternative systems. The target, capture and tapering sections from *Feasibility Study 2a* (ST2a) will here be used as the baseline set-up [4]. Feasibility Study 2 (ST2) is an end-to-end study of the Neutrino Factory complex and ST2a is a follow-up study of the capture section of the Neutrino Factory proposing an improved magnet set-up [5]. The ST2a capture and target, taper and drift sections' geometries are listed in table 2.1.

The NF design is under constant development. Important improvements and changes have been introduced since the release of the ST2a; these are not included. However, the current IDS baseline front-end system still remains very similar to the ST2a. Recent changes include a chicane and a proton absorber in the drift section. The chicane removes undesired particles from the beam and the absorber removes remaining non-interacted protons. Also some geometry parameters have changed slightly, e.g. section lengths, tuning of the RF-frequency, while the target and cooling sections remain largely the same. Nevertheless, these changes are not expected to change the main results presented. Current baseline simulations which include the proton absorber and the chicane show only a minor muon flux decrease compared to the ST2 [7].

2.1   Geometry of the Capture, Taper and Drift sections

The ST2a capture, tapering and drift geometries and the positioning of the components are listed in table 2.1 and shown in figure 2.1 [22]. The capture, taper and drift sections contain 93 solenoids (in yellow) and a target (not visible, inside the solenoids), the beam pipe is not included. The accelerated proton beam comes from the left (in figure 2.1) aimed at the target for production of particles. The z-axis points down the centre line of the NF.

The beam pipe (green), as shown in figure 2.2, is placed inside the solenoids. The target (red) and the proton beam (blue) are shown in the inset, the target is located on the left and narrowest part of the beam pipe. The target is a $L_T = 300$ mm cylinder

Table 2.1: Component placements of the ST2a lattice. SC is short for Super Conductor, Fe and Cu refers to the material of the normal conducting magnets. *z-position* is the start position of the component and *Radius* is the inner radius of the component. A field-map of the magnetic field was provided and used in simulations, the current densities listed were not implemented in G4BL.

| No. (Type)	z-position (m)	Length (m)	Radius (m)	Thickness (m)	Current density(A/mm^2)
Target and Capture section					
1 (SC)	-1.252	0.683	0.640	0.640	52.87
2 (Fe)	-0.846	0.326	0.430	0.010	29.29
3 (Fe)	-0.726	0.206	0.150	0.010	46.36
4 (Cu)	-0.500	0.948	0.160	0.070	16.52
5 (Cu)	-0.500	1.320	0.240	0.100	19.69
6 (Cu)	-0.500	1.791	0.350	0.160	20.96
7 (SC)	-0.400	0.690	1.000	0.210	26.23
8 (SC)	0.310	0.640	0.800	0.210	52.95
9 (SC)	1.070	0.850	0.800	0.210	63.02
10 (SC)	1.940	0.880	0.800	0.150	47.09
11 (SC)	2.840	1.160	0.800	0.090	56.74
12 (SC)	4.100	0.470	0.673	0.070	45.97
13 (SC)	4.590	1.127	0.800	0.050	65.18
14 (SC)	5.803	1.070	0.740	0.050	44.00
15 (SC)	6.910	1.360	0.849	0.050	39.77
16 (SC)	8.500	0.990	1.000	0.050	45.69
17 (SC)	9.800	1.900	1.000	0.050	32.01
18 (SC)	12.180	0.470	1.000	0.100	42.96
Matching section **1**					
19 (SC)	13.000	0.360	0.430	0.100	12.63
20 (SC)	13.500	0.360	0.430	0.100	16.74
21 (SC)	14.000	0.360	0.430	0.100	19.42
22 (SC)	14.500	0.360	0.430	0.100	19.06
23 (SC)	15.000	0.360	0.430	0.100	18.84
Drift section 1					
24–71 (SC)	15.5–39.0	0.360	0.430	0.100	19.22
Matching section					
72 (SC)	39.500	0.360	0.430	0.100	18.76
73 (SC)	39.960	0.355	0.450	0.100	20.39
74 (SC)	40.450	0.364	0.377	0.100	18.67
75 (SC)	40.960	0.389	0.352	0.100	19.16
76 (SC)	41.500	0.360	0.320	0.100	18.91
Drift section 2					
77–93 (SC)	42.000–50.000	0.360	0.320	0.100	19.00
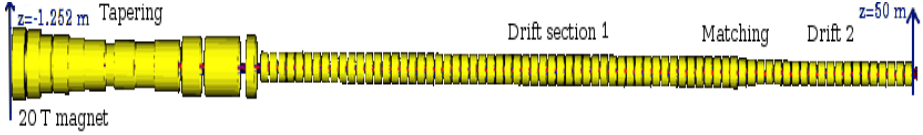
Figure 2.1: Visualisation of the ST2a setup implemented in G4BL, image from G4BL viewer.
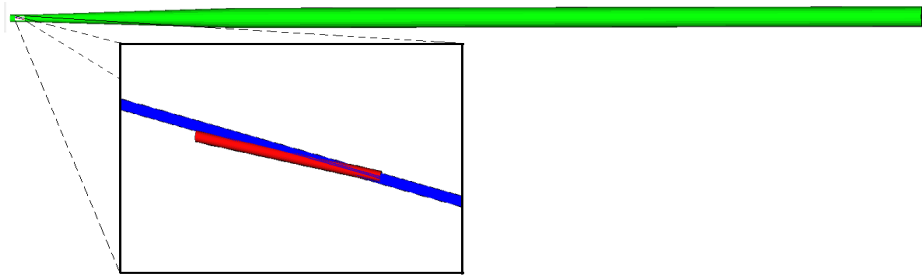
Figure 2.2: The beam pipe (green) and the target (red) and the proton beam (blue) are shown in the inset.

placed at $z = -375$ mm. The target is tilted by an angle θ_T around the x-axis. For visualisation purposes all interactions in G4BL are turned off and the proton beam continues undisturbed though the target. The proton beam enters the target on the upper part of the upstream side and exits at the lower-downstream side. For optimisation studies this layout, ST2a, will be used as reference.

The beam pipe radius is $r_c^{bp} = 75$ mm at the target centre and increases along the tapering until it reaches it maximum radius $r_d^{bp} = 254$ mm. The increasing beam pipe radius is implemented as a cone with boundary conditions equal to radii r_c^{bp} and r_d^{bp} when z is in the interval $z \in [0, 11.5]$ m.

The target rotation angle is $\theta_T = 96.68$ mrad and the angle between beam and target is $\theta_{BT} = 30$ mrad. The target is modeled in G4BL as a $L_T = 300$ mm long cylinder slab of mercury with a radius of $r_T = 5$ mm, using a target length which is two interaction lengths $L_T \approx 2\lambda_I$. The target centre is placed at $z = -375$ mm. For more details on the beam definition see [23].

2.2 Defining the figure of merit

The efficiency of a proton beam-target interaction is the measured pion outflux. A choice for efficiency estimation of the joint proton beam-target interaction, pion capture and the magnetic field tapering could be at the tapering end. However, at that point the muon beam is highly contaminated by pions. A better alternative is to measure the muon influx to the Buncher at the downstream end of the drift section. The buncher, the rotator and the cooler prepares the muon beam for acceleration and is called the pre-accelerator.

2.2.1 Muon accelerator acceptance cuts

The particles travelling inside the beam pipe of the NF are restricted by the beam pipe radius r_{bp} in the transverse direction. The maximum radius r^{max} of a particle bent by a magnetic field is half that of the beam pipe radius $r^{max} \leq r_{bp}/2$. Particle accelerators steer and accelerate particles using electromagnetic fields. The momentum of a relativistic particle is

$$\mathbf{p} = \gamma m_0 \mathbf{v} = m\mathbf{v}, \tag{2.1}$$

where $\mathbf{v}$ is the velocity, $\gamma = 1/\sqrt{1 - \left(\frac{v}{c}\right)^2}$ and $m = \gamma m_0$ is the relativistic mass. The force $\mathbf{F}$ exerted on a particle can be found with the use of Newtons second law

$$\frac{d\mathbf{p}}{dt} = \mathbf{F}, \tag{2.2}$$

here $\mathbf{F}$ is the Lorentz force law on a charged point-like fast particle in a magnetic $\mathbf{B}$ and electric $\mathbf{E}$ field, giving

$$\gamma m_0 \frac{d\mathbf{v}}{dt} = q(\mathbf{v} \times \mathbf{B} + E), \tag{2.3}$$

where t is the time and q is the particle charge [24]. The maximum transverse momentum is thus determined by

$$p_T^{max} \leq \frac{eB_c r_{bp}}{2}, \tag{2.4}$$

where e is the electric charge and B_c is the capture magnetic field. The limiting parameters are the radius and the magnetic field. Using the parameters from the NF baseline configuration, $r_{bp} = 75$ mm and $B_c = 20$ T, a maximum transverse momentum $p_T^{max} \leq 225$ MeV/c is obtained.

The transverse momentum p_T distribution of the secondary particles downstream of the target at $z = -200$ mm is shown in figure 2.3. The particles with transverse
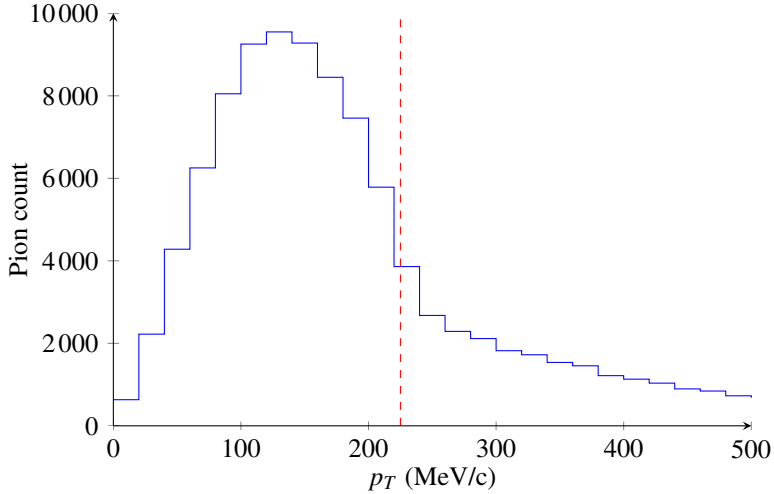
Figure 2.3: The histogram of the transverse momentum p_T at $z = -200$ mm. The vertical red line is p_T^{max}.

momentum $p_T > p_T^{max}$ are high energy particles with low divergence ($p_z >> p_T$) and a high probability of being lost either through scraping in the beam pipe or in the (pre-) accelerator.

The longitudinal momentum p_z spread downstream of the target is shown in figure 2.4. The energy spread ranges over three orders of magnitude, from a few MeV to approximately 7 GeV. The 8 GeV proton beam gives rise to the large energy spread producing particles limited by its own energy. Directly after the target the majority of the particles are pions which decay to muons while travelling further downstream. At 50 m (downstream of the target) most of the pions have decayed to muons.

The pre-accelerator and the accelerator put restrictions on the muon momentum p (pions entering the pre-accelerator are considered lost). Firstly the buncher is designed to capture muons in the kinetic energy range from 50 - 400 MeV and secondly the accelerator is designed to accelerate muons with a momentum p=233 MeV/c with a momentum acceptance of $\Delta p/p = 17\%$. Thus acceptance cuts must be defined to enable consistent performance comparisons.

Acceptance cuts can be defined in several ways. The following options were considered.
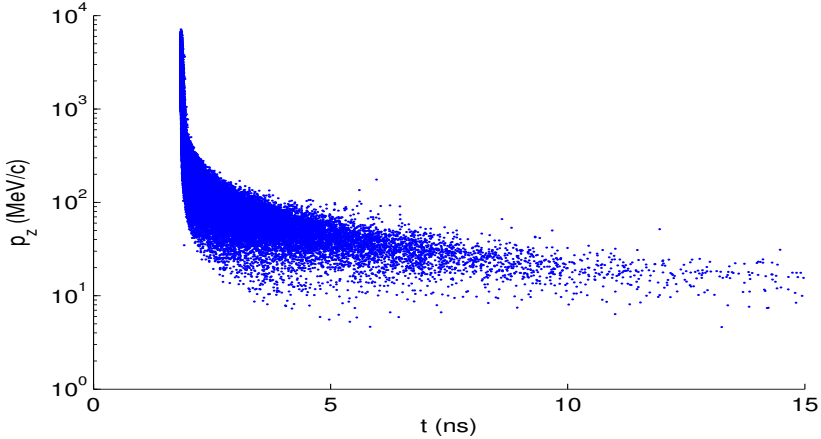
Figure 2.4: Scatterplot of the longitudinal momentum p_z versus time t at $z = -200$ mm.

1. *No cuts*: All particles counted. Higher particle influx at the buncher yields better performance.

2. *Energy cuts*: Applying an energy cut on the particle influx at the buncher. Acceptance cuts based on muons captured by the pre-accelerator.

3. *Momentum cut*: Applying momentum cuts before the buncher, based on the acceptance of the the pre-accelerator.

4. *Accelerator acceptance calculations by ecalc9.f* [25]: ecalc9.f is a module made for the simulation tool ICOOL [26]. It does particle by particle emittance ε calculations comparing them with reference particles. Predefined muon accelerator acceptance A_ε must be provided, specifically the longitudinal momentum p_z, the longitudinal A_L and transverse A_T phase space acceptance.

The first option was used for early studies because of its simplicity and ease of implementation in G4BL. Implementing only the target, capture and tapering sections in the simulation tool ensures short simulation time.

The second and third options are similar. For option 2 energy cuts $E \in [40, 180]$ MeV may be used [23]. For option 3 momentum cuts $p \in [80, 500]$ based on pre-accelerator acceptance provided in [27] can be used. They have the same simplicity,

ease of implementation and the same short simulation time as option 1, adding very little complexity with easy to use acceptance cuts.

The forth option is more complicated and involves implementing the whole front-end for simulation and use ecalc9.f on the outflux. It increases simulation time significantly, but it is the most accurate method.

A combination of the third and the forth option was adopted, where a simulation including the whole front-end in G4BL[1] was run and ecalc9.f used to find the muons accepted by the accelerator [28].

2.2.2   Simulations and the figure of merit

The muons are uniquely identified and labelled by the simulation program (G4BL). A number of virtual detectors are put along the front-end, detecting all particles crossing the detectors, such that the accepted muons (and rejected muons) given by ecalc9.f could be found along the front-end and analysed. A_ε is the acceptance cuts of the ecalc9.f routine which calculates the accepted muons. The acceptance cut input parameters for ecalc9.f is shown in table 2.2.

Table 2.2: The applied acceptance cuts A_ε for the emittance calculation routine ecalc9.f, consists of three cuts. A_L and A_T are the longitudinal and transverse emittances. p_z is the longitudinal momentum.

Acceptance (Unit)	Value
A_L (mm-rad)	150
A_T (mm-rad)	30
p_z (MeV/c)	100-300

A virtual detector placed at $z = 50$ m downstream of the target was chosen for analysis of the muons. This keeps simulation time low and the implementation is easy as in options 2 and 3. The muon influx to the pre-accelerator will therefore be calculated at $z = 50$ m.

The G4BL simulation output is given in time t, momentums p_x, p_y, p_z and positions x, y, z. To transform ecalc9.f cuts to match the G4BL output, the distribution of the accepted muons A_ε from ecalc9.f are analysed in time t, radius r and transverse momentum p_T at 50 m, this enables readily applied cuts. For example the time t-distribution for muons within acceptance cuts $\in A_\varepsilon$ is shown in figure 2.5 with the

---

[1]Thanks to Pavel Snopok for providing the front-end input files to G4BL.

corresponding survival ratio. The survival ratio is calculated by

$$R_S = \frac{\text{\# muons in } A_\varepsilon \text{ which are also within an interval } X \in [X_{min}, X_{max}]}{\text{\# muons in } A_\varepsilon}, \quad (2.5)$$

where X is one of the following t, p_T, p_z and r. The cuts are applied on one parameter, independently of the others. For example in figure 2.5

$$R_S = \frac{\text{\# muons in } A_\varepsilon \text{ which are within an interval } t \in [t_{min}, t_{max}]}{\text{\# muons in } A_\varepsilon} \approx 0.9,$$

when $t \in [t_{min}, t_{max}] = [160, 240]$ ns. The calculations of the survival ratio R_S^k for each parameter are done as follows

$$R_S^k = \frac{\sum\limits_{j}^{N} n_j}{\sum\limits_{i}^{N} n_i} \quad \text{for} \quad \begin{cases} j \subseteq i & \text{for} & X_i \in A_\varepsilon, \\ n_j = 1 & \text{if} & X_j^k \in [X_{min}, X_{max}^k], \\ n_j = 0 & \text{else}, \\ n_i = 1 & \text{if} & X_i \in A_\varepsilon, \\ n_i = 0 & \text{else}, \\ k \in [0, N_k], \end{cases}$$

where i is the muon index number, j is the index number for muons limited by ecalc9.f cuts, N_k is the number of cut intervals, k is the cut index number, N is the sum of all particles at $z = 50$ m, X can be any of the following t, p_T, p_z or r. $X_j^k \in [X_{min}, X_{max}^k]$ refers to the applied additional cuts.

To ensure rigorous testing of the accepted muons the survival ratio is set to $R_S \approx 0.9$ for finding the cuts at $z = 50$ m, meaning that 10% of the muons at the distribution tail are rejected. Thus cutting off the tail of each distribution for time t (see figure 2.5), radius r (see figure 2.7) and transverse momentum p_T (see figure 2.6) is done independently of each other. Using the survival ratio the cut value can readily be read off the graph. On time t both lower and upper cuts are applied, while the longitudinal momentum cuts are already given in table 2.2, $100 < p_z < 300$.

In figure 2.5 the time is analysed $X_j^k = t_j^k$ such that $X_j^k \in [X_{min}, X_{max}^k]$ becomes $t_j^k \in [t_{min}, t_{max}^k]$ where $t_{min} = 0$ ns and $t_{max}^k = [t_{max}^0 = 150, t_{max}^{N_k} = 350]$ ns.

As k increases so does the cut interval and the survival ratio. The same procedure could have been used to decide a lower time cut as well. Due to the fact that the longitudinal momentum p_z is already limited, the t-distribution is left-skewed with only one tail and a hard edge on the opposite side at $t = 170$ ns. A lower cut there
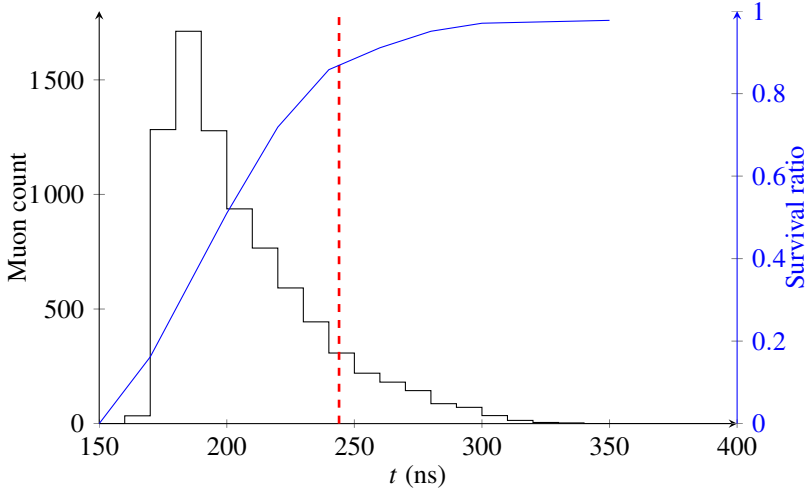
Figure 2.5: t-distribution histogram of accepted muons. The blue line is the survival ratio. The red line is the cut limit where $R_S^k \approx 0.9$.

would be sensitive to very small variations, therefore the lower time limit was set to $t_{min} = 160$ ns. Reading off the graph for the survival ratio $R_S^k \approx 0.9$ the upper time limit was set to $t_{max}^k = 240$ ns which gives $t_j = [160, 240]$ ns.

In figure 2.6 the transverse momentum is analysed $X_j^k = p_{Tj}^k$ such that $p_{Tj}^k \in [p_{Tmin}, p_{Tmax}^k]$ where $p_{Tmin} = 0$ MeV/c and $p_{Tmax}^k = [p_{Tmax}^0 = 30, p_{Tmax}^{N_k} = 100]$ MeV/c. As k increases so does the cut interval and the survival ratio. Reading off the graph for $R_S^k \approx 0.9$ the upper transverse momentum limit was set to $p_{Tmax}^k = 50$ MeV/c giving $p_{Tj} = [0, 50]$ MeV/c.

In figure 2.7 the radius is analysed $X_j^k = r_j^k$ such that $r_j^k \in [r_{min}, r_{max}^k]$ where $r_{min} = 0$ mm and $r_{max}^k = [r_{max}^0 = 150, r_{max}^{N_k} = 250]$ mm. As k increases so does the cut interval and the survival ratio. Reading off the graph for $R_S^k \approx 0.9$ the upper radius limit was set to $r_{max}^k = 200$ mm giving $r_j = [0, 200]$ mm.

Assuming an adiabatic tapering along the centre line of beam pipe such that the magnetic flux passing through cross-section $A_1 = \pi r_1^2$ at position 1 is approximately the same as the magnetic flux passing through cross-section $A_2 = \pi r_2^2$ at position 2, one
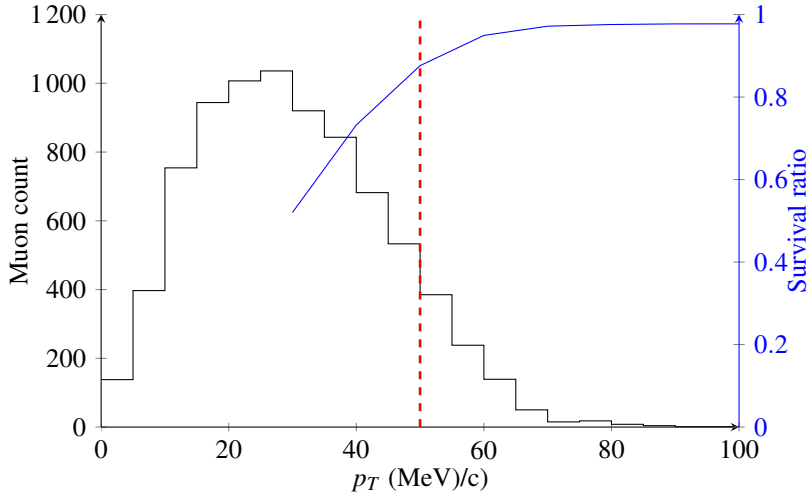
Figure 2.6: p_T-distribution histogram of accepted muons. The blue line is the survival ratio and the red line is the cut limit where $R_S^k \approx 0.9$.
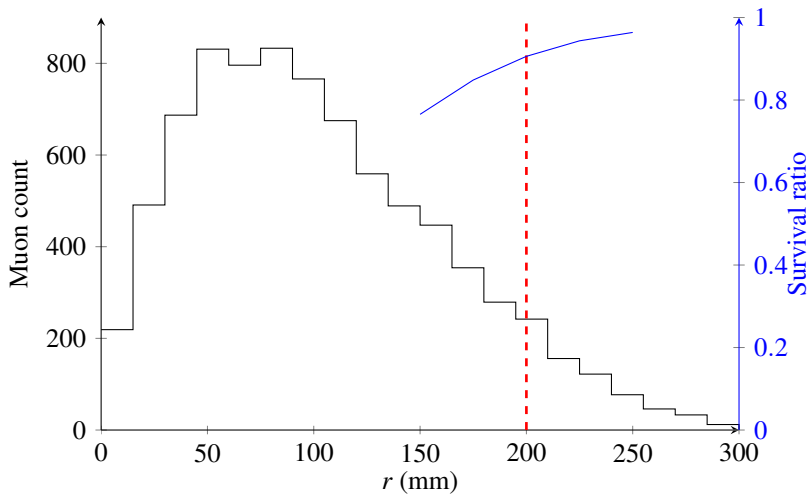

Figure 2.7: r-distribution histogram of accepted muons. The blue line shows the survival ratio. The red line is the cut limit where $R_S^k \approx 0.9$.

obtains

$$B_c \pi (r_c^{bp})^2 \approx B_d \pi (r_d^{bp})^2, \tag{2.6}$$

where r_c^{bp} and r_d^{bp} are the beam pipe radii at the target and at the drift section. $B_d = 1.5$ T is the magnetic field in the drift section and $B_c = 20$ T is the magnetic field at the capture magnet. Inserting equation 2.6 into equation 2.4 and reorganising gives an easy test for the limits just found

$$p_{Td}^{max} \leq p_T^{max} \sqrt{\frac{B_c}{B_d}}. \tag{2.7}$$

Inserting the known values gives $p_{Td}^{max} \leq 62$ MeV/c. Equation 2.6 gives the maximum radius $r_d^{max} = 254$ mm at the drift section. Comparing these results with figures 2.6 and 2.7 both values seem reasonable.

To summarise, the acceptance cuts were considered and decided upon at the end of the drift section ($z = 50$ m) based on the acceptance of muon accelerator. The acceptance cuts A_{50} are listed in table 2.3 and will be used frequently and for all optimisation studies, unless otherwise stated.

Table 2.3: The acceptance cuts A_{50} at $z = 50$ m.

Acceptance (Unit)	Value
p_{zmin}-p_{zmax} (MeV/c)	100-300
t_{min}-t_{max} (ns)	160-240
p_{Tmin}-p_{Tmax} (MeV/c)	0-50
r_{min}-r_{max} (mm)	0-200

2.3 The proton beam and calculations of initial positions

In the NF the proton beam emanates from the positions $(x, y, z) = (x_E, y_E, -750)$ mm, where x_E and y_E are unknown. To calculate the initial positions one can define the beam at the target centre and derive the equations of motion for the beam in a constant solenoid field. The beam intercepts the z'-axis of the target reference frame with the polar angle θ_{BT}. Derivation of the equations of motion for a particle in a constant solenoid field follows.

The first initial condition is the position of the target centre, defined as the intercept point between the beam and the target at $(x_0, y_0, z_0) = (0, 0, -375)$ mm. The second initial condition is the proton velocity $\mathbf{v_0}$ at the target centre, see figure 2.8.

Two reference frames will be used, the target frame (x', y', z') and the NF frame (x, y, z). The z-axis points down the centre line of the front-end and the target frame is rotated an angle θ_T around the x-axis. It is assumed that the proton travels undisturbed to the target centre, arriving with the initial beam energy E_b.
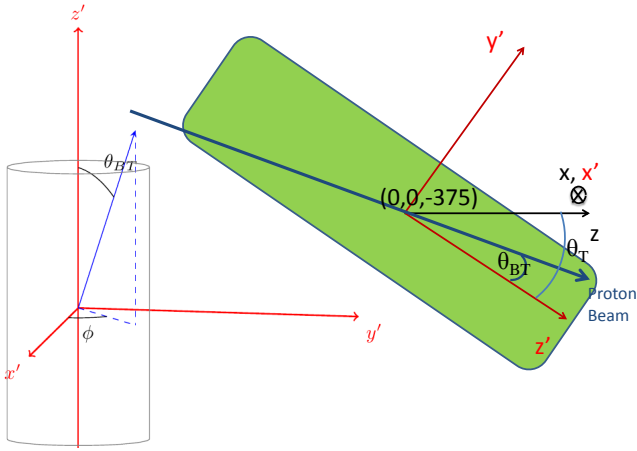
Figure 2.8: The beam definition: θ_T is the tilt angle of the target, ϕ is the azimuth angle in the target frame (x', y', z') defining the direction of the polar angle θ_{BT} between the beam and target.

The velocity vector in the target frame can then be found using the spherical co-ordinate system

$$\mathbf{v}' = |\mathbf{v}'|[\sin\theta_{BT}\cos\phi, \sin\theta_{BT}\sin\phi, \cos\theta_{BT}], \tag{2.8}$$

where θ_{BT} is the polar angle between beam and target, and ϕ is the azimuth angle from the x'-axis in the $x'y'$-plane. To find the velocity in the NF reference frame a rotation of angle $-\theta_T$ around the x-axis is done. This rotation with respect to the x-axis on matrix form is

$$\begin{bmatrix} x \\ y \\ z \end{bmatrix} = \begin{bmatrix} 1 & 0 & 0 \\ 0 & \cos(-\theta_T) & \sin(-\theta_T) \\ 0 & -\sin(-\theta_T) & \cos(-\theta_T) \end{bmatrix} \begin{bmatrix} x' \\ y' \\ z' \end{bmatrix}, \tag{2.9}$$

which when substituting position for velocity becomes

$$v_{x0} = v'_x, \tag{2.10}$$

$$= |\mathbf{v}'| \sin\theta_{BT} \cos\phi, \tag{2.11}$$

$$v_{y0} = v'_y \cos\theta_T - v'_z \sin\theta_t, \tag{2.12}$$

$$= |\mathbf{v}'|(\sin\theta_{BT} \sin\phi \cos\theta_T - \cos\theta_{BT} \sin\theta_T), \tag{2.13}$$

$$v_{z0} = v'_y \sin\theta_T + v'_z \cos\theta_T, \tag{2.14}$$

$$= |\mathbf{v}'|(\sin\theta_{BT} \sin\phi \sin\theta_T + \cos\theta_{BT} \cos\theta_T), \tag{2.15}$$

which is needed for the equations of motion.

The Lorentz force law, equation 2.3, applied on a charged point-like particle in a magnetic field $\mathbf{B}$ and electric field $\mathbf{E} \approx 0$ is

$$\gamma m_0 \frac{d\mathbf{v}}{dt} = q\mathbf{v} \times \mathbf{B}, \tag{2.16}$$

where $\mathbf{v}$ is the particle velocity, $\gamma = 1/\sqrt{1 - \left(\frac{v}{c}\right)^2}$, c is the speed of light, m_0 is the rest mass, t is the time and q is the particle charge. When $\mathbf{B} = (0, 0, B_z)$

$$\frac{dv_x}{dt} = \frac{qB_z}{\gamma m_0} v_y, \tag{2.17}$$

and

$$\frac{dv_y}{dt} = -\frac{qB_z}{\gamma m_0} v_x. \tag{2.18}$$

This can be written as a matrix

$$\begin{bmatrix} \dot{v}_x \\ \dot{v}_y \end{bmatrix} = \begin{bmatrix} 0 & \frac{qB_z}{\gamma m_0} \\ -\frac{qB_z}{\gamma m_0} & 0 \end{bmatrix} \begin{bmatrix} v_x \\ v_y \end{bmatrix}, \tag{2.19}$$

where $\frac{d\mathbf{v}}{dt} = \dot{\mathbf{v}}$, which gives $\omega^2 = \left(\frac{qB_z}{\gamma m_0}\right)^2$ and the general solution

$$v_x(t) = b_1 \sin\omega t + b_2 \cos\omega t, \tag{2.20}$$

$$v_y(t) = b_1 \cos\omega t - b_2 \sin\omega t, \tag{2.21}$$

where b_1 and b_2 are constants [29]. With the initial conditions: $v_x(0) = v_{x0}$ and $v_y(0) = v_{y0}$

$$b_1 = v_{y0}, \tag{2.22}$$

$$b_2 = v_{x0}, \qquad (2.23)$$

the velocities are

$$v_x(t) = v_{y0} \sin \omega t + v_{x0} \cos \omega t, \qquad (2.24)$$

$$v_y(t) = v_{y0} \cos \omega t - v_{x0} \sin \omega t. \qquad (2.25)$$

Integration yields

$$x(t) = \int v_x dt,$$

$$= \int (v_{y0} \sin \omega t + v_{x0} \cos \omega t) dt,$$

$$= -\frac{v_{y0}}{\omega} \cos \omega t + \frac{v_{x0}}{\omega} \sin \omega t + k, \qquad (2.26)$$

and

$$y(t) = \int v_y dt,$$

$$= \int (v_{y0} \cos \omega t - v_{x0} \sin \omega t) dt,$$

$$= \frac{v_{y0}}{\omega} \sin \omega t + \frac{v_{x0}}{\omega} \cos \omega t + c. \qquad (2.27)$$

The initial conditions (x_0, y_0, z_0, t_0) are used to get $k = x_0 + \frac{v_{y0}}{\omega}$ and $c = y_0 - \frac{v_{x0}}{\omega}$ and finally the equations

$$x(t) = x_0 + \frac{v_{y0}}{\omega}(1 - \cos \omega t) + \frac{v_{x0}}{\omega} \sin \omega t, \qquad (2.28)$$

$$y(t) = y_0 + \frac{v_{x0}}{\omega}(\cos \omega t - 1) + \frac{v_{y0}}{\omega} \sin \omega t, \qquad (2.29)$$

With $t = \frac{\Delta z}{v_{z0}}$ the initial positions can readily be found.

Setting the protons to emanate from $z = z_E = -750$ mm and fixing the parameters $E_b = 8$ GeV, $\theta_{BT} = 30$ mrad and $\theta_T = 96.68$ mrad while varying the azimuth angle ϕ the previous equations give the positions and velocities listed in table 2.4 and shown by the red and blue circles in figures 2.9 and 2.10. The circle centres are the initial positions for the selected values of the azimuth angle ϕ. The blue circle shows the

Table 2.4: The proton beam emanates from the positions x_E and y_E with the velocities v_{xE}/c, v_{yE}/c and v_{zE}/c at $z = -750$ mm, when varying the azimuth angle ϕ in the target frame. $E_b = 8$ GeV and $\theta_{BT} = 30$ mrad

| ϕ (°)	x_E (mm)	y_E (mm)	v_{xE}/c	v_{yE}/c	v_{zE}/c
0	-6.06	47.2	0.0317	-0.122	0.987
24	-10.5	45.7	0.0428	-0.116	0.987
48	-13.9	42.4	0.0506	-0.106	0.987
72	-15.7	38.1	0.0540	-0.0946	0.988
96	-15.6	33.4	0.0521	-0.0824	0.990
120	-13.5	29.1	0.0454	-0.0720	0.991
144	-10.0	26.1	0.0350	-0.0652	0.992
168	-5.5	24.7	0.0228	-0.0632	0.992
192	-0.87	25.3	0.0108	-0.0663	0.992
216	3.1	27.7	0.00108	-0.0740	0.992
240	5.8	31.6	-0.00464	-0.0850	0.991
264	6.7	36.2	-0.00537	-0.0973	0.990
288	5.6	40.8	-0.000994	-0.109	0.988
312	2.8	44.6	0.00773	-0.118	0.987
336	-1.37	46.9	0.0192	-0.122	0.987
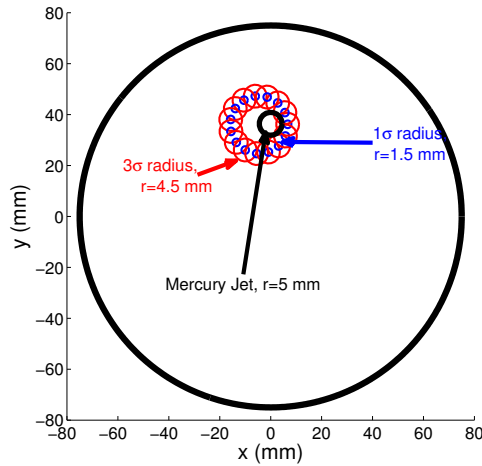
Figure 2.9: Proton beam initial positions at $z = -750$ mm. The beam enters in the upper half of the beam pipe (outer solid black circle) that has a radius $r_c^{bp} = 75$ mm.

radius standard deviation 1σ limit for each initial position and the red circle shows the 3σ limit for the same initial position. The black solid circle shows where the jet target would be located if it is a long straight cylinder with radius $r_T = 5$ mm, i.e. not affected by gravity.

Some of the red cirles in figure 2.10 overlap with the mercury target when the whole mercury jet is included. Specifically the right most initial positions where $\phi \in [240, 312]°$, a beam size of $3\sigma = 4.5$ mm would already partially interact with the target at $z = -750$ mm.
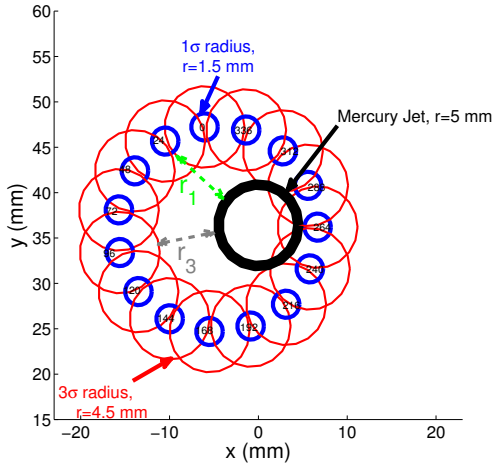

Figure 2.10: Initial positions for the proton beam zoomed in from figure 2.9. The numbers in the blue circle indicates the azimuth angle ϕ. The initial position when $\phi = 72°$ has the highest clearance from the target and the initial position when $\phi = 264°$ has the lowest clearance.

These calculations above were performed with a constant magnetic field of 20 T. However, in the NF the proton beam has to traverse a non-homogeneous magnetic field, from the initial position $z = -750$ mm, which would disturb the beam. To test the disturbance a simulation which includes the non-homogeneous field was performed to check if the proton passes through the centre of the target (0,0,-375) mm. The simulations showed that a proton beam with a beam size of 0 mm is disturbed by a distance $\Delta d = \sqrt{\Delta x^2 + \Delta y^2} \leq 0.2$ mm off the wanted intercept point at the target centre. However, the disturbance is much smaller than the proton beam size of 1.5 mm

and therefore this effect can be neglected.

2.4   Proton beam-target impact and layout optimisation studies

The production of secondary particles is studied using G4BL simulations. G4BL has several physics lists available to permit users to make trade-offs between simulation accuracy and CPU time [11]. In this thesis the default physics list for G4BL called QGSP is used. It is recommended and accurate for energies $E \sim 12$ GeV. The important energy ranges in this thesis is around 8 GeV for particle production and approximately 40-180 MeV for tracking of the captured particles. The low energy particles hitting the NF geometry are immediately lost, thus the important physics happens at an energy $E_b \approx 8$ GeV and therefore the QGSP physics list was chosen.

The initial positions, calculated by the equations in section 2.3 (all input parameters are the same), are used for the proton beam. The proton beam-size is set to $\sigma_x = \sigma_y = 1.5$ mm in the x and y directions, no other uncertainty parameters are set and defaults to 0.

The target is modelled as a $L_T = 2 * \frac{r_T}{\sin \theta_{BT}} \approx 300$ mm long cylinder of mercury which is approximately the length a proton, with intercept angle $\theta_{BT} \approx 0.03$ rad, would traverse under ideal conditions (figure 2.8).

2.4.1   Proton beam impact position on the target

Varying the intercept angle θ_{BT} and later the azimuth angle ϕ will change the proton beam's entry position and entry angles on the target which influence the particle production and thus the machine performance.

Varying the intercept angle between the beam and the target θ_{BT}

The azimuth angle ϕ is now fixed, while the angle between the beam and the target θ_{BT} varies. $\phi = 72°$ was chosen based on figure 2.10 as it has the highest clearance from the target. The performance when varying the angle θ_{BT} are shown in figure 2.11, where the black dots are the muon counts with acceptance cuts $\in A_{50}$ and the red dots are the muon counts without cuts. Every point has statistical error bars.

Muon count variations are observed both with and without acceptance cuts. The muon count is gradually reduced for increasing values of θ_{BT}, because when increasing θ_{BT} the protons will enter the upstream end of the target with an increasing distance
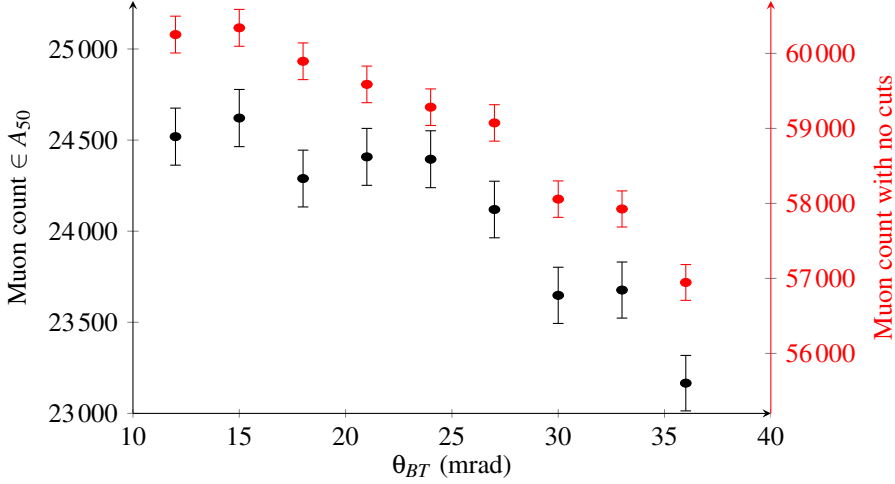
Figure 2.11: Muon counts at z=50 m with and without cuts when varying the intercept angle between beam and target θ_{BT}.

from the target centreline pointing along z'. Due to the beam size of $\sigma = 1.5$ mm some of the protons will not traverse the whole target length and the proton beam-target interaction region will decrease which will decrease the production of pions and the performance. Measurement of the proton path length will be performed to address this issue. The maximum difference in muon counts are $\approx 6\%$ with and without acceptance cuts.

The path length λ_{Air} of the proton trajectory inside the target, approximately that of a proton travelling through a target of air, is measured. The beam spot-size is $\sigma_x = \sigma_y = 1.5$ mm, the measured path lengths λ_{Air} are therefore only indicative of the average beam path length in the target.

Figure 2.12 shows the path length λ_{Air} when varying θ_{BT} and holding $\phi = 72°$ fixed. For $\theta_{BT} < 30$ mrad the proton enters and travels through the whole length of the target and therefore the path length $\lambda_{Air} = L_T = 300$ mm. When $\theta_{BT} > 30$ mrad the beam will have a shorter path length because it misses the upstream target-end and enters the target on the side.
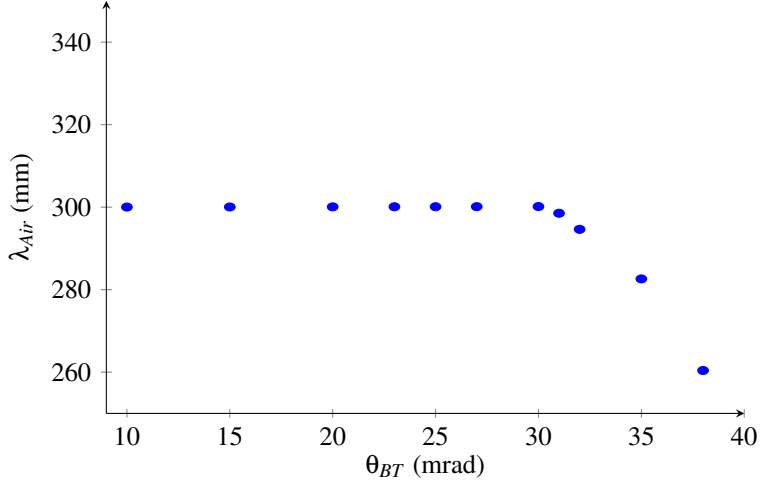
Figure 2.12: Path length λ_{Air} of a proton inside the target region when all interactions are turned off and varying the interception angle between beam and target θ_{BT}.

Varying the azimuth angle ϕ

The proton beam definition ensures different entry positions on the target when varying the azimuth angle ϕ and holding θ_{BT} fixed. The target length of $L_T = 300$ mm is chosen based on an intercept angle of 30 mrad as already described, therefore $\theta_{BT} = 30$ mrad.

The resulting muon influx variations at $z = 50$ m are shown in figure 2.13. The black dots are the muon counts with cuts $\in A_{50}$ and the red dots are muon counts without cuts. Every point has statistical error bars. In both cases performance variations when varying the incident azimuth angle ϕ are observed. For acceptance cuts A_{50} the muon count variation is up to 3% and for the case without cuts the muon count variation is up to 4.5%.

When ϕ is varied in the interval $\in [0, 336]°$ and $\theta_{BT} = 30$ mrad is fixed the proton traverses the whole target and the path lengths are $\lambda_{Air} = 300$ mm, for all ϕ's. Only very small variations in the order of 10^{-3} mm are observed. Therefore the observed fluctuations can not be explained by a variable path length λ_{Air}.

When varying the intercept angle between the beam and the target θ_{BT} the performance varied by up 6%, while when varying the azimuth angle ϕ the performance varied by up to 3%. The optimisation results show that the intercept
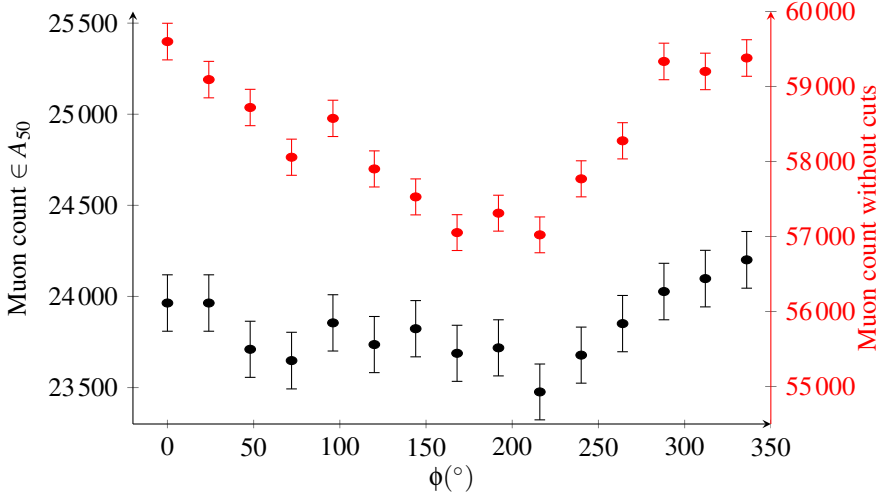
Figure 2.13: Muon counts with and without cuts when varying the azimuth angle ϕ.

angle between the beam and the target θ_{BT} should be kept between 10 and 15 mrad and the beam should enter the target from the top $\phi \approx 0°$. The crude measurements of the path lengths λ_{Air} did not explain the optimisation results, a more accurate method for path length measurement is adopted and discussed in subsection 2.4.4.

2.4.2 Shape fluctuations at the free-flowing mercury-jet

A free-flowing mercury-jet's surface shape fluctuates as can be seen in figure 2.14 [9]. To investigate the effect of such fluctuations the $L_T = 300$ mm long target is divided into 60 pieces of length $L_{Td} = 5$ mm and radius $r_T = 5$ mm. Each piece is then displaced a small random distance normal to the target as an approximate solution in G4BL.

From hydrodynamics studies of the mercury jet as it traverses the high gradient magnetic field of the $B_c = 20$ T solenoid, a quadrupole effect may be present that can distort the jet from a circular shape to an elliptical shape [18]. An approximate solution to the elliptical cylinder is used in G4BL. Optimisation studies on the beam-target interaction region with target shape fluctuations are presented in the following
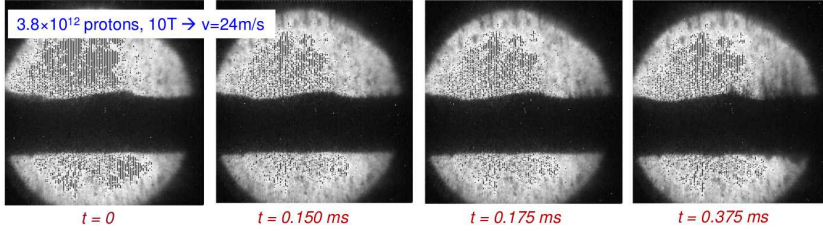
Figure 2.14: The free-flowing jet in a $B = 10$ T magnetic field at $t = 0$, 0.150, 0.175, and 0.375 ms at MERIT.

paragraphs.

Unevenly shaped jet surface

The target geometry fluctuations are varied from 0 to 1.5 mm. Starting with a smooth surface and stepwise increasing the target geometry fluctuations. The step size is 0.25 mm resulting in seven different target set-ups which are implemented in G4BL.

The position of each target piece of length 5 mm, indexed j, is shifted by a random distance $\Delta \mathbf{y}_{ij}$ mm along the y'-axis normal to the target

$$\Delta \mathbf{y}_{ij} = \sigma_j \mathbf{a}, \tag{2.30}$$

where σ_j is uniformly distributed on a limited interval $\sigma_j \in [-1, 1]$. The index i refers to the size of the geometry fluctuations $\mathbf{a} = [0, 0.25, 0.5, 0.75, 1.0, 1.25, 1.5]$. The free flowing jet target's mass is conserved. Figure 2.15 shows the geometry fluctuations of the target for $a_1 = 0.0$ mm, $a_4 = 0.75$ mm and $a_7 = 1.5$ mm, where the fluctuations increase from top to bottom

Figure 2.16 shows the relative muon flux for increasing geometry fluctuations, normalised to the case with no geometry fluctuations $a_0 = 0$ mm. Blue dots correspond to no cuts and red dots correspond to acceptance cuts $\in A_{50}$. The relative muon flux decrease with increasing geometry fluctuations, approximately 3 % when the geometry fluctuates with 30%. The MERIT experiment showed that the jet had geometry fluctuations, but the fluctuations were suppressed when in a magnetic field as is shown in figure 2.17 and the height of the jet grows when in a magnetic field. The effect of increasing the mercury jet height and decreasing the width is studied next.
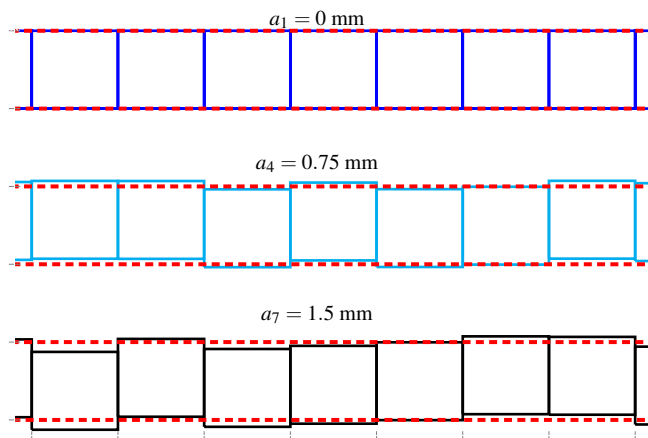
Figure 2.15: The target consists of several cylinders placed in series, illustrated by boxes in the figure. The red dashed lines indicate the geometry of a straight and smooth target with $a_0 = 0$ mm. The distance between the cylinders and the red dashed lines is Δy_{ij}.

Figure 2.16: Relative muon flux with error bars versus increasing geometry fluctuations.

Figure 2.17: Stabilisation of the mercury jet's geometry fluctuations in a magnetic field. The height of the jet is seen to grow when increasing the magnetic field.

Elliptical cylinder shaped jet

The distorted jet was modelled in simulations by increasing the height and squeezing the width, compared to the circular jet with radius $r = 5$ mm, to form an elliptically shaped jet.

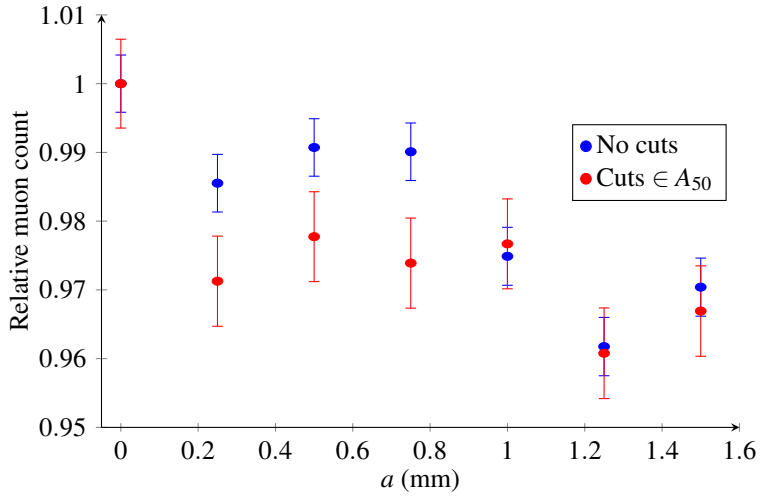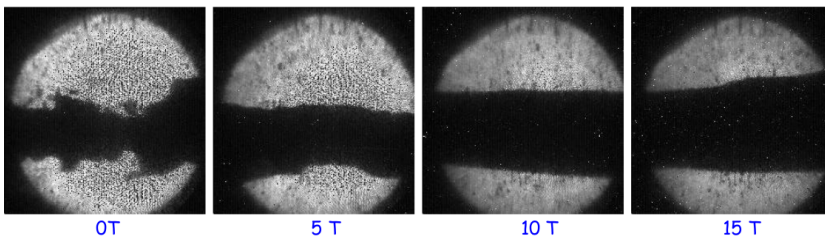The jet height increase has been reported to be $\sim 1.15 \times r_T$ in a 15 T magnetic field [18]. Here it is assumed that the height increases to $1.2 \times r_T$ when in a 20 T field. The major semi-axis of the ellipse should be $a = 6$ mm, therefore and from conservation of mass for the jet, the minor semi-axis is calculated to be $b \sim 4.2$ mm.

To approximate the elliptically shaped jet in G4BL, three cylinders were used; one at the centre with radius $r_1 = b$ mm and two placed at $y \pm 2$ mm with $r_2 = 3.8$ mm, see figure 2.18. The cylinders were tilted $\theta_T = 96.68$ mrad.
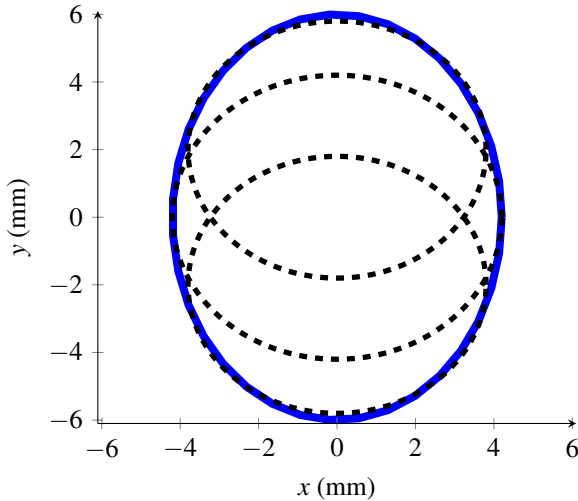
Figure 2.18: Cross section of the elliptical cylinder jet. The 3 circular cylinders overlap each other and approximates the elliptical cylinder.

The polar angle between the beam and target is fixed to $\theta_{BT} = 30$ mrad while the azimuth angle is varied $\phi \in [0, 336]$ degrees, in steps of 24 degrees, using the target reference frame. The muon count variations for an elliptical cylinder are shown and compared with a circular cylinder in figure 2.19. The maximum particle count variation is ~ 3 % for both cases and the elliptical target has a lower count, on average. The error
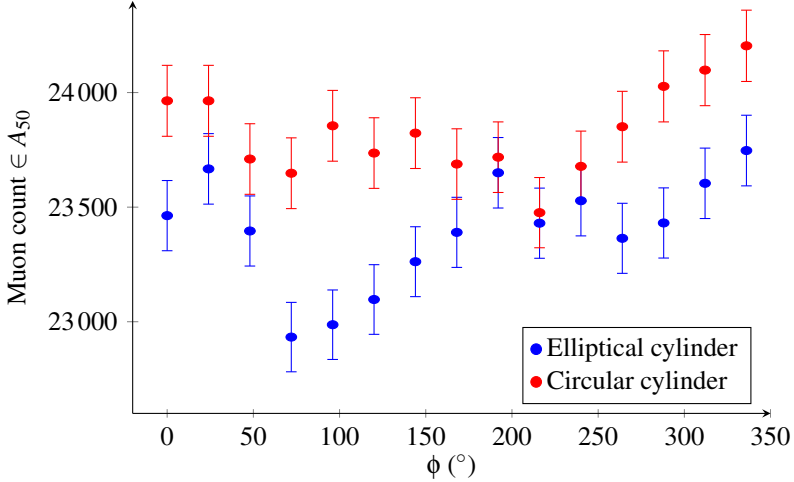
Figure 2.19: Muon count versus the azimuth angle ϕ. Error bars are statistical.

bars are statistical. The path length will be investigated to explain the variations. The path length λ_{Air} in the elliptical cylinder is shown and compared to the path length λ_{Air} in a circular cylinder in figure 2.20. The path length in an elliptical cylinder is shorter when the proton beam enters the target on the left side $\phi \in [72, 120]°$ and the right side $\phi \in [240, 312]°$. The path length λ_{Air} and the muon count extremes are located at the same azimuth angles ϕ, thus explaining the muon count variations.

To better understand the path length variations figure 2.21 shows the entry positions on a circular and an elliptical cylinder for a beam with size 1σ. The entry positions are identical for the circular and the elliptical cylinders. For the elliptical cylinder the path length variations are due to the elliptic shape. When the proton enters the elliptical target on either of the sides it traverses a shorter interaction region, compared to the circular target, resulting in a shorter path length. In addition, the centres of the blue circles on the left side of the elliptical cylinder are outside the cylinder. Thus shortening the interaction region further for $\phi \in [48, 120]°$.

In summary the shape fluctuations of the mercury jet are shown to reduce the performance by ~ 3 % or less.
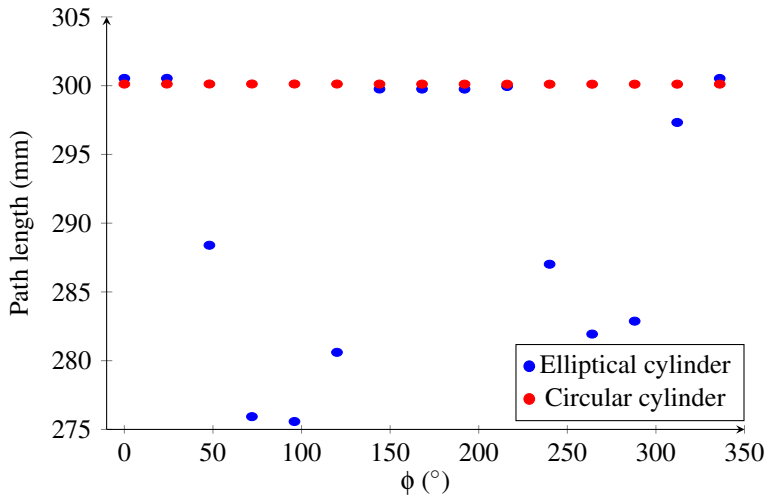
Figure 2.20: Path lengths λ_{Air} vs the azimuth angles ϕ for the elliptic and circular targets.
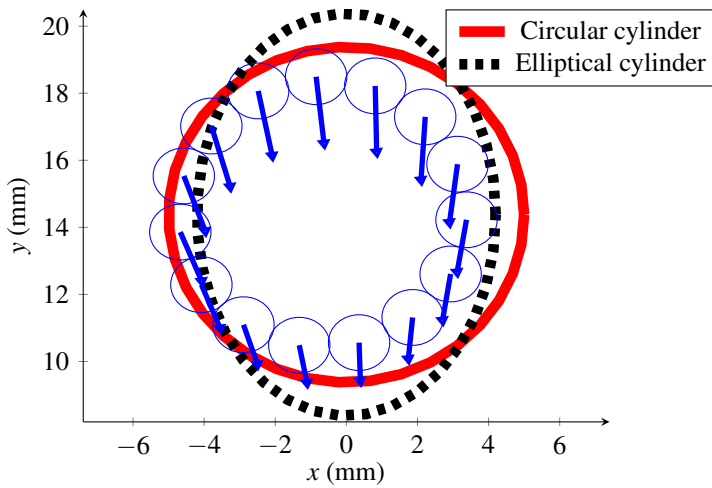

Figure 2.21: Entry positions at $z = -524.3$ mm (the upstream end of the target) with 1σ beam size and velocity directions at the circular target. The elliptical target shape is also shown.

2.4.3   Elongating the target model

In this subsection the target is elongated to better resemble a free-flowing liquid mercury jet.

Due to the helical proton trajectory in the magnetic field the assumption that a proton would traverse the same target length for all ϕ's is not true for a longer target. In addition the path length measure used in the previous subsection didn't take into account the size of the beam. Therefore an improved measurement method of the path length is proposed to provide better accuracy.

The free-flowing mercury jet is assumed to travel in a straight line (no gravity) without shape fluctuations from the nozzle at $z = -750$ mm down to the magnet shielding. Therefore in a more realistic simulation a long straight cylinder of mercury with radius $r_T = 5$ mm replaces the short $L_T = 300$ mm target. All beam and target parameters remain the same as before.

The new path length measurement method is as follows. 10000 protons are aimed at the target and each individual proton's trajectory in the proton beam-target interaction region (IR) is tracked. The average trajectory length of all tracks are used as a more accurate path length λ_{IR} measure. All interactions are turned on in G4BL.

The path length λ_{IR} error bars will be estimated by the standard error

$$s_e = \frac{s}{\sqrt{n}}, \tag{2.31}$$

where s is the estimated standard deviation and n is the sample size [30].

Varying the azimuth angle ϕ for the circular cylinder jet target

The longer and more realistic target model has replaced the short target model in the simulation. As before the azimuth angle ϕ is varied while the intercept angle $\theta_{BT} = 30$ mrad is fixed and the results are reported.

In figure 2.22 the muon counts of the long target model and the short target model are compared. The muon count has decreased on average by approximately 8% for the long target model and the maximum muon count variations are approximately 6%. The muon count is lower in the range $\phi \in [144, 312]$ and the minimum is at $\phi = 264°$. The reason is that the distance between the beam and the target is smaller in this region and the beam interacts with the target earlier. The interaction region is shifted closer to the beam pipe and more particles are lost when they hit the shielding.

Figure 2.23 shows the mean path length λ_{IR} with respect to the azimuth angle ϕ. The highest path length λ_{IR} is found when the protons enter the jet from the side $\phi \sim$
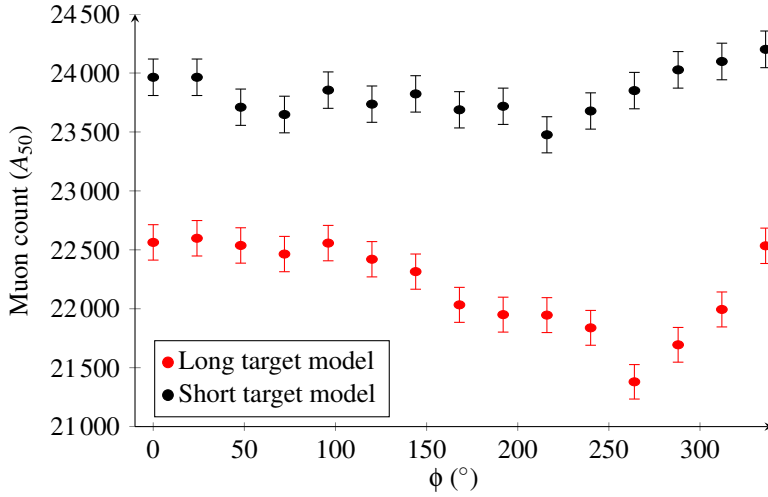
Figure 2.22: Muon counts with acceptance cuts A_{50} versus ϕ for the short 300 mm target model and the longer and more realistic target model.
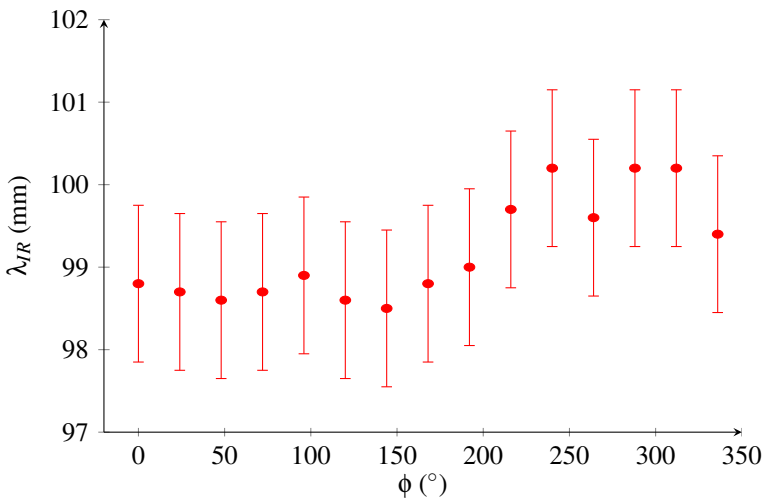
Figure 2.23: Path length λ_{IR} versus the azimuth angle ϕ.

$270°$. Comparing the path length λ_{IR} with the muon count for each azimuth angle step ϕ, no clear correlation is found. The path length measurement variations are $\Delta\lambda_{IR}^{max} \approx 2$ mm.

Varying the azimuth angle ϕ for an elliptical cylinder jet

From hydrodynamics studies of the mercury jet as it traverses the high gradient magnetic field of the central solenoid a quadrupole effect may be present [18] that can distort the jet to an elliptical shape. In simulations the long and more realistic elliptical cylinder jet target is approximated as a combination of three circular cylinders as described in subsection 2.4.2.

Comparing the muon count with acceptance cuts $\in A_{50}$ for the long elliptical and long circular cylinder targets, the influx to the buncher is on average 1.3 % lower for the elliptical target as shown in figure 2.24. The minimum influx to the buncher is
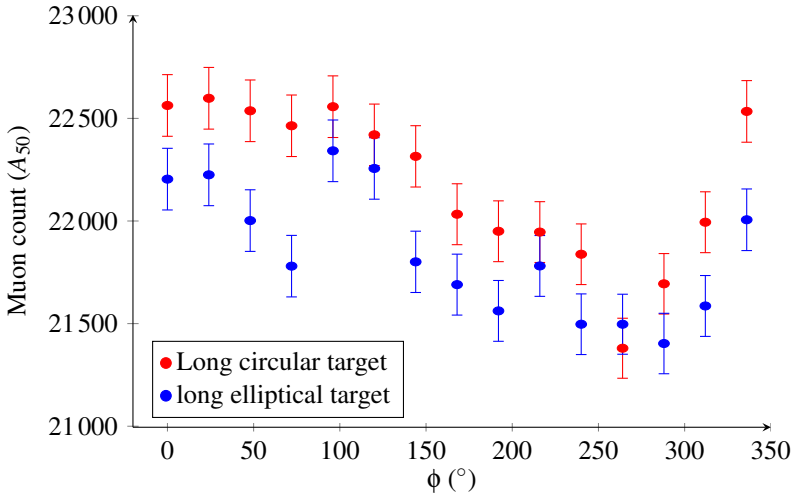
Figure 2.24: Muon count with acceptance cuts when varying the azimuth angle ϕ. Statistical error bars.

found when the proton beam enters the target on the side $\phi \sim 264°$ and the maximum influx is found when the proton beam enters on the opposite side of the target $\phi \sim 96°$.
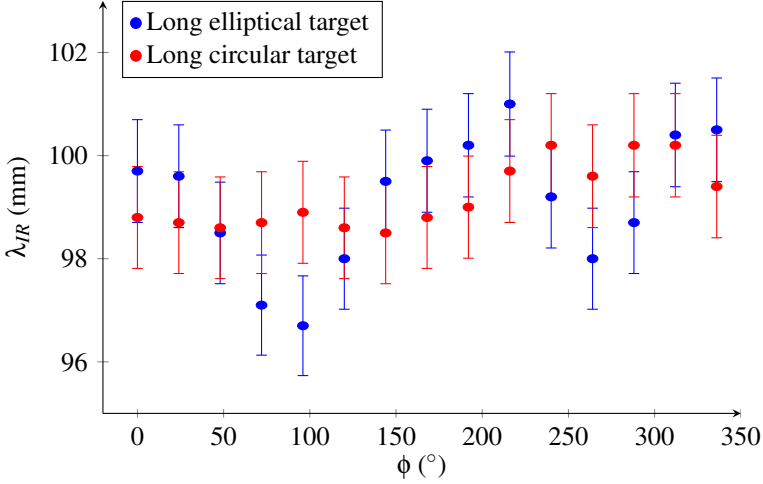
Figure 2.25: Path length λ_{IR} versus the azimuth angle ϕ for the elliptical and the circular targets.

Figure 2.25 shows the path length λ_{IR} with respect to the azimuth angle ϕ for the long elliptical target and the long circular target. The path length λ_{IR} variations for the long elliptical target are up to approximately $\Delta\lambda_{IR}^{max} \approx 4$ mm and higher than for the long circular target. The path length λ_{IR} is lower when the proton beam enters the target on the sides $\phi \sim 90°$ and $\phi \sim 270°$ where the ellipse has it is minor semi-axes and higher when the protons enter from below $\phi \sim 180°$ or from the top $\phi \sim 0°$ where the ellipse has it is major semi-axis. No clear correlation between the path length λ_{IR} and the muon count is found.

A full length mercury jet target was introduced and replaced the short target. In addition an improved measurement of the proton beam trajectory in the target or the proton path length λ_{IR} was introduced. The optimisation with respect to the azimuth angle ϕ showed that the proton beam should enter the target from the top for optimal performance, when the intercept angle is $\theta_{BT} = 30$ mrad. The effect of shape fluctuations on the long target in a high magnetic field reduces the performance by a maximum of only 1.3 %.

2.4.4   Path length in the proton beam-jet interaction region

When using a long target care must be taken to avoid early interactions between the spiralling beam and the jet-target. Figure 2.26 shows the 1σ and 3σ beam-sizes and the circumference of the cylinder target at $z = -750$ mm.
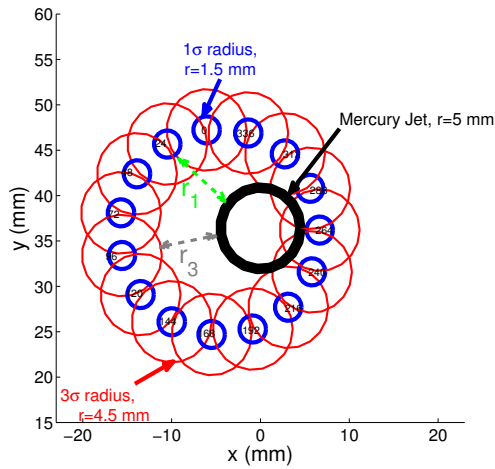
Figure 2.26: Initial positions for the proton beam at $z = -750$ mm.

The clearance radius r_k is the shortest distance between the beam and the target at $z = -750$ mm. The clearance radius r_k varies according to the angle between the beam at the target θ_{BT}. To avoid early interactions a minimum clearance radius of one or three times the size of the proton beam, $k = 1$ or $k = 3$ such that $r_1 \geq 1\sigma$ and $r_3 \geq 3\sigma$ is required. The minimum angle θ_{BT}^{min} ensures a minimum clearance radius greater than or equal to r_k. Equations from section 2.3 were used for calculations. The minimum angles θ_{BT}^{min} when varing the azimuth angle ϕ are shown in figure 2.27. The blue circular points show the minimum angles θ_{BT}^{min} for $r_1 = 1\sigma$ and the red triangles show the minimum angles θ_{BT}^{min} for $r_3 = 3\sigma$. The figure shows that early interaction between the proton beam and the long target is likely when the angle θ_{BT} is small.

To investigate potential early interactions the trajectory of each individual proton has been tracked until it interacts with the target. Figure 2.28 shows the y-distribution of the interaction points between each tracked proton and the target when the azimuth
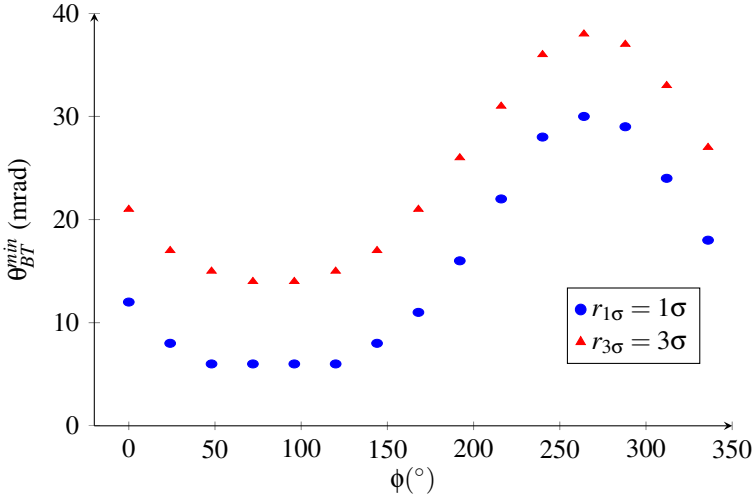
Figure 2.27: Minimum angle between beam and target θ_{BT}^{min} versus azimuth angle ϕ.

angle is $\phi = 0°$. The interactions are off-centred by several millimetres and the peak is at $y \approx 18$ mm. An off-centre and spiralling particle will have a higher probability of being lost through scraping in the beam pipe which leads to a lower muon influx to the buncher. Shifting the *y*-distribution peak of the interactions closer to the beam pipe centre which is closer to the focal point of the optics system of the solenoids could increase particle yield, but then a re-definition of the proton beam is necessary.

2.4.5 Re-defining the proton beam

The undesirable early interactions between the proton beam and the target allowed for a change of the proton beam definition. A re-definition of the proton beam is presented to move the proton beam-jet interaction region closer to the centre of the beam pipe to avoid early interactions.

When using the velocity $\mathbf{v_E}$ and the positions x_E, y_E at $z_E = -750$ mm listed in table 2.4 the proton beam will cross target centre at $(x, y, z) = (0, 0, -375)$ mm. In the re-defined proton beam the crossing point will be shifted away from the centre and to the surface of the target as shown in figure 2.29. This way the entry position and the entry angles on the target can be controlled and early interactions avoided.
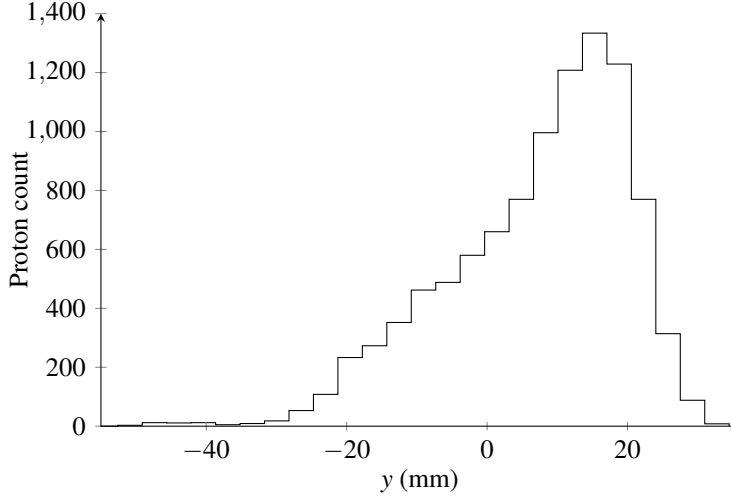
Figure 2.28: Transverse distribution of the proton beam-target interactions for $\phi = 0°$.

First the shift in position or the displacement from the centre of the target has to be calculated. The target reference frame is used. The displacement length is $\rho = \sqrt{\Delta x_0'^2 + \Delta y_0'^2 + \Delta z_0'^2}$ from the target centre to the surface of the target. $\Delta x_0'$, $\Delta y_0'$, $\Delta z_0'$ are the displacements in the x', y' and z' directions.

The displacement vector ρ ends on the target surface, therefore the constraint $r_T = \sqrt{\Delta x_0'^2 + \Delta y_0'^2}$ is imposed, where r_T is the target radius. The displacement vector in the target frame is

$$\rho = [r_T \cos\phi', r_T \sin\phi', \Delta z'], \tag{2.32}$$

where ϕ' is the azimuth angle. Using the rotation matrix, equation 2.9, and a known displacement vector ρ the displacements in the NF reference frame can be calculated by

$$\Delta x = \rho_x,$$
$$= r_T \cos\phi', \tag{2.33}$$
$$\Delta y = \rho_y \cos\theta_T - \rho_z \sin\theta_t,$$
$$= r_T \sin\phi' \cos\theta_T - \Delta z' \sin\theta_T, \tag{2.34}$$
$$\Delta z = \rho_y \sin\theta_T + \rho_z \cos\theta_T,$$

Figure 2.29: Redefinition of the beam. The beam is shifted a distance ρ to the surface of the target. Rotations are greatly exaggerated.

$$= r_T \sin\phi' \sin\theta_T + \Delta z' \cos\theta_T. \qquad (2.35)$$

Adding these displacements to the initial positions at $z_E = -750$ mm the displacement vector can now be used to control the entry position of the proton beam on the target. The entry position in the target reference frame will be $(x'_0, y'_0, z'_0) = (\Delta x'_0, \Delta y'_0, \Delta z'_0)$. The angles θ_{BT} and ϕ refers to the angles at target surface and not at the centre of the target. In addition the variation of Δz introduce a shift in time which can be calculated by

$$\Delta t = \frac{\Delta z}{v_{z0}}. \qquad (2.36)$$

Centering particle production in the beam pipe

The proton-beam target interaction region where the secondary pions are produced can be considered as the particle source. The effective interaction region is determined by the entry and exit points and directions of the primary proton beam.

The transverse distribution peak of the interaction region for $\phi = 0°$ was shown to be off-centred by $y \approx 18$ mm. Taking advantage of the newly defined proton beam early interactions can be avoided and the distribution peaks can be shifted closer to the origin. For example when $\phi' = 0$ and $\Delta z' = 0$ mm are chosen the proton beam will enter the target from the top at $z' = 0$ mm and when $\phi' = 0$ and $\Delta z' = -25$ mm the proton beam will enter the target from the top at $z' = -25$ mm. $\Delta z'$ is varied from -150 mm to 0 mm in table 2.5 which shows the proposed initial positions and velocities for the proton beam at $z = -750$ mm and the linear displacements with respect to the target centre. The time shift from equation 2.36 is also taken into account.

Table 2.5: Initial positions and the linear displacements for the proton beam's entry positions. The azimuth angle $\phi = 0°$ and intercept angle $\theta_{BT} = 30$ mrad, the displacement vector has azimuth angle $\phi' = 90°$, target radius $r_T = 5$ mm and thus $\Delta x = 0$ mm.

$\Delta z'$ (mm)	Δy (mm)	Δz (mm)	x_E (mm)	y_E (mm)	v_{xE}/c	v_{yE}/c	v_{zE}/c
-150	19.46	-148.82	-2.21	48.15	0.0192	-0.124	0.987
-125	17.04	-123.93	-2.72	48.86	0.0213	-0.124	0.987
-100	14.63	-99.05	-3.29	49.57	0.0234	-0.123	0.987
-75	12.22	-74.17	-3.90	50.26	0.0255	-0.123	0.987
-50	9.80	-49.28	-4.57	50.95	0.0276	-0.123	0.987
-25	7.39	-24.40	-5.30	51.62	0.0297	-0.122	0.987
0	4.98	0.48	-6.07	52.28	0.0317	-0.122	0.987

The target is circular cylindrical. Using these initial positions the transverse *y*-distribution of each individual proton interaction point in the target is investigated and shown in figure 2.30. The distribution peak, or the particle production centre, is off-
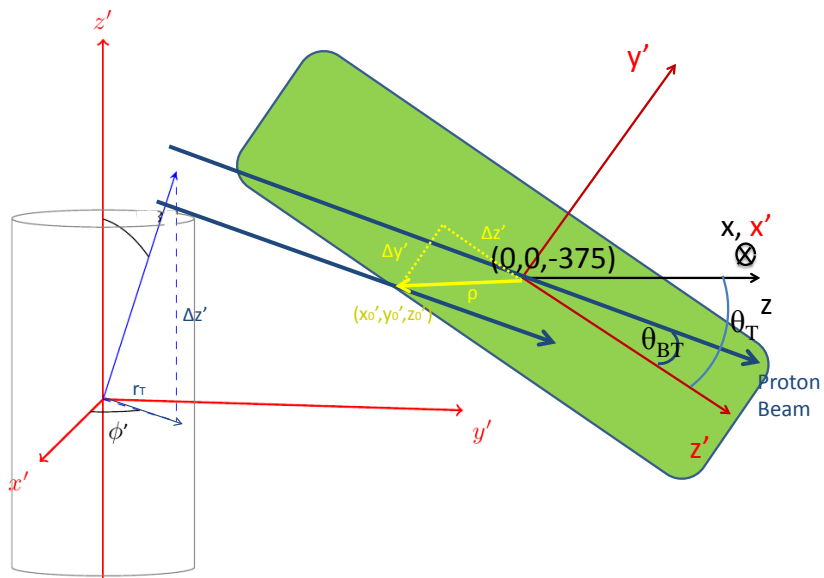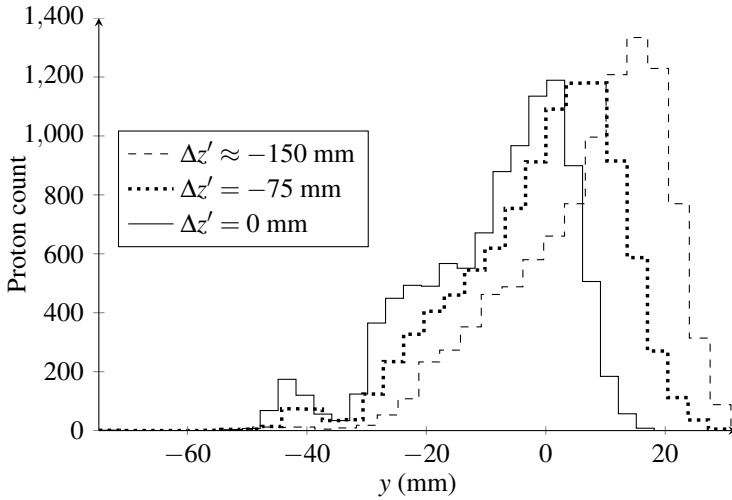

Figure 2.30: Transverse distribution of the proton beam-target interactions.

centred in the positive *y*-direction. The secondary particles are therefore produced in the upper part of the beam pipe, out of the focal point and more particles will be lost from scraping in the shielding. The dashed line shows the distribution for $\Delta z' = -150$, the dotted line shows the distribution for $\Delta z' = -75$ mm and the solid line shows the distribution for $\Delta z' = 0$ mm. The proposed initial positions from table 2.5 does indeed shift the distribution along the *y*-axis.

The transverse *y*-distributions of the interaction points are skewed and non-gaussian, the median was therefore chosen over the mean to indicate the central tendency. The transverse *y*-distribution medians when varying $\Delta z'$ versus the particle count directly after the target at $z = 0$ m are shown in figure 2.31. The particle count increases with decreasing median of y in the interval $\in$ [-4, 9] mm. Centring the interaction region and the particle production in the beam pipe increases the particle count at $z = 0$ mm by 10.5 % comparing $\Delta z' = -25$ mm with $\Delta z' \approx -150$ mm. Then the secondary particles will have a centred radial distribution, thus potentially increasing the muon yield at the
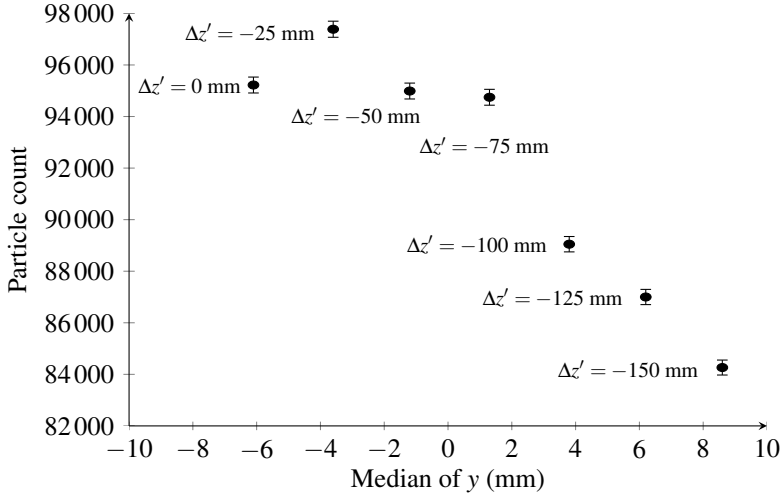
Figure 2.31: Muon and pion count with respect to the median value of y, count at $z = 0$ mm.

buncher as well as at $z = 0$ mm. In addition the energy deposition is spread out more evenly such that the upper part of the shielding does not get the peak of the radiation.

However, the interaction region is moved closer and closer to the plane at $z = 0$ m where the particle flux is measured when $\Delta z'$ varies and therefore the particle flux will increase. To make sure the optimised performance at $z = 0$ mm also optimises the influx to the buncher a performance comparison is made at $z = 50$ m at the end of this chapter.

Centring the proton beam-target interaction region in the beam pipe resulted in a centred secondary beam which increased the flux of secondary particles after the target by 10.5 %.

Increasing the path length

Decreasing the intercept angle θ_{BT} could increase the proton beam's average path length λ_{IR} in the jet. Thus θ_{BT} is varied in the interval $\in [20, 35]$ mrad, while keeping the optimal median value at $y \approx -4$ mm found previously which means fixing $\Delta z' = -25$ mm. Table 2.6 shows the initial positions and velocities for the proton beam at $z = -750$ mm and the linear displacements of the proton beam's entry positions on

the jet target.

Table 2.6: Proton beam initial positions when varying the intercept angle θ_{BT} for a chosen entry position. The position vector can be read off table 2.5 for $\Delta z' = -25$ mm. The velocity vector has azimuth angle $\phi = 0°$ and varying intercept angle θ_{BT}.

θ_{BT} (mrad)	x_E (mm)	y_E (mm)	v_{xE}/c	v_{yE}/c	v_{zE}/c
20	-4.87	48.09	0.0273	-0.113	0.988
25	-5.08	49.86	0.0285	-0.117	0.987
27	-5.17	50.56	0.0290	-0.119	0.987
30	-5.30	51.62	0.0297	-0.122	0.987
33	-5.43	52.68	0.0304	-0.125	0.986
35	-5.51	53.39	0.0309	-0.127	0.986

Figure 2.32 shows the particle count without acceptance cuts at $z = 0$ m versus the average path length λ_{IR}, due to the decreasing intercept angle θ_{BT}. The particle count increases for a longer path length λ_{IR}, the longest path length λ_{IR} is 100.8 mm giving an increased particle count of another 6.8 % giving a total increase of 17.3 % compared with the lowest particle count in figure 2.31.

To make sure the particle production optimisation done at $z = 0$ m also increases the influx to the buncher, the performance measure is moved to $z = 50$ m. The relative muon flux with acceptance cuts A_{50} are shown in figure 2.33, combining these optimisations give an increased muon count of ≈ 6 % compared to the non-optimised at $\theta_{BT} = 25$ mrad.

The proton path length in the jet was increased which gave an increased muon count of 6.8% after the target, giving an accumulated increase of 17.3 %.

The optimised proton beam parameters, the accumulated effect of all target optimisation studies, increased the performance by approximately 6 % when applying acceptance cuts. Changes and improvements at this level are very significant and important when discussing cost and performance for a future neutrino facility.
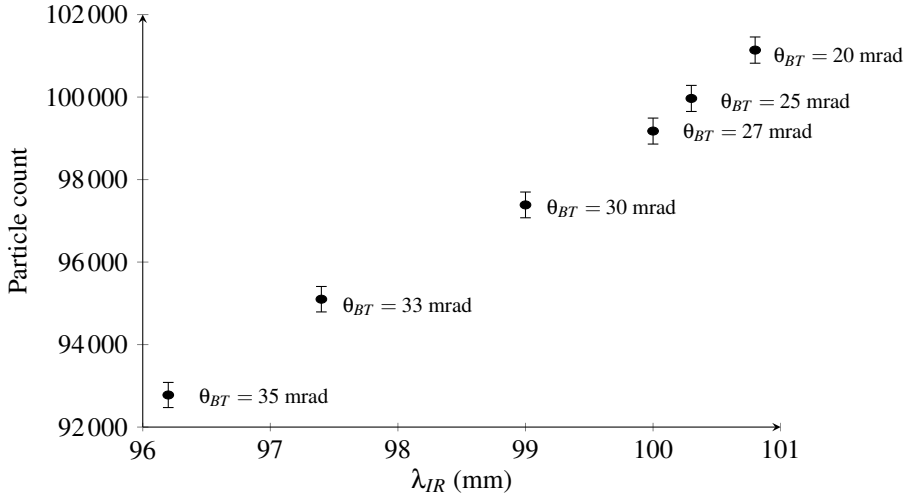
Figure 2.32: Muon and pion count without acceptance cuts at $z = 0$ m versus the path length λ_{IR}. The intercept angle θ_{BT} is indicated to the right of the marks.
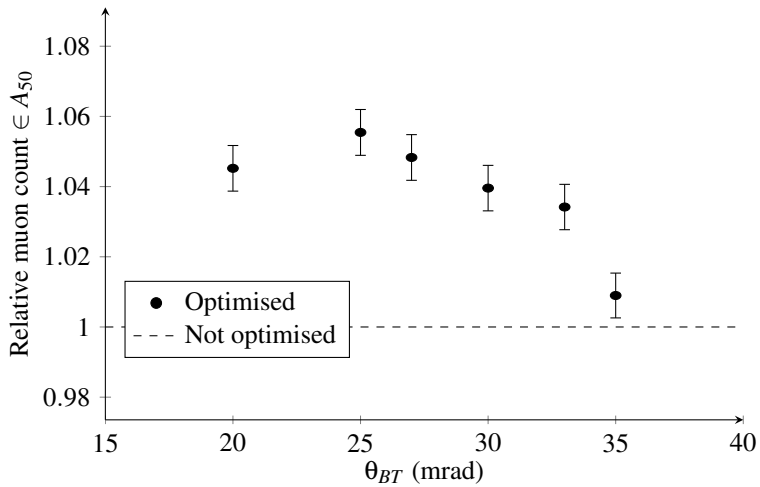

Figure 2.33: Relative muon count with acceptance cuts A_{50} versus the intercept angle θ_{BT} at $z = 50$ m.

2.5 Summary

A detailed assessment of the optimisation of the proton beam-target layout and geometry in the Neutrino Factory has been made. The focus was the flux of secondary particles from the interaction between primary protons and the mercury target. Optimising the flux of secondary particles is important in order to increase the muon density in the storage ring, which ultimately increase the neutrino beam intensity.

Initially the ST2a baseline configuration was presented in detail, the figure of merit was established with acceptance cuts and the incoming proton beam was defined.

The optimisation of the beam's impact position and impact angles on the short mercury target showed that the intercept angle between the beam and the target θ_{BT} should be kept between 10 and 15 mrad and the beam should enter the target from the top for optimal performance. When varying the intercept angle between the beam and the target θ_{BT} the performance varied by up 6%, while when varying the azimuth angle ϕ the performance varied by up to 5%. The effect of shape fluctuations on the free-flowing mercury jet target in a high magnetic field is shown to reduce the performance by 3 % or less.

A full length mercury jet target was introduced and replaced the short target. In addition an improved measurement of the proton beam trajectory in the target or the proton path length λ_{IR} was introduced. The optimisation with respect to the azimuth angle ϕ showed that the proton beam should enter the target from the top for optimal performance, when the intercept angle is $\theta_{BT} = 30$ mrad. The effect of shape fluctuations on the long target in a high magnetic field reduces the performance by a maximum of only 1.3 %.

Centring the proton beam-target interaction region in the beam pipe resulted in a centred secondary beam which increased the flux of secondary particles after the target by 10.5 %. The proton path length in the jet was increased which gave an increased muon count of 6.8% after the target, giving an accumulated increase of 17.3 %.

The optimised proton beam parameters, the accumulated effect of all target optimisation studies, increased the performance by approximately 6 %. Changes and improvements at this level are very significant and important when discussing cost and performance for a future neutrino facility.

Chapter 3

Optimising the Capture and Tapering sections

In this chapter optimisation studies of the capture, tapering and drift sections will be explained. The baseline configuration includes a series of magnets and a target. The configurations will evolve from there. The main results are published in [31].

The Neutrino Factory storage ring is designed to have 10^{21} muon decays/year. This puts high requirements on the performance of the Capture and the Tapering sections of the facility. The Capture section of the Neutrino Factory includes a superconducting solenoid and small normal conducting solenoids which together produce a magnetic field of $B_c \approx 20$ T around the target. Downstream of the Capture section the Tapering section consists of a series of large aperture superconducting solenoids producing the adiabatic magnetic field tapering.

It is imperative to maximise the muon influx to the buncher as this ultimately limits the muon density in the storage ring. Therefore the magnetic field strength in the capture section, the shape of the magnetic field in the tapering section and the magnetic field strength in the drift section are studied to optimise performance.

The superconducting solenoids are the critical components of the capture and tapering sections as they produce the magnetic field which captures the secondary particles and influence the performance. High energy deposition in the solenoids will make the magnet quench, thus shielding is in place to protect the solenoids. In addition the shielding protect the solenoids from long-term damage from radiation. The magnetic field is modelled in G4BL including extremely long solenoids. It is assumed that shorter real magnets can reproduce the magnetic field reasonably well. The goal is to

improve the capture efficiency, by using alternative magnetic field tapering, alternative solenoid geometry and alternative solenoid shielding set-ups. The magnetic field tapering is varied by changing the current densities in each magnet and/or changing the magnet geometries.

The performance of each set-up is measured as the acceptance influx A_{50} to the buncher at $z = 50$ m. The acceptance influx to the buncher are based on the acceptance of the muon accelerator. The acceptance A_{50} is listed in table 3.1 and will be used frequently and for all optimisation studies. The performances with and without acceptance cuts are reported.

Table 3.1: The acceptance cuts A_{50} at $z = 50$ m.

Acceptance (Unit)	Value
p_{zmin}-p_{zmax} (MeV/c)	100-300
t_{min}-t_{max} (ns)	160-240
p_{Tmin}-p_{Tmax} (MeV/c)	0-50
r_{min}-r_{max} (mm)	0-200

The optimisation studies are performed using the simulation tools FLUKA [10] and G4beamline [11]. Figure 3.1 shows the capture and the tapering sections of the Neutrino Factory.
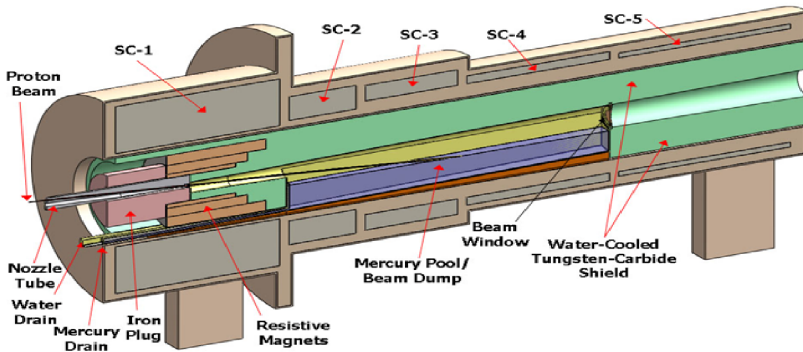

Figure 3.1: Baseline layout of the target, capture and tapering sections. The proton beam hits the target to produce pions, the pions are focussed downstream by the magnetic field made by the surrounding SC magnets. Figure taken from [5].

3.1 Initial studies using simplified geometry

The initial capture and tapering studies are performed using the Feasibility Study 2 (ST2) magnet configuration containing 13 solenoid magnets. [5]. The geometry of the capture and tapering sections of the ST2 configuration is listed in table 3.2 and shown

Table 3.2: The ST2 magnet configuration, geometry and current density taken from [5]. z is the position of the upstream end of each element, Δz is the element length, R_i is the element inner radius, ΔR is the element thickness. The value of the current density J for SC12 was discarded.

	z (m)	Δz (m)	R_i (m)	ΔR (m)	J (A/mm^2)
SC1	-1.203	1.781	0.636	0.642	23.39
SC2	0.678	0.729	0.686	0.325	25.48
SC3	1.507	0.999	0.776	0.212	29.73
SC4	2.606	1.550	0.776	0.107	38.26
SC5	4.256	1.859	0.776	0.066	49.39
SC6	6.050	0.103	0.416	0.051	68.32
SC7	6.325	2.728	0.422	0.029	69.27
SC8	9.103	1.749	0.422	0.023	75.62
SC9	10.902	1.750	0.422	0.019	77.37
SC10	12.702	1.749	0.422	0.017	78.78
SC11	14.501	1.750	0.422	0.015	79.9
SC12	16.301	2.366	0.422	0.013	-0.85
Cu1	-0.662	0.749	0.178	0.054	24.37
Cu2	-0.662	0.877	0.231	0.122	19.07
Cu3	-0.662	1.073	0.353	0.137	14.87

in figure 3.2. The first twelve superconducting (SC) magnets, SC1-SC12, produce the tapered magnetic field and the thirteenth superconducting magnet SC13 the drift field B_d. SC13 is placed 50 mm after SC12 as one very long solenoid magnet extending up $z = 50$ m.

The value for magnet current SC12 was discarded as it gave a magnetic field $B_{SC12} \approx 0$ T over a length of 2 m. Instead the current density J_{SC12} of SC12 was changed manually until the magnetic field B_{SC12} matched the boundary conditions $B_{SC11} = B_{SC12} = B_{SC13}$. The matching resulted in a current density for SC12 of $J_{SC12} = 85.85$ A/mm^2 and a current density for SC13 of $J_{SC13} = 85.0$ A/(mm)^2. Figure 3.3

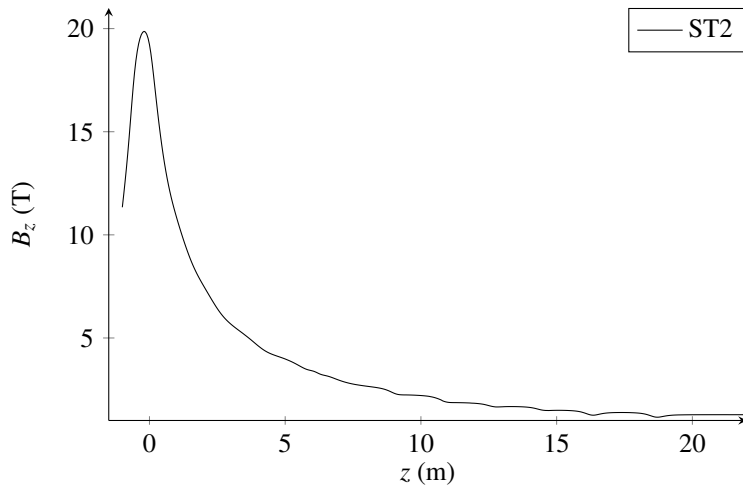Figure 3.2: ST2 magnet configuration, consisting of 13 solenoids.

Figure 3.3: The magnetic field tapering of the ST2.

shows the magnetic field for the ST2 set-up.

The target centre is at $z = -375$ mm and the tilt angle is $\theta_T = 96.68$ mrad with respect to the z-axis. The target length is $L_T = 300$ mm and the target radius is $r_T = 5$ mm. The impinging proton beam has an angle $\theta_{BT} = 30$ mrad with respect to the target axis and kinetic energy $E_b = 8$ GeV. These beam parameters are equal for all set-ups.

3.1.1 Elongating the tapering section

A set-up with identical geometry to the ST2 is renamed to 13sol (named after the number of solenoids in ST2) to avoid confusion with the original ST2. These 13sol alternatives have different current densities and thus different magnetic field tapering than the original. An index is added to the set-up name 13sol_i, the index i signifies that the current density J of at least one of the thirteen solenoids has been changed from the original. The tapering sections of the 13sol set-ups are longer than the ST2.

The current density J input parameters to G4BL for the 13sol set-ups are listed in table 3.3 and the longer 13sol_i on-axis magnetic fields are shown in figure 3.4 where

Table 3.3: Magnet currents for each SC solenoid for 13sol.

	13sol_1	13sol_2	13sol_3	13sol_4	13sol_5	13sol_6
J_{SC1} (A/mm^2)	24.5	38	24.5	18.5	24.5	24.5
J_{SC2} (A/mm^2)	55	87	55	42	50	55
J_{SC3} (A/mm^2)	70.5	118	70.5	58.5	65.5	70.5
J_{SC4} (A/mm^2)	120.5	170	120.5	90.5	100	115.5
J_{SC5} (A/mm^2)	145	190	145	125	105	125
J_{SC6} (A/mm^2)	185	225	185	165	125	155
J_{SC7} (A/mm^2)	205	270	205	165	135	165
J_{SC8} (A/mm^2)	195	250	195	165	135	165
J_{SC9} (A/mm^2)	190	235	190	160	130	160
J_{SC10} (A/mm^2)	175	235	175	125	125	155
J_{SC11} (A/mm^2)	175	225	130	125	130	130
J_{SC12} (A/mm^2)	145	205	135	125	135	135
J_{SC13} (A/mm^2)	95	95	130	95	130	130

13sol_2 and 13sol_4 have capture magnets with magnetic field strengths $B_{c2} = 30$ T and $B_{c4} = 15$ T, respectively, the other four have $B_c = 20$ T. Set-ups 1,2 and 4 have magnetic field strength $B_d = 1.5$ T in the drift section and set-ups 3,5 and 6 have $B_d = 2$ T.
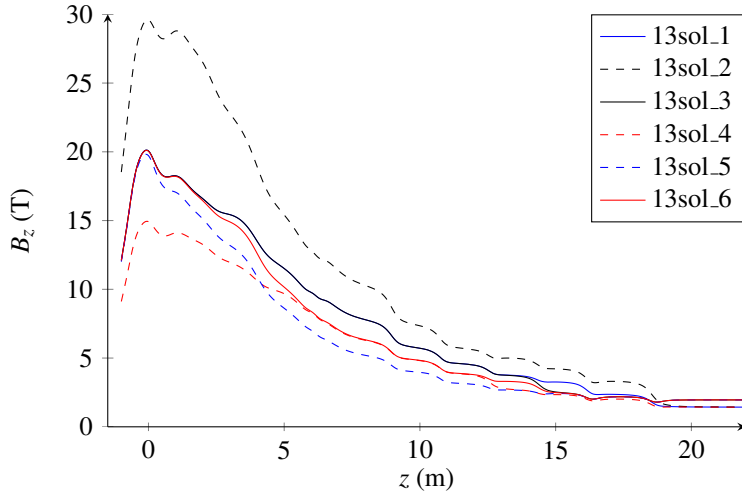
Figure 3.4: On-axis magnetic field tapering for six 13sol set-ups.

In figure 3.5 the relative muon count for each set-up is shown and compared with the ST2 result. The blue dots are the relative muon count without acceptance cuts, while the red dots are the relative muon count for acceptance cuts $\in A_{50}$. Without any cuts applied, set-ups indexed 3,5 and 6 have performance increase greater than 10% and they all have a higher magnetic field in the drift section $B_d = 2$ T. The performance of set-ups 1 ($B_c = 20$ T), 2 ($B_c = 30$ T) and 4 ($B_c = 15$ T) suggests that variations of the capture magnet's magnetic field strength $B_c \in [15, 30]$ does not improve performance.

When comparing the relative muon counts with acceptance cuts A_{50} the original ST2 has the highest performance. Specifically 13sol set-ups 3,5,6 ($B_d = 2$ T) have poorer performances ≈ 0.85. Comparing 13sol set-up 1 ($B_c = 20$ T), set-up 2 ($B_c = 30$ T) and set-up 4 ($B_c = 15$ T) shows an increased performance for higher values of the capture magnet's field strength B_c. Therefore, increasing the magnetic field strength in the drift section from $B_d = 1.5$ T to $B_d = 2$ T reduces performance, elongating the tapering section reduces the performance and increasing the capture magnet's field strength B_c increases performance.
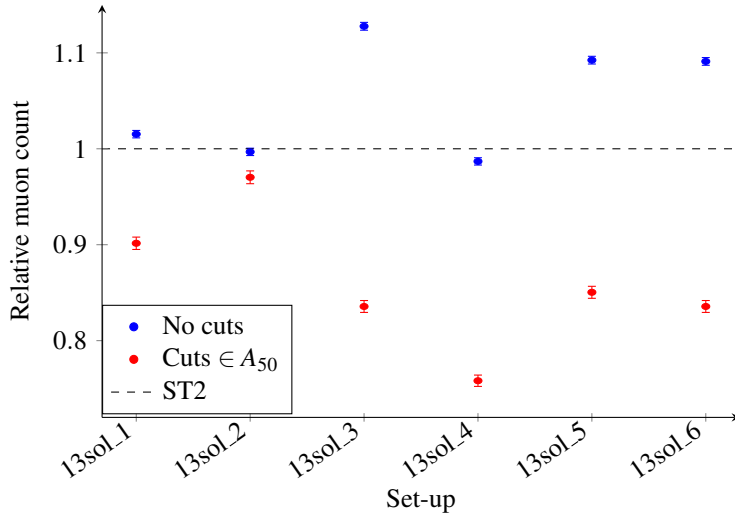
Figure 3.5: Relative muon count normalised to ST2 versus set-up. Error bars are statistical.

3.1.2 Shortening the tapering section

In light of the results from subsection 3.1.1, simplified set-ups with shorter tapering were implemented in G4BL with only 2 or 3 SC solenoid magnets. The set-ups are called 2sol or 3sol, respectively. The included magnets are the high field $B_c \approx 20$ T capture magnet and the drift section magnet, plus an intermediate magnet for 3sol. The ST2 resistive magnets listed in table 3.2 are also included. These ultra simple set-ups are shown in figures 3.6 and 3.7.

Figure 3.6: The 2sol solenoid magnet configuration from the G4BL-viewer.

Two 2sol_i and one 3sol set-ups with varying current densities J_i in the SC solenoids will be compared with the ST2 tapering. The 2sol_i and 3sol geometries and the current
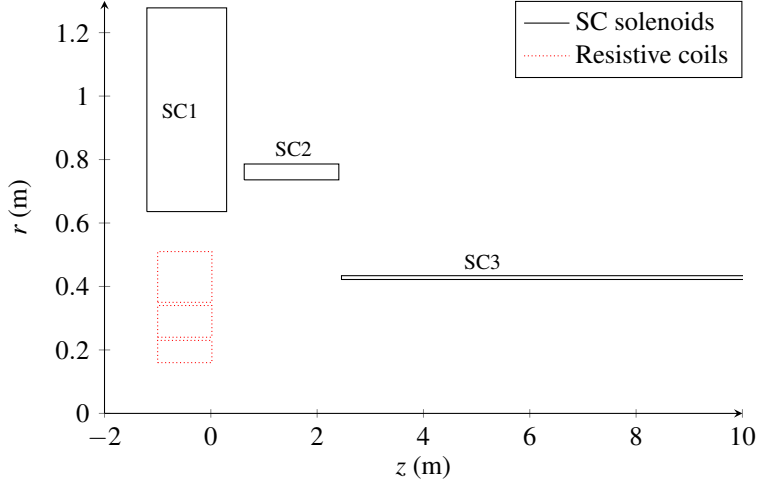
Figure 3.7: The 3sol solenoid magnet configuration. The picture shows the upper half of a vertical cut of the solenoids without shielding.

densities J_i are listed in tables 3.4 and 3.5. The 2sol_i variants are indexed $i \in [1, 2]$.

Figure 3.8 shows the magnetic field along the z-axis for the three short tapering variants, the 2sol_i tapering lengths are ≈ 2 m while 3sol tapering length is ≈ 4 m. All drift sections have a magnetic field $B_d = 1.5$ T except 2sol_1 where $B_d = 2$ T.

The relative muon count for these three alternative set-ups are shown in figure 3.9. The performance difference between applying and not applying acceptance cuts is notable for set-up 2sol_1. The magnetic field in the drift section of 2sol_1 is 2 T while the other set-ups all have 1.5 T in the drift section. Equation 2.7 is used to calculate the transverse momentum of a charged particle in the tapered magnetic field. The transverse momentum at the capture magnet is p_{Tc} and magnetic field is $B_c =$ for both set-ups, while $B_{d1} = 2$ T or $B_{d2} = 1.5$ T. The ratio between the two transverse momenta is

$$\frac{p_{Td1}}{p_{Td2}} = \frac{p_{Tc}\sqrt{\frac{B_c}{B_{d1}}}}{p_{Tc}\sqrt{\frac{B_c}{B_{d2}}}} = \sqrt{\frac{B_{d2}}{B_{d1}}}. \tag{3.1}$$

Table 3.4: Geometry and current densities of the two 2sol variants. z is the position of the upstream end of each element, Δz is the element length, R_i is the element inner radius, ΔR is the element thickness, and J_i is the current density. SC1-SC2 are superconducting solenoid magnets and Cu1-Cu3 are resistive coils.

	z (m)	Δz (m)	R_i (m)	ΔR (m)	J_1 (A/mm^2)	J_2 (A/mm^2)
SC1	-1.203	1.781	0.636	0.642	35.5	40
SC2	0.600	51.680	0.422	0.012	135	95
Cu1	-1.00	1.00	0.16	0.07	13	13
Cu2	-1.00	1.00	0.24	0.10	13	13
Cu3	-1.00	1.00	0.35	0.16	13	13

Table 3.5: Geometry and current densities of the 3sol. z is the position of the upstream end of each element, Δz is the element length, R_i is the element inner radius, ΔR is the element thickness, and J is the current density. SC1-SC3 are superconducting solenoid magnets and Cu1-Cu3 are resistive coils.

	z (m)	Δz (m)	R_i (m)	ΔR (m)	J (A/mm^2)
SC1	-1.203	1.50	0.636	0.642	32.5
SC2	0.347	1.78	0.70	0.050	50.5
SC3	2.458	50.0	0.422	0.012	95
Cu1	-1.00	1.00	0.16	0.07	13
Cu2	-1.00	1.00	0.24	0.10	13
Cu3	-1.00	1.00	0.35	0.16	13

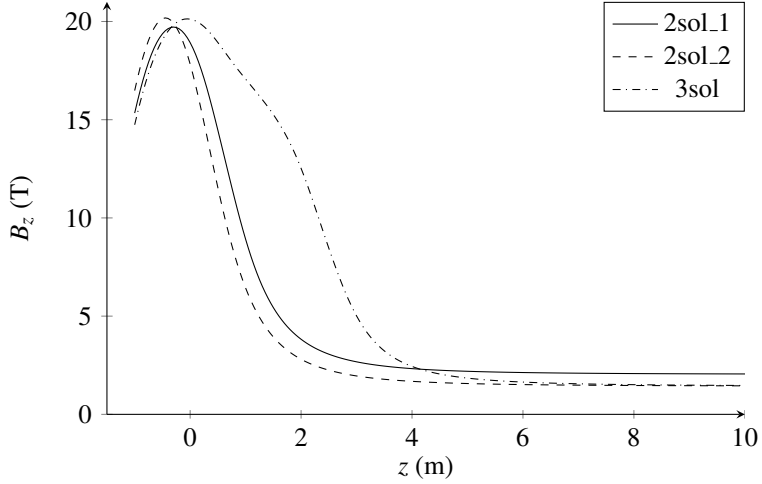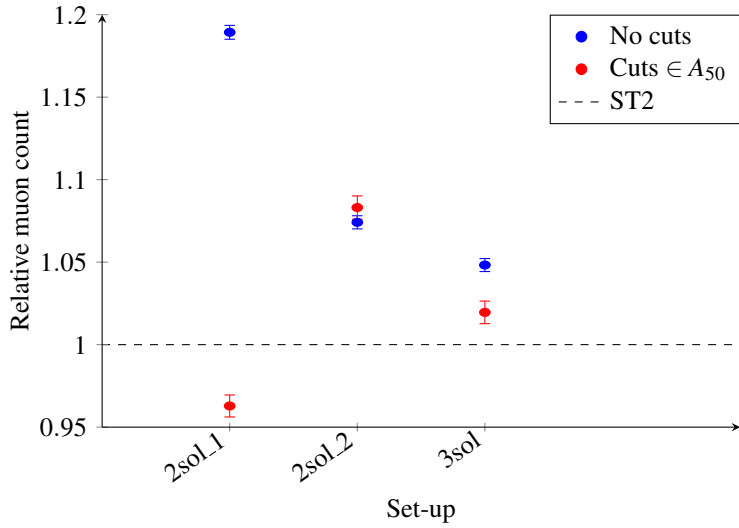Figure 3.8: On-axis magnetic field tapering with respect to z.

Figure 3.9: Relative muon count for the alternative set-ups.

Inserting these values gives a ratio of approximately 1.15, thus increasing the magnetic field in the drift section from 1.5 T to 2 T increases the transverse momentum of the particles at the drift section by approximately 15%. Therefore the relative muon count difference is larger between applying acceptance cuts and not applying acceptance cuts for set-up 2sol_1. Increasing the magnetic field strength B_d in the drift section reduces the performance.

When applying acceptance cuts the 2sol_2 and the 3sol are favoured over the ST2, as shown in figure 3.9. These rather surprising results suggest that a shorter tapering out-performs the longer tapering of ST2. A short tapering decreases the transverse momentum and increases the beam size and the longitudinal momentum quickly. The beam size quickly reaches its maximum size, and the quick momentum exchange between transverse and longitudinal momentum increases the overall performance.

If no cuts are applied set-up 1 with $B_d = 2$ T is favoured.

3.1.3 Optimising performance of alternative set-ups

So far the simple alternative 2sol and 3sol set-ups have not been optimised for performance. Since 2sol_2 showed the best performance in the previous subsection 3.1.2 it will be used for optimisation.

First the magnetic field in the capture section $B_c \in [10, 40]$ T will be varied while holding the field in the drift section constant at $B_d = 1.5$ T. Then the magnetic field in the drift section $B_d \in [0.75, 2.5]$ T is varied while the capture section field is held constant at $B_c = 20$ T.

The protons are bent proportional to the strength of the magnetic field, therefore the trajectory and the initial positions of the proton beam is affected when varying the magnetic field in the capture section B_c. To maintain an equal interaction region between the beam and the target when varying the magnetic field strength the intercept angle $\theta_{BT} = 30$ mrad and the azimuth angle $\phi = 144°$ between the proton beam and the target were fixed. The initial positions and the velocities at $z = -750$ mm in the capture section as the magnetic field strength in the capture section B_c varies is shown in figure 3.10.

The performance while varying the magnetic field strength in the capture section B_c is shown in figure 3.11. All variants are normalised to the performance of the original 2sol_2 ($B_c = 20$ T), with and without acceptance cuts; the black dotted line is the normalisation line. In both cases the muon yield seems to flatten out for $B_c > 20$ T, in particular for the case without cuts. The present NF baseline has a 20 T capture solen-
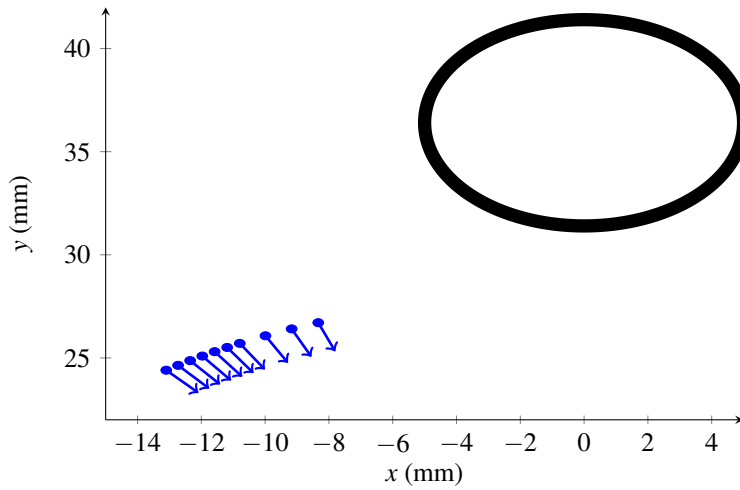
Figure 3.10: Initial positions at $z = -750$ mm (at arrow beginning) and transverse velocity directions of the proton beam with respect to the changing magnetic field in the capture section. The positions and velocity directions are sorted from right to left in increasing order of B_c =[10,15,20,25,27.5,30,32.5,35,37.5,40]. The black ring is the target surface.
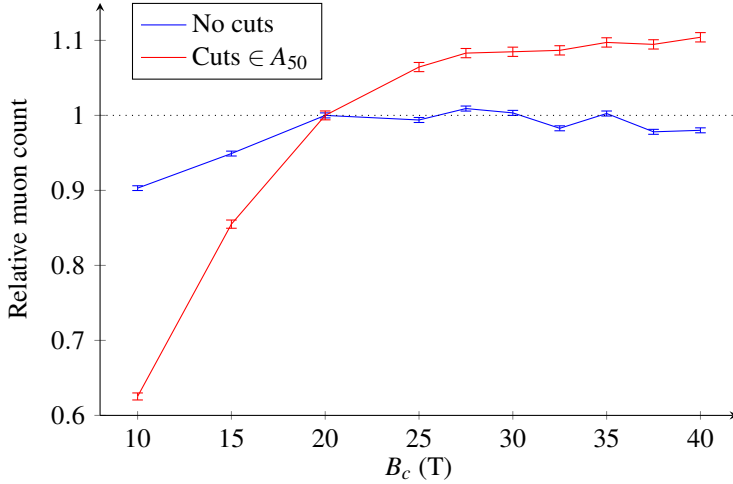
Figure 3.11: Relative muon count versus the peak magnetic field in the capture section. Error bars are statistical.

oid magnet, which is already a huge technical challenge. The performance increase of $\sim 6\%$ stepping up from $B_c =20$ to $B_c =25$ T has to be taken into account when deciding the size of the capture magnet. It is considered that the technical challenges of increasing the magnetic field by 5 T in the capture section to $B_c = 25$ T are bigger than gained performance. Therefore the magnetic field strength is kept at $B_c = 20$ for the further optimisation studies.

Figure 3.12 shows the performance while varying the magnetic field strength in the drift section B_d. The slope is positive up to a magnetic field strength $B_d < 1.5$ T where the performance peaks and the slope becomes negative for $B_d > 1.5$ T. No matching or tuning of the pre-accelerator and the drift section were done when varying B_d due to time constraints. As before equation 3.1 can be used to explain why the slope turns negative for $B_d > 1.5$ T when applying acceptance cuts. When the magnetic field in the drift section falls below 1.5 T the size of the beam grows too large and particles are lost when hitting the aperture. The optimal magnetic field strength in the drift section is $B_d = 1.5$ T.

Without any acceptance cuts the slope is always positive, higher field strength B_d improves the performance because the beam size is smaller and fewer particles hit the aperture.
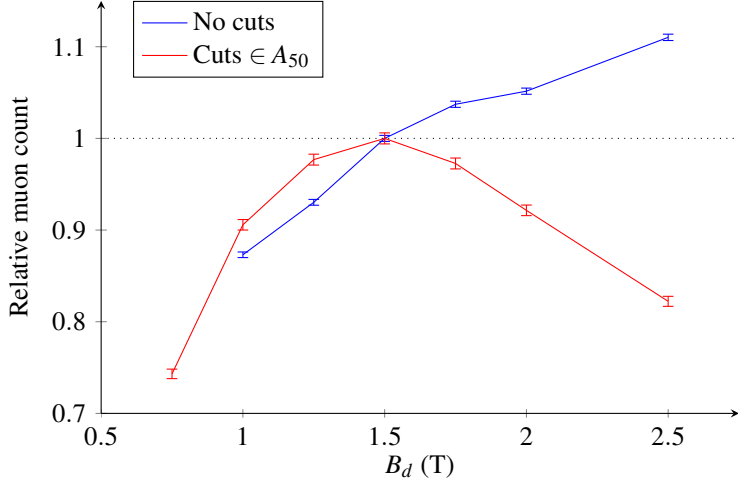
Figure 3.12: Relative muon count versus the on-axis magnetic field in the drift section. Error bars are statistical.

3.2   Optimisation studies including magnet shielding

Shielding is needed to protect the magnets from high energy deposition and radiation. The energy deposited is highest in close vicinity of the beam-target interaction region. In the interaction region the shielding has the shape of a cylinder with inner radius $r_1 = 75$ mm [4]. The tapering section has a conic shielding with linearly increasing inner radius $\in [r_1, r_2]$ over the tapering length. After the tapering the shielding is a cylinder with inner radius r_2. Figure 3.14 shows the shielding shape.

3.2.1   Fitting the magnet shielding to the alternative set-ups

The ST2a set-up was implemented in G4BL to replace the ST2 as the baseline; the ST2a is the successor of the ST2. The ST2a configuration consists of 93 SC magnets which smoothens the magnetic field compared to the ST2, as shown in figure 3.13. The inner radius of the original shielding for ST2a in the tapering section can be found as follows.

The inner radius of the magnet shielding is calculated assuming an adiabatic tapering and conservation of magnetic flux $\Phi = \pi B r^2$, where B and r are the magnetic field
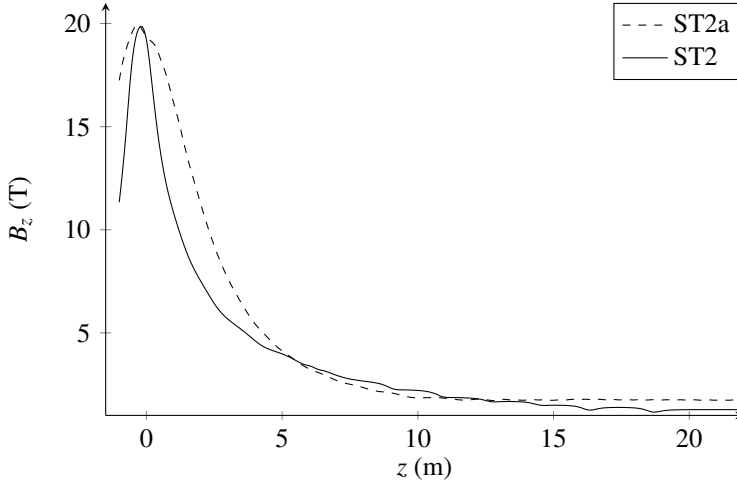
Figure 3.13: The magnetic fields of the ST2 and the ST2a.

strength and the inner shielding radius, respectively. From flux conservation

$$\pi B_1(z)r_1^2 = \pi B_2(z)r_2^2, \tag{3.2}$$

where the subscrips refer to different points along the tapering where the flux is con-
served. The inner shielding radius is a function of position along the z-axis. In the
ST2a set-up the magnetic field strength in the capture section is $B_c = 20$ T and in the
drift section $B_d = 1.75$ T. The inner shielding radius of the ST2a setup is $r_1 = 75$ mm at
the peak magnetic field strength in capture section and reaches $r_2 = 254$ mm at the drift
section where magnetic field strength is $B_d^{ST2a} = 1.75$ T [4]. Using equation 3.2, with
$B_1 = B_c = 20$ T and $B_2 = B_d = 1.75$ T, the boundary condition for the conic shielding
radius r_2 in the tapering section is calculated for ST2a. The same recipe is used for the
2sol and 3sol set-ups with $B_2 = B_d = 1.5$ T and the results are listed in table 3.6. The
original shielding cone radius increases from $r_1 = 75$ mm to $r_2 = 254$ mm in the inter-
val $z \in [0, 11.5]$ m, while the alternative shielding cone radius increases from $r_1 = 75$
mm to $r_2 = 274$ mm in the interval $z \in [0, 0.8]$ m.

   The shielding occupies a significant fraction of the volume inside the solenoids
and reduces the available beam phase-space volume. Shortening the conic region of
the shielding will increase the available beam phase-space volume and possibly the
performance, but leaving the solenoids more exposed to radiation and higher energy

Table 3.6: Parameters and shielding boundary conditions (in red) for the ST2a, the 2sol and the 3sol .

Set-up	Name	Parameter value	Boundary condition	Cone length
ST2a	Original shielding	$B_1 = 20$ T $B_2 = 1.75$ T	$r_1 = 75$ mm $r_2 = 254$ mm	11.5 m
2/3sol	Alternative shielding	$B_1 = 20$ T $B_2 = 1.5$ T	$r_1 = 75$ mm $r_2 = 274$ mm	0.8 m

deposition. The higher radiation and energy deposition is counteracted by inserting an intermediate solenoid SC2 with a higher inner radius $r_i^{SC2} = 736$ mm in between SC1 and SC3, as was the case for the 3sol. Figure 3.14 shows the geometry of the magnet configuration when the intermediate solenoid magnet SC2 is in place, the set-up is named after the number of solenoid magnets and thus it is called 3sol. In addition the
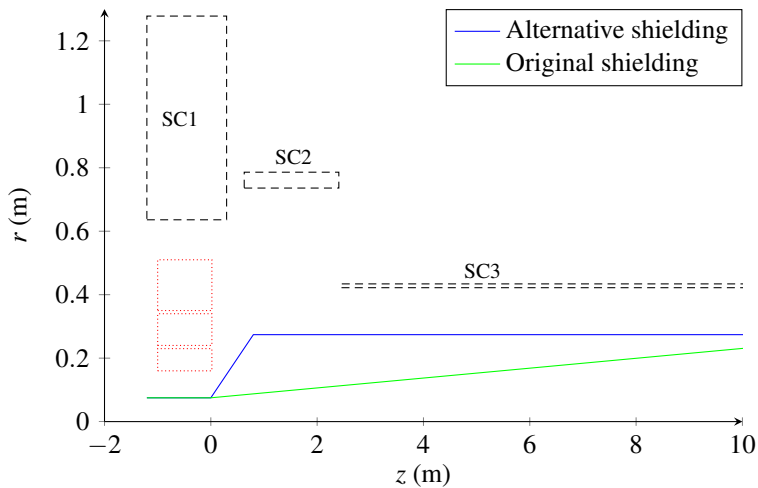
Figure 3.14: The alternative shielding inner radius set-up and the original inner radius set-up. The the upper half of a vertical cut of the solenoids and shielding is shown.

geometry of the alternative shielding is shown. The low magnetic field solenoid SC2 is assumed to withstand higher energy deposition than a high magnetic field solenoid. The shielding for SC1 is not changed, but for SC2 a quickly expanding shielding cone is preferred since the magnetic field tapering length is shorter.

A rapidly decreasing magnetic field tapering allows an increased shielding radius to conserve the magnetic flux. An increase of the shielding inner radius and a shortening of the cone length was done accordingly.

3.2.2 Magnetic field tapering variations

The alternative shielding is included in the 3sol set-up and the original shielding is included in the ST2a set-up. The 3sol performance will be optimised as follows. Magnetic field tapering variations are produced by changing the magnetic field in each SC solenoid, one at a time, while holding the others constant. Finally the 3sol variants with the alternative shielding are compared with the ST2a with the original shielding and the ST2a with the alternative shielding. The muon flux of ST2a with the original shielding at $z = 50$ m is listed in table 3.7.

Table 3.7: Performances of the ST2a with the original shielding baseline used for normalisation.

Set-up	Acceptance cuts	Muon Flux
ST2a	A_{50}	23671
	No	57731

Varying the magnetic field in SC1

The capture solenoid, SC1, is tuned to produce a magnetic field in the interval $B_{SC1} \in$ [10, 40] T. Solenoids SC2 and SC3 produce constant magnetic field strengths of $B_{SC2} = B_{SC3} = 1.5$ T. The magnetic field variations are shown in figure 3.15.

The graphs in figure 3.16 show the muon flux flatening out around $B_{SC1} = 25$ T. The relative muon count is normalised to the ST2a. The maximum magnetic field strength in SC1 is set to $B_{SC1} = 20$ T, taking into account the technical challenges of making a magnet producing a field higher than 20 T and the increased cost. The relative difference in muon flux between 20 and 25 T is 13%.

When the beam size is limited by the magnet shielding the magnetic field strength of SC1 B_{SC1} is of higher importance than when only limited by the magnet geometry (as in the previous section). The higher performance compared to the ST2a comes from the increased shielding inner radius of the alternative shielding.
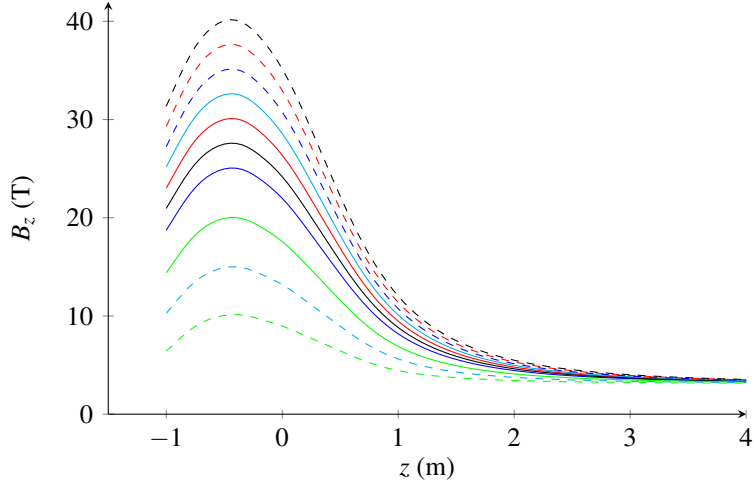
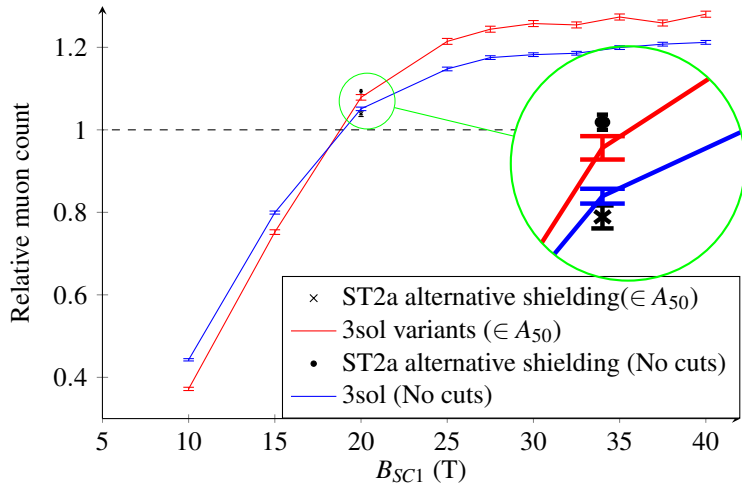Figure 3.15: Magnetic field variations in solenoid SC1.

Figure 3.16: Relative muon count when varying B_{SC1} normalised to the performance of ST2a. The green circle shows a magnification of the results for the non-standard set-ups.

SC1 produce a magnetic field of $B_{SC1} = 20$ T for all set-ups. The proton beam trajectory is influenced by the magnetic field **B**. Magnetic field variations would change the proton beam's entry position on the target, potentially causing unwanted particle production variations between set-ups. Minimising particle production fluctuations imposed by unmatched magnetic fields in the capture section have been emphasised when implementing all set-ups in G4BL (and later FLUKA).

The magnetic field strength B_z of all the 3sol set-ups have been matched to ST2a in the interval $z \in$[-750,-225] mm. (The proton beam emanates from $z = -750$ mm and the beam-target interaction region ends at $z = -225$ mm.)

Figure 3.17 shows the ratio between the 3sol and the ST2a on-axis magnetic field $R_{B_z} = B_z^{3sol}/B_z^{ST2a}$. The matched region is indicated by the red dashed lines. Errors ε_R
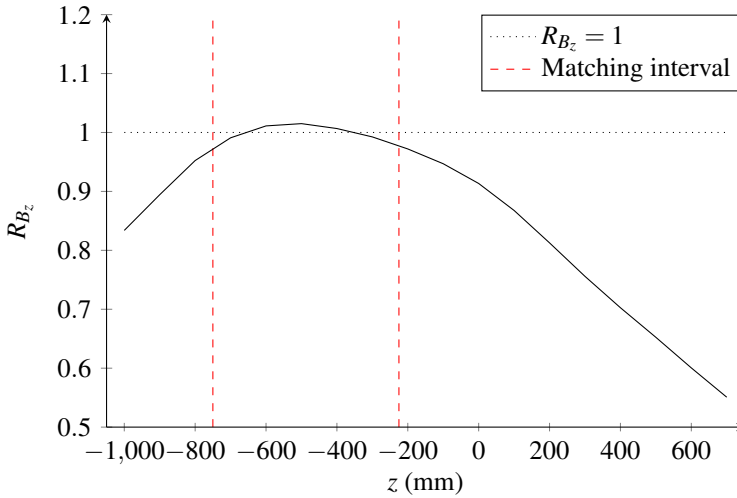
Figure 3.17: Ratio between the on-axis magnetic field for 3sol and ST2a.

of up to a few percent are acceptable $R_{B_z} \approx 1 \pm \varepsilon_R$.

Varying the magnetic field in SC3

The magnet strength of SC2 is set equal to SC3 $B_{SC2} = B_{SC3}$. The magnet strength of SC3 (and therefore SC2) is (are) varied from $B_d = 1$ T to $B_d = 2.5$ T. Again the muon flux of the ST2a with the original shielding is used for normalisation. The results are
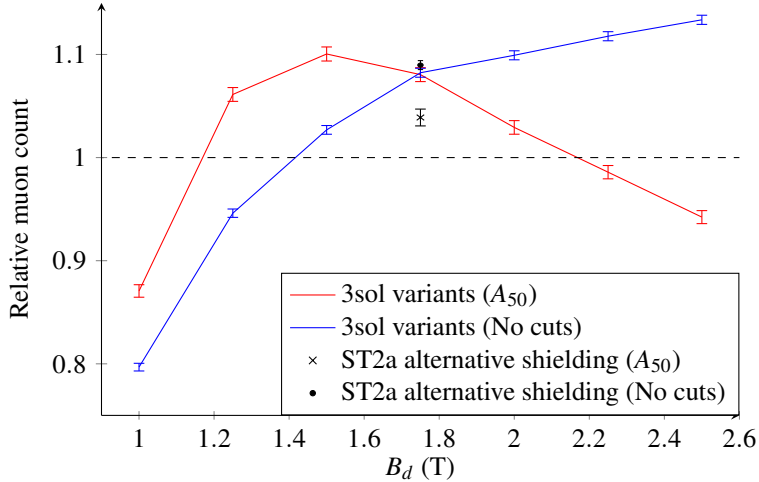
Figure 3.18: Relative muon count when varying the SC3 magnet strength from 1 to 2.5 T. Errorbars are statistical.

shown in figure 3.18. The performance peak is found, following the red line for the 3sol variants with acceptance cuts A_{50}, at a SC3 magnetic field strength of $B_{SC3} = 1.5$ T. In this case the the performance is approximately 8 % higher than the ST2a.

Varying the length of SC2

The drift section of the 3sol set-up begins at solenoid SC3 where $z \approx 2.5$ m and the drift section of the ST2 begins at $z \approx 6.3$ m. The solenoids in the drift section have lower magnetic fields and lower inner radii than the solenoids placed further upstream. In the 3sol set-up elongating the SC2 solenoid and thereby pushing the drift section further downstream and increasing the magnetic field in solenoid SC2 might increase the performance. In addition the larger inner radius of the solenoid could allow for thicker shielding. Therefore, the length of solenoid SC2 is varied in the interval $L_{SC2} \in [3.5, 7.0]$ m. The current density J in SC2 for the 3sol is held constant and produce a magnetic field of $B_{SC2} \approx 3.5$ T. Three alternative versions of the 3sol with longer SC2 magnet lengths were considered and the resulting on-axis magnetic field strength B_z is shown in figure 3.19.

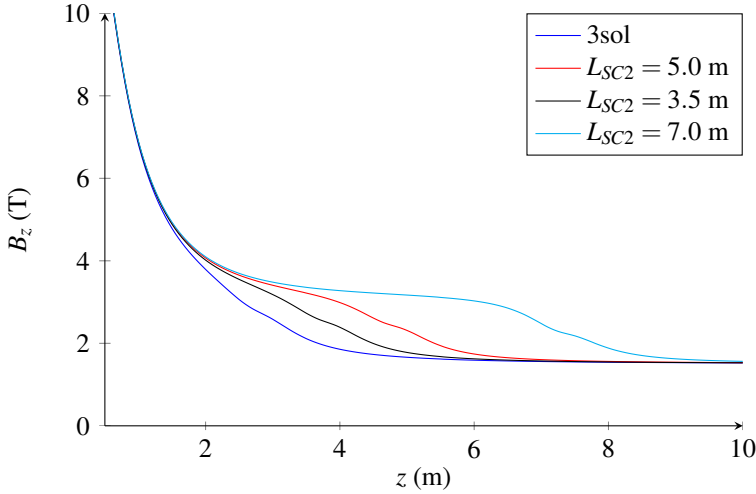Figure 3.20 shows the relative muon count, normalised to the 3sol, when varing the

Figure 3.19: The on-axis magnetic field strength B_z with respect to z for alternative 3sol set-ups with varying SC2 magnet lengths L_{SC2}.

length of SC2 $L_{SC2} \in [3.5, 7.0]$ m. The performance increases approximately 2% when the SC2 magnet length is increased to $L_{SC2} = 7.0$ m, the drift section is thereby shifted downstream.

Varying the magnetic field in SC2

The magnetic field produced in a $L_{SC2} = 7.0$ m long solenoid SC2 is varied in the interval $B_{SC2} \in [1.8, 8.8]$ T, while the magnetic field produced by solenoids SC1 and SC3 are held constant at $B_{SC1} = B_c = 20$ T and $B_{SC3} = B_d = 1.5$ T, respectively. Figure 3.21 shows the on-axis magnetic field for the ST2a and the 3sol variants. The 3sol variants are indexed in the interval $\in [1, 8]$ and ordered from lowest to highest magnetic field strength at the centre of SC2 ($z \approx 3.8$ m) and compared with the ST2a.

The performance with and without acceptance cuts for each 3sol variant is compared and normalised to the performance of the ST2a in figure 3.22. The blue line are the 3sol variants without acceptance cuts sorted from lowest to highest magnetic field strength in SC2. The black marks are for the ST2a tapering with the alternative
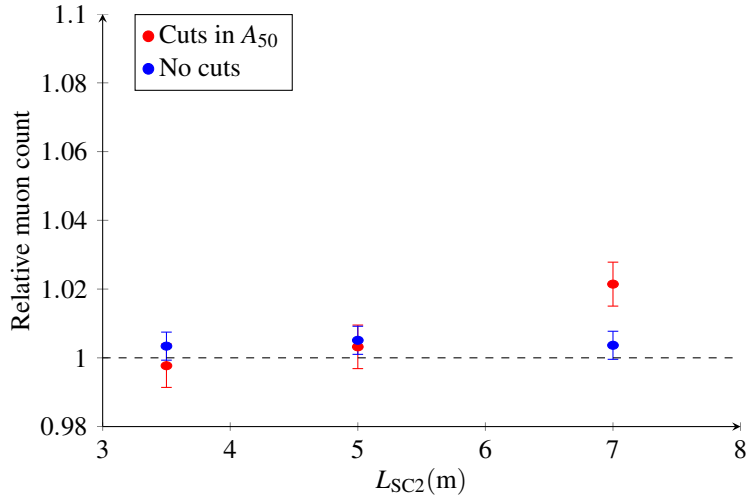
Figure 3.20: Relative muon count with respect to the length of SC2 L_{SC2}. Error bars are statistical.
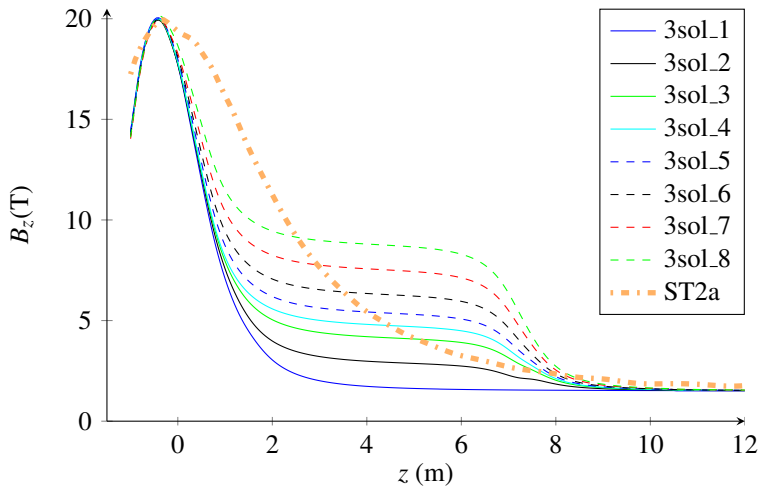

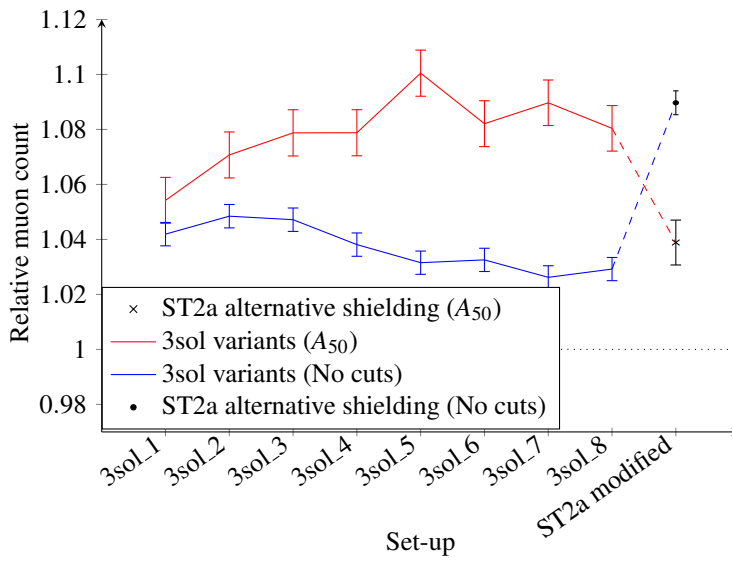Figure 3.21: Magnetic field variations in solenoid SC2 compared with the ST2a.

Figure 3.22: Relative muon count versus set-up. The magnetic field B_{SC2} can be read-off figure 3.21. Error bars are statistical.

shielding and the standard shielding. All error bars are statistical.

The red line with statistical error bars show the 8 different 3sol variants sorted from lowest to highest magnetic field strength in SC2. 3sol_5 has the highest performance approximately 10 % higher than the ST2a. The 3sol variants also out-perform the ST2a without acceptance cuts, but the ST2a with the alternative shielding has the best performance without acceptance cuts.

The momentum distributions for the 3sol_5 and ST2a with the alternative shielding are compared in figure 3.23. The two dashed lines show the muon momentum distribu-
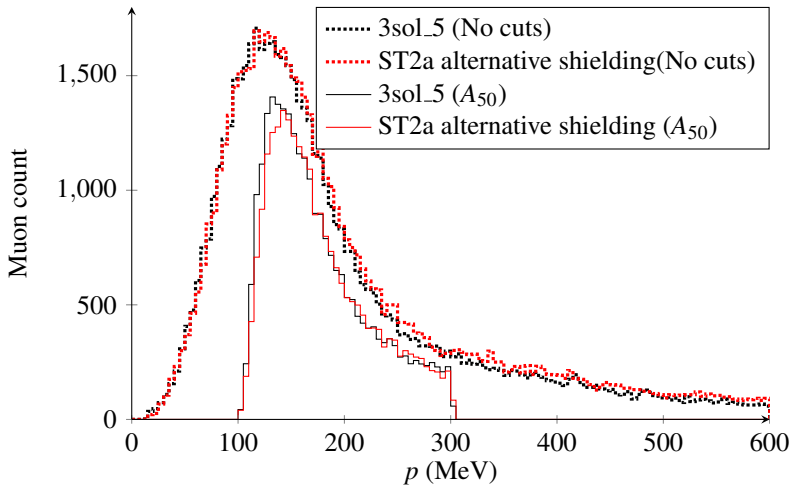
Figure 3.23: Muon momentum distributions of the ST2a and the 3sol_5 shown in red and black, respectively.

tions without any acceptance cuts, while the two solid lines show the muon momentum distributions with acceptance cuts $\in A_{50}$. Without acceptance cuts the ST2a with the alternative shielding captures more higher momentum muons, but they are rejected by the accelerator.

3sol_5 captures a higher number of muons within the acceptance cuts $\in A_{50}$. The 3sol_5 has a magnetic field strength of $B_{SC2} = 4.8$ T in the SC2 which is the optimal.

The magnetic field strength was optimized in each of the SC magnets, varying the magnetic field strength in only one magnet at a time. The optimised alternative 3sol set-up gives a higher yield compared to the baseline set-up (ST2a).

Length of the drift section (SC3)

The muon density in the capture, tapering and drift sections is influenced by competing processes. Pion decays contribute to muon density increase, while muon decays and muon loss due to scraping in the shielding leads to muon density decrease.

The pion decays can be seen as a muon source which weakens with time. Muon density increase dominates in the beginning of the capture, tapering and drift sections, when the muon source is strong (meaning high pion density and pion decay rates). As the muon source weakens with time (space) and the pion density decreases, muon loss will eventually dominate.

A longer drift section is added to the 3sol_5 set-up by elongating magnet SC3. Magnet SC3 now stretches down to $z \approx 60$ m. Changes in particle count are investigated in the interval $z \in [10, 60]$ m to find the optimal length of SC3. Time cuts $t \in [160, 240]$ ns are removed from the normal acceptance cuts A_{50} and denoted A_{50}^{-t}.

Figure 3.24 shows the change in particle count over the change in distance or the (approximate) particle gradient $\Delta N / \Delta z = (N_{i+1} - N_i)/(z_{i+1} - z_i)$ muons/mm versus the forward selected z_{i+1}-position along the NF centre line. The muon gradient is positive
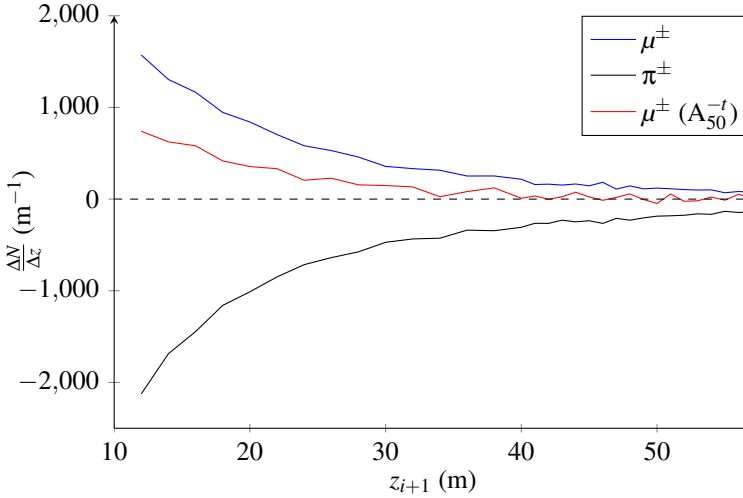

Figure 3.24: (Approximate) particle gradient with respect to the z_{i+1}-position for pions and muons (with and without acceptance cuts).

and decreasing along the z_{i+1}-axis while the pion gradient is negative and increasing.

Soft pions decay at low z_{i+1}-values and hard pions decay further downstream, which is reflected in the evolution of the muon gradients.

The muon gradient is approximately zero muons/mm for acceptance cuts $\in A_{50}^{-t}$ (red line) when $z_{i+1} \gtrsim 30$ m. The muon gradient without cuts are positive for all z_{i+1}, but higher momentum pions decay to higher momentum muons further downstream, these hard muons are not in the acceptance cut intervals $\in A_{50}^{-t}$.

Having a drift section reaching further downstream than z ≈ 30 m does not increase muon density. Injecting the beam into the buncher at z ≈ 30 m would reduce the solenoid length L_{SC3} by approximately 20 m and reduce building costs without loss in performance.

This study was limited to the study of the capture, the tapering and the drift sections. Shortening the drift section changes the longitudinal position-energy correlation and a denser muon beam will be injected to the buncher. This would most likely also require a re-optimisation of the pre-acceleration. Further work on the pre-acceleration is beyond the scope of this thesis.

Comparing simulation results from G4beamline and FLUKA

Simulation software, like G4BL and FLUKA, are under continuous development and frequently updated, some studies comparing simulation results with experimental results are reported in e.g. [32] and [33]. The HARP experiment's homepage has a thorough list of publications e.g. related to hadron production [34]. The choice of using G4BL was coincidental, in fact any suitable simulation tool could have been used.

A study using FLUKA [10] is done to compare the results obtained with G4BL. The 3 set-ups called 3sol, ST2a and ST2a with the alternative shielding are implemented in FLUKA. Figure 3.25 shows a picture of 3sol from FLUKA.

Figures 3.26 and 3.27 show the transverse momentum p_T distributions and the radius r distributions of the muon influx to the buncher for the ST2a set-up obtained from G4BL and FLUKA. The muon count is much higher for G4BL than FLUKA with identical beam and target parameters. When normalising the G4BL distribution to the FLUKA ditribution, they are very similar. The normalisation ratio is $N_{G4BL}/N_{FLUKA} = 1.67$.

Figure 3.28 shows the momentum distribution p of the muon influx to the buncher. The momentum distributions of G4BL and FLUKA differ significantly. G4BL produces a softer distribution than FLUKA, both peaks are located at approximately the
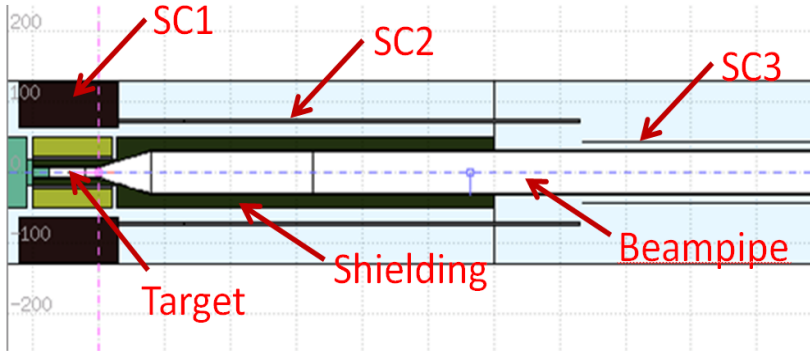
Figure 3.25: The 3sol_5 set-up from FLUKA. SC1, SC2 and SC3 are superconducting solenoids. The beampipe is the white region in the centre.
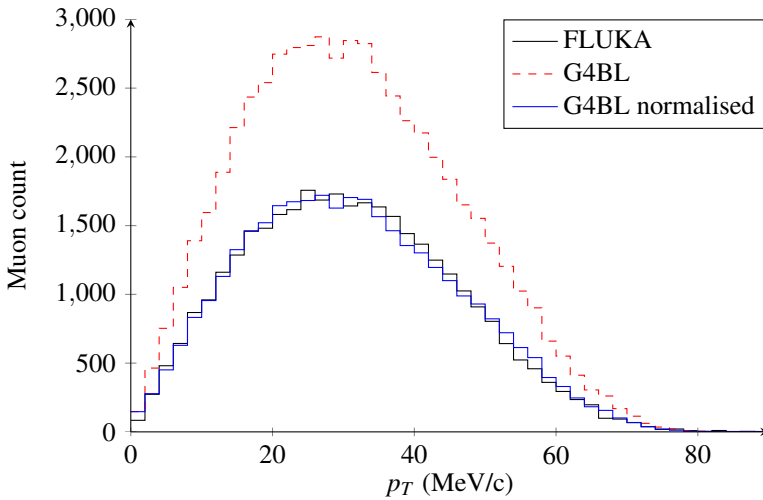
Figure 3.26: Transverse momentum p_T distribution for G4BL in red and FLUKA in black at $z = 50$ m for the ST2a set-up. The blue histogram shows the G4BL distribution normalised to the FLUKA distribution.
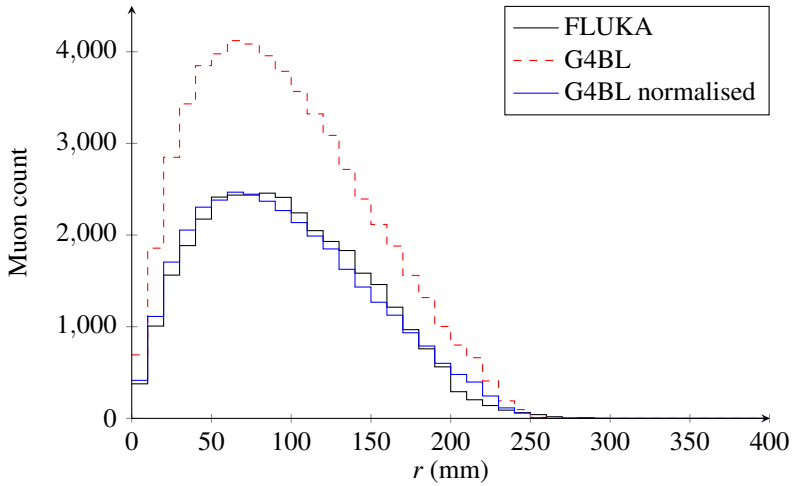
Figure 3.27: Radius r distribution from G4BL in red and from FLUKA in black at $z =$ 50 m for the ST2a set-up. The blue histogram shows the G4BL distribution normalised to the FLUKA distribution.
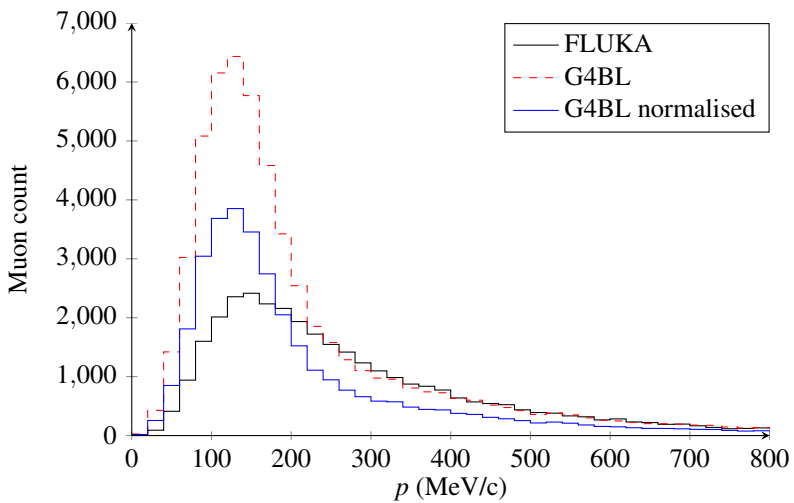
Figure 3.28: Momentum distribution p from G4BL in red and from FLUKA in black at $z = 50$ m for the ST2a set-up.

same momentum value $p \approx 150$ MeV/c, but the harder FLUKA distribution is more right-skewed.

For the harder muon momentum spectrum $p \gtrsim 220$ MeV/C the red dashed and black solid lines overlap, resulting in similar time t distributions when $t \lesssim 190$ ns, shown in figure 3.29. The time distribution peaks are located at $t \approx 170$ ns. FLUKA
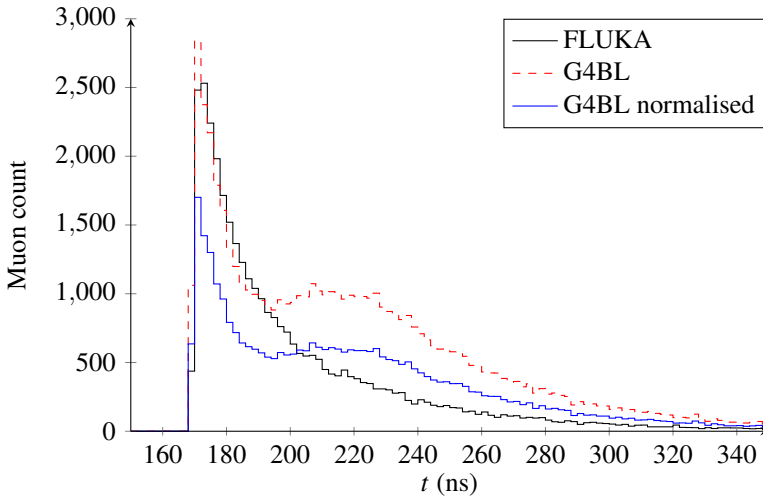
Figure 3.29: Time distribution t from G4BL in red and from FLUKA in black at $z = 50$ m.

gives a t-distribution which falls of quickly with time, while G4BL has a plateau in the interval $t \in [190, 240]$ ns due to the large fraction of muons found in the softer muon momentum spectrum $p \lesssim 210$ MeV/c. Notice the small bin size of $t = 2$ ns, chosen to clearly visualise the shape of the plateau and the differences between G4BL and FLUKA.

Different particle production models are used in FLUKA and G4BL, resulting in different longitudinal momentum distributions and muon counts. Worrying as this might be, both simulation tools favour the alternative 3sol_5 set-up over the ST2a as shown in figure 3.30 where the relative muon counts from FLUKA and G4BL are compared. The relative muon flux of the 3sol_5 is ∼10-14 % higher than for the ST2a when acceptance cuts A_{50} are applied.
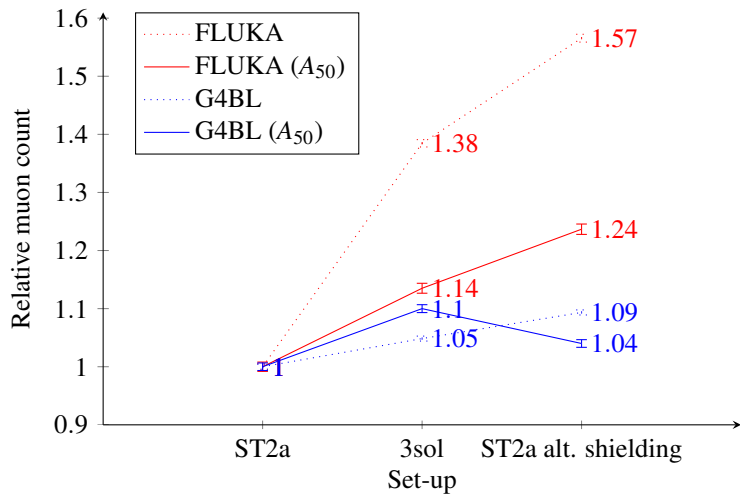
Figure 3.30: Comparing results from the simulation tools G4BL and FLUKA. The G4BL results are shown in blue and the FLUKA results are shown in red. The solid lines show the results with acceptance cuts A_{50} and the dotted lines show the results without acceptance cuts.

3.3 Summary

Optimisation of the magnetic field and magnet shielding layout in the capture, the tapering and the drift sections for an alternative set-up has been performed. The optimisation without any shielding, showed that a shorter magnetic field tapering is a good alternative to the longer adiabatic tapering of the baseline set-ups (ST2 and the ST2a). A shorter tapering allows for lower currents in the SC magnets, specifically the lower current in solenoid SC2 of the 3sol set-up may allow for a larger solenoid radius thereby exposing it to less radiation.

A rapidly decreasing magnetic field tapering allows an increased shielding radius to conserve the magnetic flux. An increase of the shielding inner radius and a shortening of the cone length was done accordingly and the resulting muon count was increased. The magnetic field strength was optimized in each of the SC magnets, varying the magnetic field strength in only one magnet at a time. The optimised alternative 3sol set-up gives a higher yield compared to the baseline set-up (ST2a), for both FLUKA and G4beamline.

Table 3.8 shows the most important results with and without acceptance cuts A_{50} for G4BL and FLUKA. According to the G4beamline simulations, 3sol is better than

Table 3.8: Relative muon count with and without acceptance cuts A_{50} compared to the reference ST2a.

Set-up	No cuts		A_{50}	
	G4BL	FLUKA	G4BL	FLUKA
ST2 alternative shielding	0.93	-	0.96	-
ST2a alternative shielding	1.09	1.57	1.04	1.24
3sol_5	1.05	1.38	1.10	1.14

both the baseline (ST2a) and the ST2a set-up with the alternative shielding. The results from FLUKA suggests that the 3sol is better than the baseline (ST2a) and the ST2a with the alternative shielding is even better than the 3sol. However, reducing the shielding thickness for the ST2a magnet set-up increases the radiation on the magnets.

When studying the length of the drift section it was shown that the length could be shortened by approximately 20 m, delivering a denser muon beam, without performance loss at the buncher. The performance of the buncher when receiving a denser muon beam needs further study.

The simulation tool FLUKA seems to be more sensitive to a change in shielding layout than G4beamline, increasing the muon flux with 24 % for the ST2a with the

alternative shielding and 57% without acceptance cuts. The optimised 3sol set-up is shown in figure 3.31 and the geometric parameters listed in table 3.9.
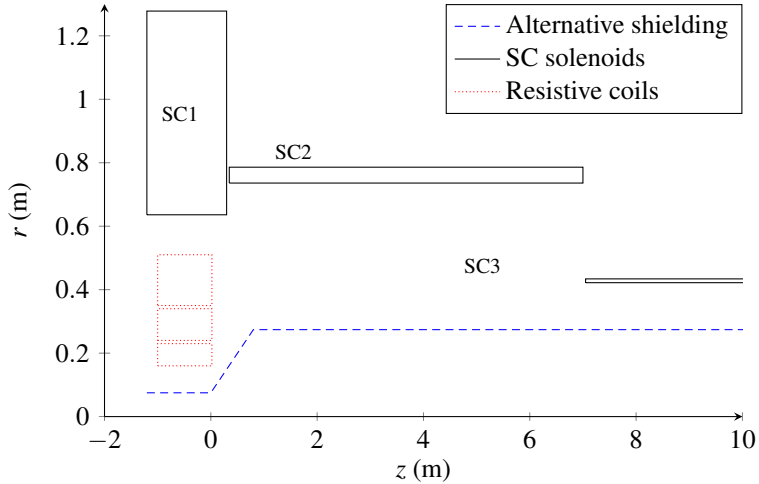
Figure 3.31: Optimised 3sol geometry.

Table 3.9: Geometry and current densities of the optimised 3sol variant. SC1-3 are superconducting solenoid magnets and Cu1-3 are resistive coils.

	z (m)	Δz (m)	R_i (m)	ΔR (m)	J (A/mm^2)
SC1	-1.203	1.50	0.636	0.642	32.5
SC2	0.347	7.00	0.70	0.050	75.0
SC3	7.397	50.0	0.422	0.012	95
Cu1	-1.00	1.00	0.16	0.07	13
Cu2	-1.00	1.00	0.24	0.10	13
Cu3	-1.00	1.00	0.35	0.16	13

The optimised 3sol_5 set-up has a 10% higher yield than the ST2a. Combining the optimisations of chapter 2 (optimised beam parameters for particle production) and chapter 3 (optimised capture and tapering sections) the optimal set-up increases the muon yield by another 6 %, up to a total increase of approximately 16 % compared to

Figure 3.32: Optimisation results. The relative muon count versus the optimisations.

the ST2a as shown in figure 3.32.

Chapter 4

The Muon Ionisation Cooling Experiment (MICE)

In this chapter the momentum distribution of the muon beam from the Muon Ionisation Cooling Experiment (MICE) beam line is studied. The muon beam entering the cooling section of the Neutrino Factory has a symmetrical momentum distribution[5]. The MICE cooling channel is based on the Neutrino Factory Feasibility study 2 (ST2), therefore the goal of 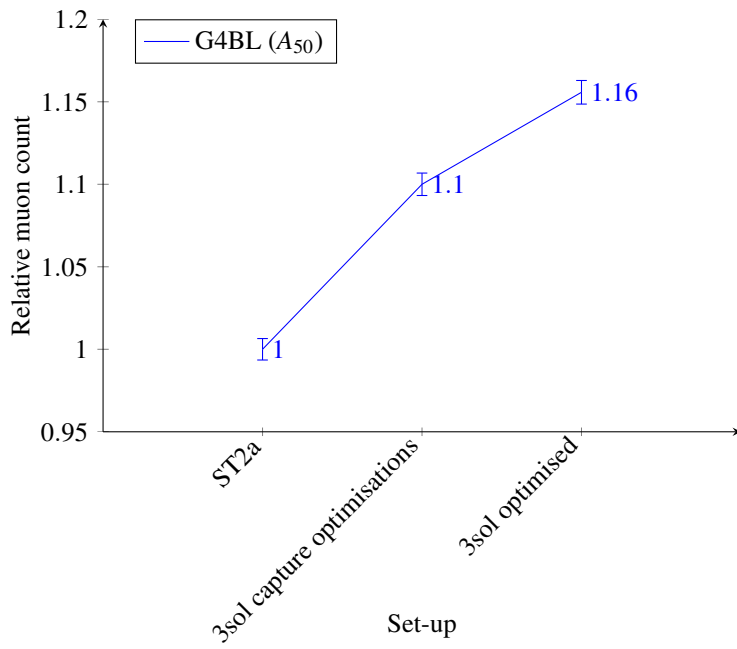the study is to provide MICE with a muon beam with a symmetrical momentum distribution. Monte Carlo simulation results are compared with data from MICE. The main results are published in [35].

In addition estimates of the pion contamination in the MICE muon beams is performed by Monte Carlo simulations. The main results are published in [36].

Section 4.1 contains a general description of the MICE facility, while section 4.2 and on-wards describes the specific studies carried out as part of this thesis, unless otherwise stated.

4.1 Introduction to MICE

The Muon Ionisation Cooling Experiment (MICE) is an ongoing and under construction, proof-of-principle experiment at Rutherford Appleton Laboratory (RAL) in the UK. It is aimed at providing the ultra-fast muon cooling from ionisation, several times faster than the muon decay time of 2.2 μs [37].

Staging of MICE is divided in 3 steps, the so-called Step I, Step IV and Step V, due to availability of hardware and effort. Each step is commissioned with important

upgrades for the final step [13].

MICE has finished Step I, the beam and the detectors have been commissioned and the upcoming Step IV is planned to run (2014) 2015 and 2016 and Step V in 2017.
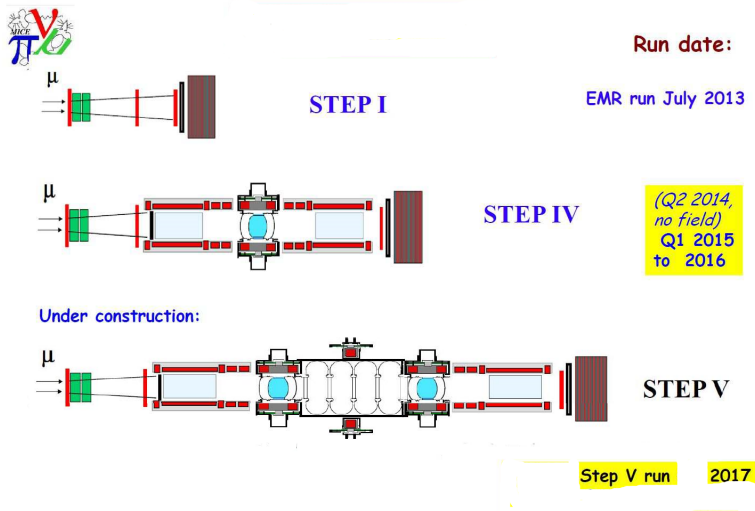
Figure 4.1: MICE staging plan and time frame.

4.1.1   Brief description

Ionisation cooling is a technique to decrease the phase-space occupied by a beam. A large sized beam is focussed onto an absorber where the beam loses energy through ionisation (cooling) at the same time as multiple scattering will deflect particles and increase the beam size (heating). The normalised emittance change can be calculated by

$$\frac{d\varepsilon_N}{dX} \approx -\frac{\varepsilon_N}{\beta^2 E_\mu}\left\langle\frac{dE}{dX}\right\rangle + \frac{\beta_t(0.014 GeV)^2}{2\beta^3 E_\mu m_\mu X_0}, \tag{4.1}$$

where X is the material thickness, X_0 is the radiation length of the medium, β is the velocity, β_t is the betatron function, E_μ is the muon energy and m_μ is the muon mass [38]. The negative part gives emittance reduction through energy loss (the positive part emittance increase through multiple scattering). It is therefore important that the

energy loss is dominant to achieve cooling. Re-acceleration of muons is done by the RF cavities, restoring the longitudinal momentum to its original value after it has traversed the absorber. The decreased transverse momentum is not restored and the emittance is reduced.

The experiment, shown in figure 4.2, will use one cooling lattice cell based on the
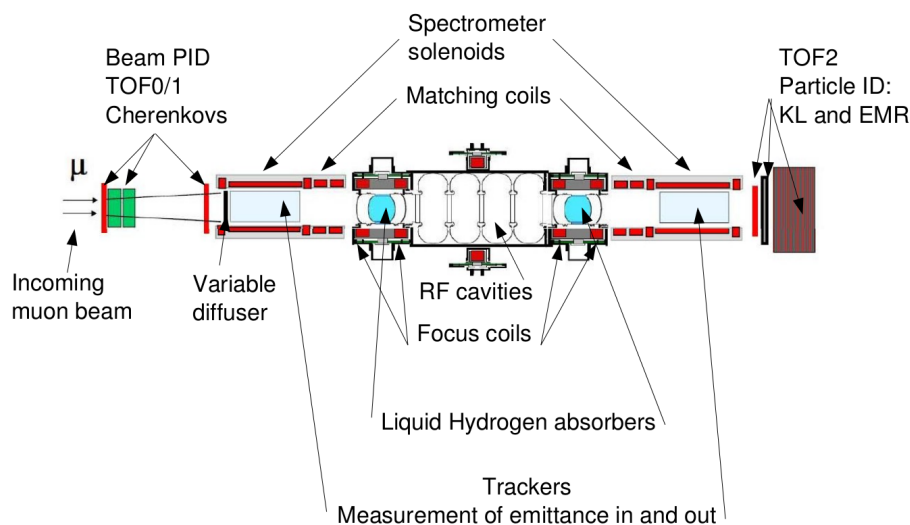
Figure 4.2: Cartoon of the MICE layout, muons come from the MICE beam line, shown in figure 4.3.

design of the Neutrino Factory Feasibility Study 2. All lattice details can be found in [5]. Multiple scattering and energy loss in materials change with the beam energy or momentum. Three beam momentum settings will be use for the emittance measurements in the momentum region where the NF will operate, see table 4.1. This will make it possible to compare real-life data with simulation data and improve accuracy of simulation tools. More accurate simulations will be an advantage when designing the cooling section for the NF and μC, improvements may change the current baseline before it is finally frozen and built.

Several detectors are present along the beam line and they will be used for particle identification and emittance measurements. These include a scintillator counter, time-of-flight (TOFx) detector, Cherenkov detectors (CKOWab), a scintillation tracker inside a solenoid, a calorimeter (KL) and an Electron Muon Ranger (EMR).

The beam entering MICE hits a diffuser, with varying thickness. The diffuser increase the divergence of the beam to allow for different emittance ε_N settings, shown in figure 4.2. On each end two trackers measure the emittance, while the other detectors take care of particle identification. Three low Z, liquid hydrogen, absorbers will provide cooling. The lost longitudinal momentum is restored by two accelerating RF-cavities. The goal is high precision measurement of relative emittance-change to 1% of its value, $(\varepsilon_0 - \varepsilon_1)/\varepsilon_0 \approx 0.01$.

The cooling properties of liquid hydrogen, lithium hydride and other absorber materials will be investigated. using optics configurations with varying momentum, emittance, beam polarity and magnet polarisation.

MICE will prove, if successful, the principle of ionisation cooling. Ionisation cooling is an essential step towards building a NF and/or a Muon Collider (μC). The standard scheme is to build the NF before the μC, since the μC essentially has the same front-end and may be seen as an extension of the NF. Furthermore the μC relies on a more complex cooling (including longitudinal) in 6D, while MICE (and NF) is (are) designed for 4D cooling.

The MICE beam line

The MICE beam line has two modes, one mode provides a muon beam to the experiment (muon mode) and the other mode provides a beam with pions, muons and electrons (positrons) to the experiment (pion mode). The MICE beam line is shown in figure 4.3.

The protons needed for production of pions come from the ISIS proton beam. A titanium target is dipped into the beam for $t \approx 2$ ms producing a secondary low intensity beam. The secondary pions are captured by a quadrupole triplet (Q1-3) before momentum selection is provided by a dipole (D1) where the beam is rotated an angle of $60°$.

In the muon mode the captured pions are left to decay to muons in the decay solenoid (DS) which focusses the beam towards a second dipole (D2). At dipole D2 the tertiary muons experience momentum selection and a rotation of $30°$. The muon beam is then guided and shaped to a given size and divergence by two quadrupole triplets (Q4-6 and Q7-9) before it hits the diffuser and the proceeding cooling section. The time-of-flight distribution between TOF0 and TOF1 of the beam from muon mode is shown in figure 4.4. The distribution shows a large muon peak at approximately 28 ns and a small electron peak at approximately 26 ns.

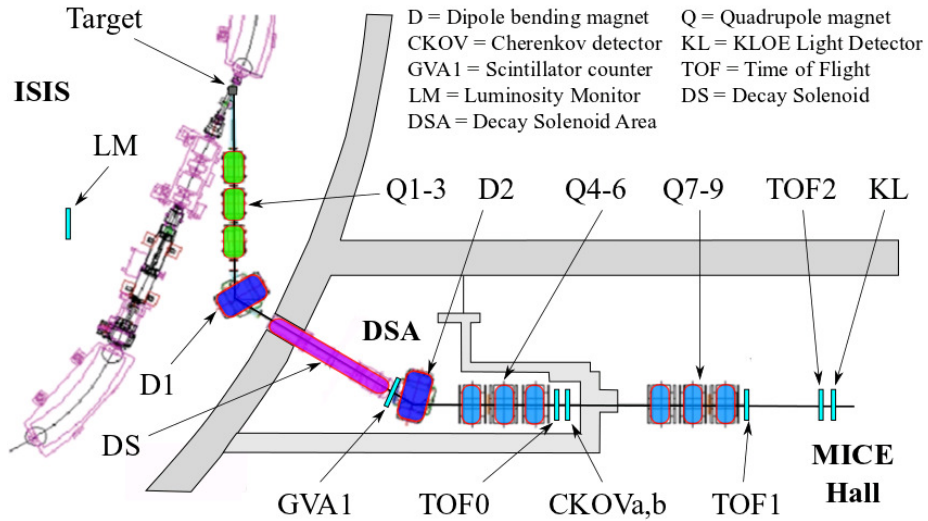In pion mode dipole D2 is used to select pions at approximately the same mo-

Figure 4.3: The MICE step I beam line set-up at RAL.
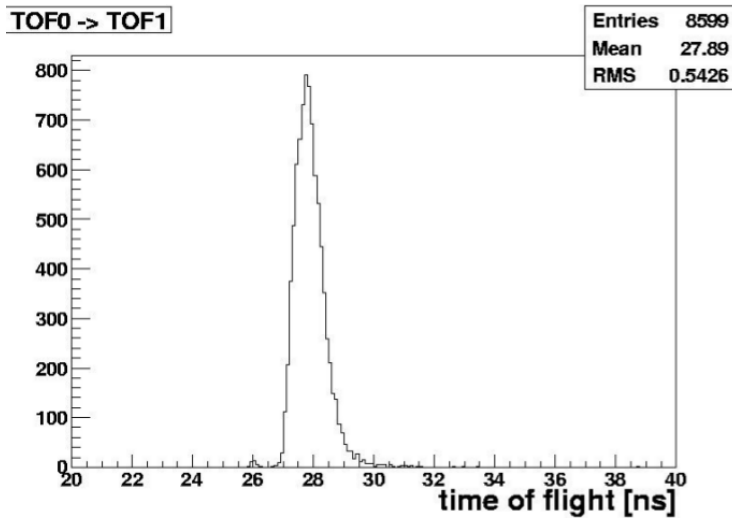
Figure 4.4: Time-of-flight distribution between TOF0 and TOF1 in muon mode.

mentum as at dipole D1, $p_{D1} \approx p_{D2}$. The time-of-flight distribution between TOF0 and TOF1 of the beam from pion mode is shown in figure 4.5. The distribution shows three
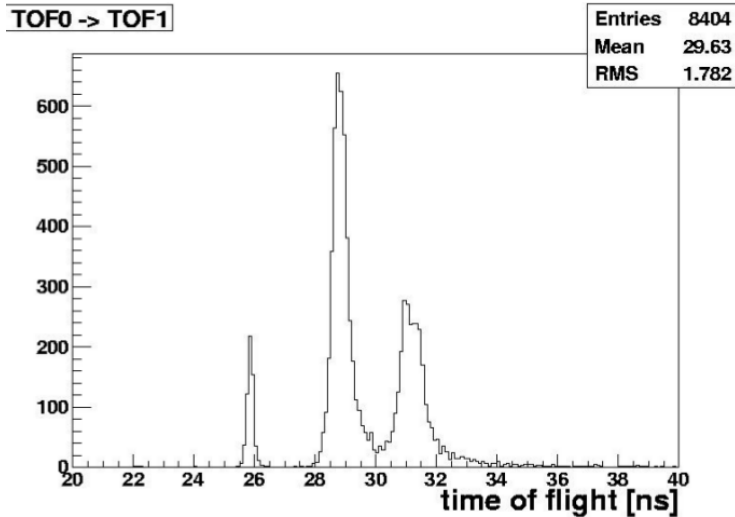
Figure 4.5: Time-of-flight distribution between TOF0 and TOF1 in pion mode.

peaks, the electron peak (26 ns), the muon peak (29 ns) and the pion peak (31 ns).

The beam line is designed to allow for three emittances and three beam momenta. Which gives us a total of 9 optics settings, in addition the design allows for both sign muon runs. Parameters and beam definitions at the diffuser are summarised in the emittance-momentum matrix, table 4.1. The emittances are ε_N =3, 6 and 10 mm rad and the beam momenta are p_z =140, 200 and 240 MeV/c for the experiment. It is stressed that these parameters are *input parameters* to the experiment, downstream of the absorber.

The beam emittance is increased by multiple scattering in a high Z-material, a diffuser. Lead diffusers of width from 5 to 15.5 mm changes the magnitude of the beam heating, increasing diffuser width increases heating.

To refer to the beam definitions the standard notation is on the following form

$$\varepsilon_N\text{-}p_z = 6\text{-}200,$$

for a ε_N =6 mmrad p_z =200 MeV/c beam.

Table 4.1: Mean momentum and emittance for the MICE beams in black. The emittance-momentum matrix, in blue, shows the beam's longitudinal momentum at the diffuser and diffuser thickness which results in the required beam for the experiment. The hyphen signifies no diffuser for $\varepsilon_N = 3$ mm rad.

| p_z(MeV/c) | ε_N (mm rad) | | | Units |
	3	6	10	
140	151	148	164	p_z (MeV/c)
	-	5	10	t (mm)
200	207	215	229	p_z (MeV/c)
	-	7.5	15.5	t (mm)
240	245	256	267	p_z (MeV/c)
	-	7.5	15.5	t (mm)

To characterise the beam a variety of particle detectors are placed along the beam-line, detector abbreviations in figure 4.3. Starting with the GVA1 between the DS and D2, CKOWa and b after the quadrupoles Q4-6. Three TOF detectors, one placed between Q4-6 and CKOVab, another after Q7-9 and the last one after the cooling channel. Finally one KLOE calorimeter (KL) and the EMR are place downstream of TOF2, see the following references for a description of the detectors [39], [40]. Table 4.2 includes all beam-line elements and placement, the upper half contains the beam optics elements and the proton absorber and the lower half contains the detectors. Traditional emittance measurement methods have a precision of ≈ 10 %, which is not sufficient for MICE. In order to comply with the high-precision measurement-requirements MICE uses a low beam intensity and a particle-by-particle detection system.

4.1.2 Step I

The first step aims at calibrating the detectors and characterising the beam, step I has been successfully finished.

Standard optics

Matching of the beam has to be done from the diffuser and backwards to the target since the beam is defined downstream of the diffuser. This was done in several steps, first by varying the magnet currents in the beam line until a match was found. Later detailed geometry of the MICE step I was implemented in G4BL. Using G4BL meant more accurate simulation results were available because it includes stochastic effects

Table 4.2: MICE step I beam line element details and placement positions measured from the target [40].

Element	Distance from target [along nominal beam axis]	L_{eff}	Max field/gradient		Aperture Radius (Pole tip)	1/2-aperture [H/V]	
	(mm)	(mm)	(T)	(T/m)	(mm)	mm	mm
Q1	3000.0	888		1.6	101.5		
Q2	4400.0	888		1.6	101.5		
Q3	5800.0	888		1.6	101.5		
D1	7979.1	1038	1.6			254.0	76.0
Decay Solenoid	12210.7	5000	5.7		57.5		
D2	15808.1	1038	0.85			254.0	76.0
Q4	17661.6	660		2.3	176.0		
Q5	18821.6	660		2.3	176.0		
Q6	19981.6	660		2.3	176.0		
Q7	25293.7	660		2.3	176.0		
Q8	26453.7	660		2.3	176.0		
Q9	27613.7	660		2.3	176.0		
Proton absorber	14880	Plastic sheets 15, 29, 49, 54 mm					
GVA1	15050.0	Scintillation counter (0.02 X_0)					
BPM1	16992.0	Scintillating fibres (0.005 X_0)					
TOF0	21088.0	Segmented scintillator (0.12 X_0)					
Ckova	21251.5	Aerogel threshold Cherenkov (0.019 X_0)					
Ckovb	21910.9	Aerogel threshold Cherenkov (0.031 X_0)					
BPM2	24293.7	Scintillating fibres (0.005 X_0)					
TOF1	28793.1	Segmented scintillator (0.12 X_0)					
TOF2	31198.1	Segmented scintillator (0.12 X_0)					
KL	31323.1	Lead + scintillator (2.5 X_0)					
Tag counters	31423.1	Scintillation bars (0.06 X_0)					

of particle interaction with matter. This resulted in the magnet currents summarised in table 4.3 [41]. The polarity of the currents depends on the charge of the particles the

Table 4.3: Magnet currents for the re-scaled TURTLE and genetic algorithm optical designs. Tilley and Roberts' (6 mm, 200 MeV/c) base line optical configuration is italicised.

Optical design	Polarity	ϵ_N (mm)	p_z (MeV/c)	Magnet current (Amps)											
				Q1	Q2	Q3	D1	DS	D2	Q4	Q5	Q6	Q7	Q8	Q9
Re-scaled TURTLE	μ^-	3	140	80.3	100.3	69.8	243.1	524.2	73.9	122.5	164.3	108.8	101.3	153.1	130.6
			200	97.7	122.0	84.9	305.0	637.9	91.5	153.4	205.7	136.4	133.9	202.5	172.9
			240	113.7	142.1	98.9	370.1	743.0	104.4	76.2	236.3	156.7	157.0	237.6	203.0
		6	140	81.9	102.3	71.2	248.4	534.6	75.5	125.2	167.9	111.2	104.2	157.6	134.4
			200	*102.4*	*127.9*	*89.0*	*323.2*	*668.6*	*94.2*	*158.1*	*212.0*	*140.6*	*138.7*	*209.8*	*179.2*
			240	118.3	147.8	102.8	390.2	773.0	108.5	183.6	246.2	163.3	164.4	248.8	212.6
		10	140	84.7	105.7	73.6	257.8	552.5	77.8	129.2	173.3	114.8	108.6	164.2	140.1
			200	107.6	134.4	93.5	344.2	703.0	99.1	166.8	223.7	148.3	147.5	223.3	190.7
			240	121.9	152.3	106.0	406.9	797.0	112.0	189.6	254.3	168.7	170.4	258.0	220.4
	μ^+	3	140	80.3	100.3	69.8	243.1	524.0	73.9	122.5	164.3	108.8	101.3	153.1	130.6
			200	97.7	122.0	84.9	305.0	637.9	91.5	153.4	205.7	136.4	133.9	202.5	172.9
			240	113.7	142.1	98.9	370.1	743.0	104.4	176.2	236.3	156.7	157.0	237.6	203.0
		6	140	81.9	102.3	71.2	248.4	534.6	75.5	125.2	167.9	111.2	104.2	157.6	134.4
			200	*102.4*	*127.9*	*89.0*	*323.2*	*668.6*	*94.2*	*158.1*	*212.0*	*140.6*	*138.7*	*209.8*	*179.2*
			240	118.3	147.8	102.8	390.2	772.7	108.6	183.6	246.2	163.3	164.4	248.8	212.6
		10	140	84.7	105.7	73.6	257.8	552.5	77.8	129.2	173.3	114.8	108.6	164.2	140.1
			200	107.6	134.4	93.5	344.2	702.8	99.1	166.8	223.7	148.3	147.5	223.3	190.7
			240	121.9	152.3	106.0	406.9	797.0	112.0	189.6	254.3	168.7	170.4	258.0	220.4
Genetic algorithm	μ^-	6	140	81.9	102.3	71.2	248.4	535.0	75.5	129.2	199.9	105.0	77.8	149.6	117.6
			200	81.9	102.3	71.2	248.4	535.0	75.5	197.3	264.2	159.7	126.4	222.8	185.1
			240	118.3	147.8	102.8	390.2	773.0	108.5	213.9	313.1	198.4	152.7	264.2	224.5
		10	140	84.7	105.7	73.6	257.8	553.0	77.8	111.8	199.6	126.8	80.8	130.1	101.3
			200	107.6	134.4	93.5	344.2	702.8	99.1	168.0	265.4	124.5	109.5	211.7	180.5
	μ^+	6	200	102.4	127.9	89.0	323.2	668.6	94.2	197.3	264.2	159.7	126.4	222.8	185.1
			240	118.3	147.8	102.8	390.2	772.7	108.6	213.9	313.1	198.4	152.7	264.2	224.5
		10	140	84.7	105.7	73.6	257.8	552.5	77.8	111.8	199.5	126.8	80.8	130.1	101.3
			200	107.6	134.4	93.5	344.2	702.8	99.1	168.0	265.4	124.5	109.5	211.7	180.5
			240	121.9	152.3	106.0	406.9	797.0	112.0	138.8	290.5	198.1	155.5	281.3	219.5

beam line is designed to transport. In all cases each quadrupole triplet is arranged to focus–defocus–focus in the horizontal plane [42].

To make precise measurements the beam line should deliver a pure muon beam. However, a low rate of pion contamination is expected. The muon momentum selection is done in D2. The momentum distributions of muons and pions, for the nominal 6-200 beam, at D2 are shown in figure 4.6.

To minimise the pion contamination the backwards decaying muons in the pion reference frame are selected by D2 such that a low pion contamination rate is achieved. Figure 4.7 shows the momentum distribution of the beam at TOF1 when $p_{D2} = 238$ MeV/c. The occurrence of pions and positrons is very low. The muon momentum
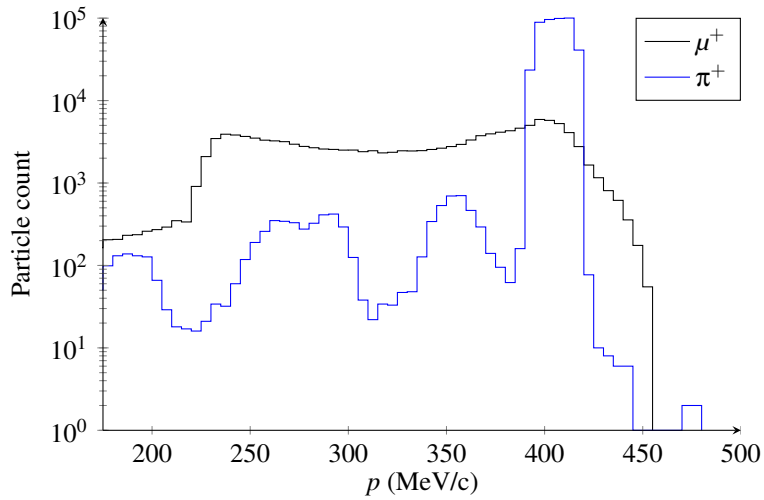
Figure 4.6: Momentum distribution of the positive muons and pions . The pion peak is at $p_{D1} \approx 410$ MeV/c which is the pion momentum selected at D1 for a 6-200 beam.
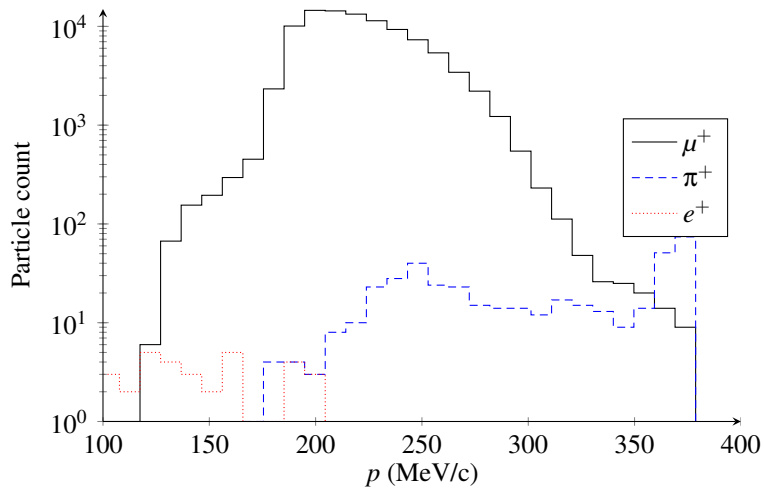

Figure 4.7: Momentum distributions of the positive muons, pions and positrons for the 6-200 beam at TOF1. Positron and pion counts are very low. $p_{D1} = 408$ MeV/C and $p_{D2} = 238$ MeV/c

distribution is skewed.

4.2 Symmetrical momentum distribution

The MICE cooling channel is based on Feasibility study 2 (ST2)[5]. The muon momentum distribution of the beam used in ST2 is symmetrical, with a mean momentum of $\bar{p} = 207$ MeV/c and momentum standard deviation of $s_p = 28$ MeV/c, as shown in figure 4.8.
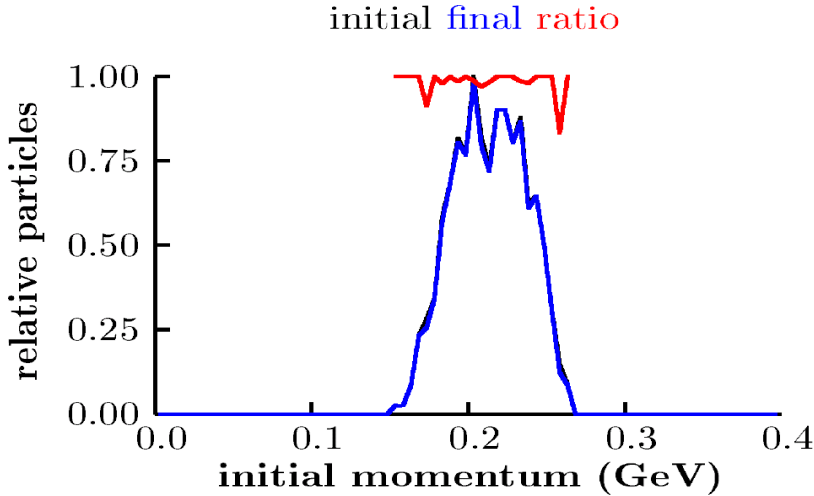

Figure 4.8: Momentum distribution of the ST2 muon beam [5].

As seen in figure 4.7 the muon momentum distribution of the nominal 6 mm - 200 MeV/c beam is skewed. The skewness

$$s = \frac{\frac{1}{n}\sum_{i=1}^{n}(x_i - \bar{x})^3}{\left(\frac{1}{n}\sum_{i=1}^{n}(x_i - \bar{x})^2\right)^{\frac{3}{2}}}, \tag{4.2}$$

is used to indicate how symmetrical the momentum distribution is. A perfectly symmetric distribution will have $s = 0$. The distribution is negative skew if the left tail is more pronounced than the right, and positive skew if the opposite [43].

To provide a beam which better resembles the symmetrical ST2 beam to MICE, a so-called D1-scan will be performed to change the muon momentum distribution.

4.2.1   Simulation results of a D1-scan

The simulation tool G4Beamline is used [11]. A D1-scan is performed by holding the magnet strengths of D2 and the two quadrupole triplets Q4-Q6 and Q7-Q9 constant, while varying the strengths of the capture quadrupoles Q1-Q3, D1 and the decay solenoid proportionally to the reference pion momentum p_{D1}.

The standard 6 mm - 200 MeV/c beam is used. The conversion from magnet currents (table 4.3) to magnetic fields are done by interpolating values from a magnet data sheet from the MICE documentation [44]. The magnetic fields are used as input to G4BL and listed in table 4.4. D2 is set to select muons with momentum $p = 238$

Table 4.4: D1-scan input parameters to G4BL. The D2 selection muon momentum is $p_{D2} = 238$ MeV/c. The quadrupole triplet is set to focus-defocus-focus in the horizontal plane.

Polarity	p_{D1} (MeV/c)	Q1 (T/m)	Q2 (T/m)	Q3 (T/m)	D1 (T)	DS (T)
	250	0.649	0.810	0.563	0.791	2.332
	275	0.715	0.892	0.621	0.872	2.571
	300	0.781	0.975	0.678	0.952	2.81
μ^+	325	0.846	1.057	0.736	1.033	3.048
	350	0.912	1.140	0.793	1.114	3.286
	375	0.978	1.222	0.850	1.194	3.523
	408	1.066	1.332	0.927	1.302	3.843
	425	1.109	1.386	0.965	1.355	3.998
	280	0.728	0.909	0.632	0.888	2.619
	310	0.807	1.008	0.701	0.985	2.905
	339	0.884	1.104	0.768	1.079	3.183
	357	0.932	1.164	0.810	1.138	3.356
μ^-	375	0.978	1.222	0.850	1.194	3.523
	392	1.020	1.278	0.889	1.249	3.686
	408	1.066	1.332	0.927	1.302	3.843
	425	1.109	1.385	0.964	1.354	3.995
	440	1.149	1.436	0.999	1.403	4.141

MeV/c.

D1-scan simulations have been performed for beams of both signs. The momentum distributions after the decay solenoid are shown in figures 4.9 and 4.10. The selection momentum at D1 is indicated in the figures. The pion peaks are located at the selection
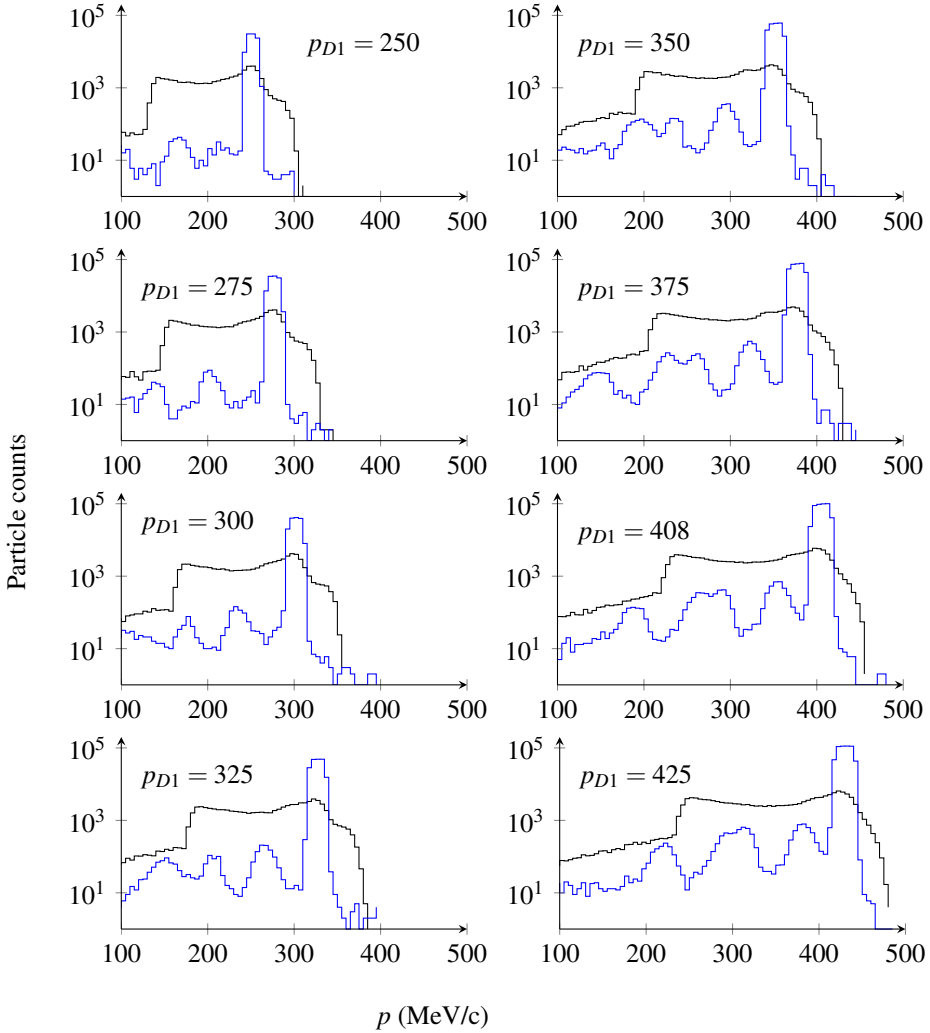
Figure 4.9: Momentum distributions of the positive muons and pions (μ^+ and π^+) after the decay solenoid when varying the selection momentum p_{D1} in dipole 1 while $p_{D}2 = 238$ MeV/c is fixed. The y-scale is logarithmic.

momentum. The skewness is observed to increase when the ratio between the pion momentum at D1 and muon momentum at D2 p_{D1}/p_{D2} increase and at some point become 0, such that the beam becomes symmetrical.

Then in figures 4.11 and 4.12 the momentum distributions at TOF1 are shown. The selection momentum p_{D1} is indicated in the figures. The skewness is measured at TOF1, before it enters MICE. The skewness is negative skewed for low pion selection momentum p_{D1}, positive skewed for high pion selection momentum p_{D1} and more symmetrical in between. The momentum distribution width s_p and the particle count also change when doing the D1-scan.

Selected skewness values vs. p_{D1} for both signs beams are shown in table 4.5. According to the simulations one would expect the beams to be close to symmetrical

Table 4.5: Skewness for the positive and the negative beam calculated from the simulations. The positive/negative beam is on the left/right side of the slash.

p_{D1} +/-(MeV/c)	300/310	325/339	375/375	408/408
s	-0.82/-0.40	-0.13/0.17	0.51/0.45	0.65/0.68

when $p_{D1} \approx 325$ MeV/c.

4.2.2   Simulations and MICE data

MICE data was retrieved for the runs listed in table 4.6. The statistics from the MICE

Table 4.6: The MICE data run numbers for the D1-scan.

p_{D1} (MeV/c)	339	357	375	392	408	425
Run	4149	4148	4147	4145	4144	4150

data is low and it only exists for the negative beam at the moment, these results are therefore only preliminary. Higher statistics runs are expected to be taken and analysed in the near future. However, the statistics should be high enough to give estimates for the beam mean, skewness and standard deviation with reasonable error calculations.

Cuts are applied to eliminate the longest tails of the momentum distributions. A cut on the particle count was used, eliminating 2.5 % of the particles on each tail. Simu-
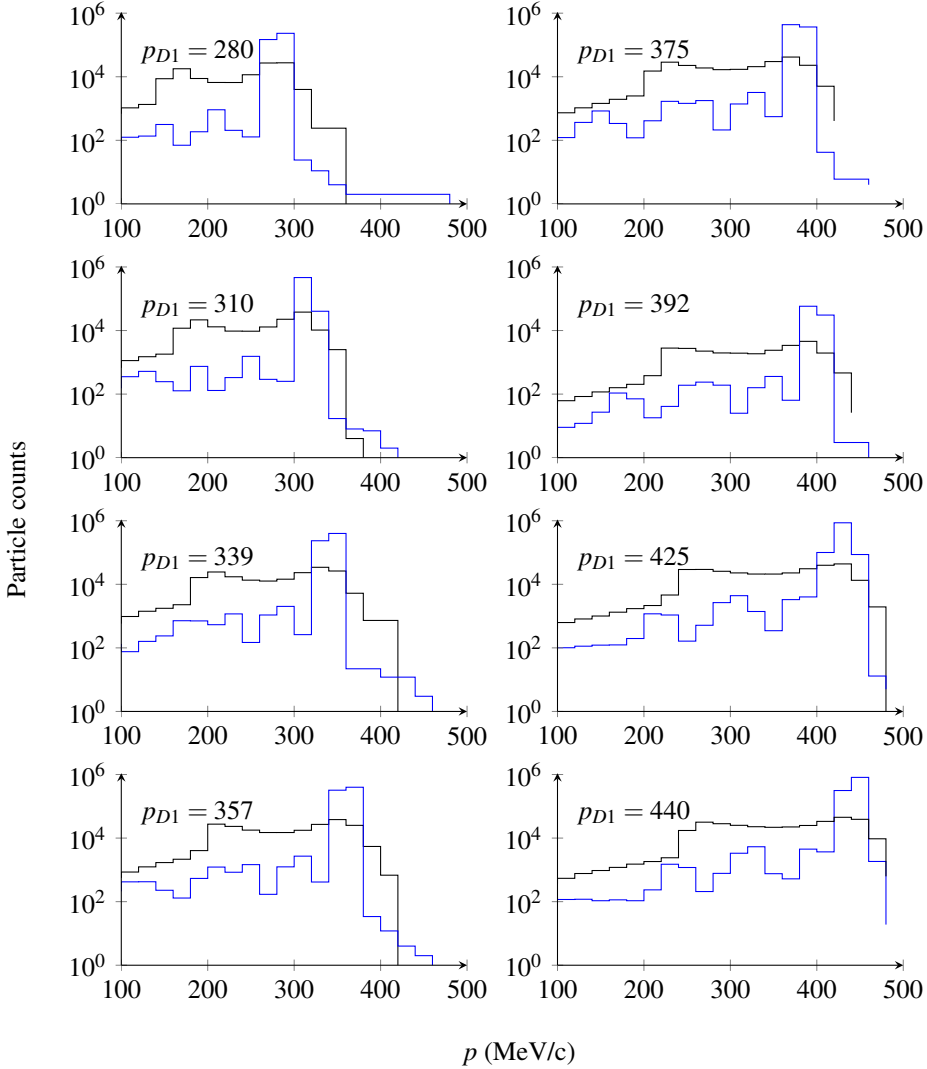
Figure 4.10: Momentum distributions of the negative muons and pions (μ^- and π^-) after the decay solenoid when varying the selection momentum p_{D1} in dipole 1 while $p_{D2} = 238$ MeV/c is fixed. The y-scale is logarithmic.
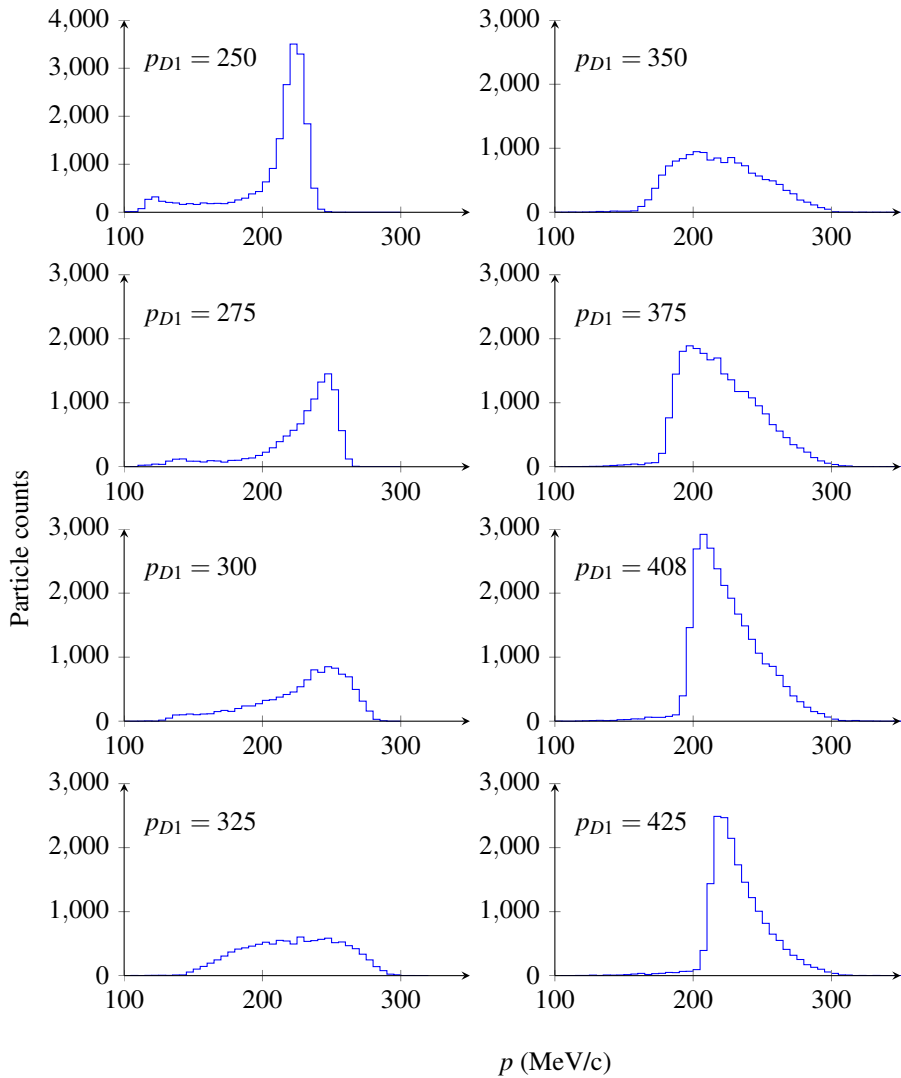
Figure 4.11: Momentum distributions of the positive muons (μ^+) at TOF1 when varying the selection momentum p_{D1} in dipole 1 while $p_{D2} = 238$ MeV/c is fixed.
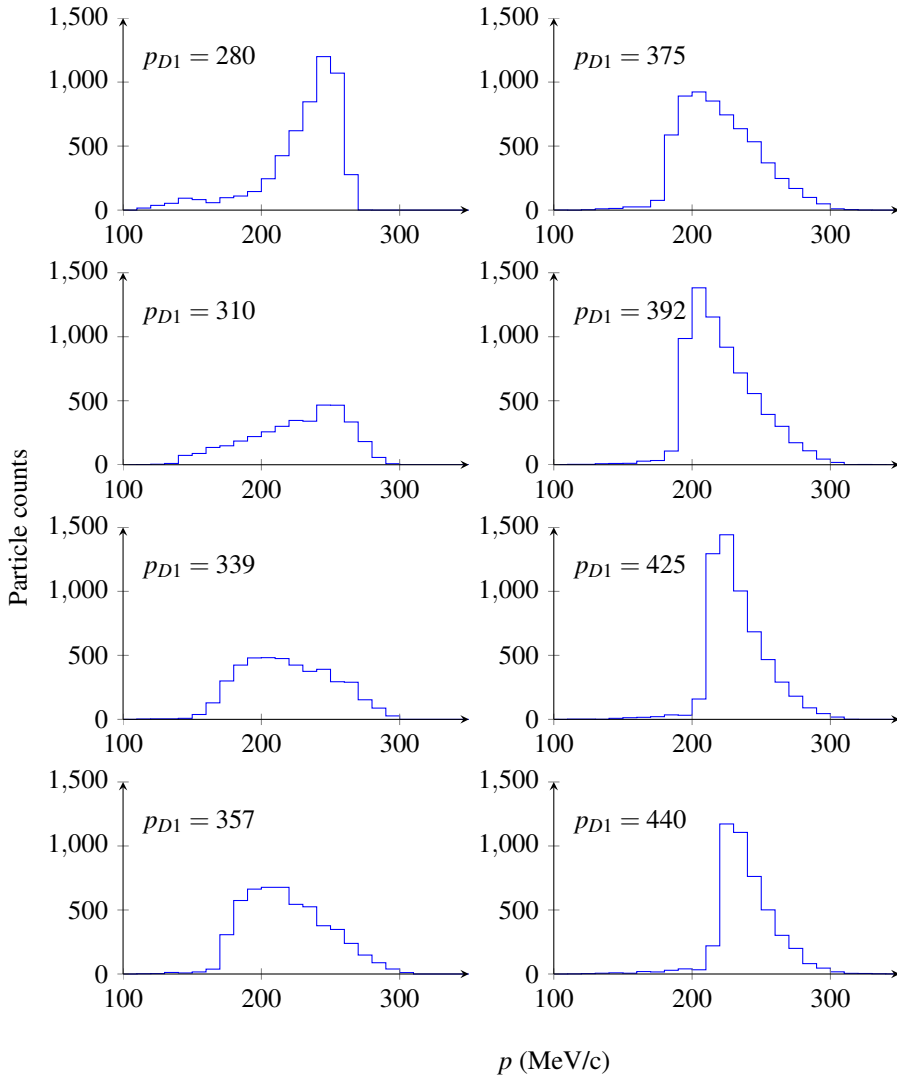
Figure 4.12: Momentum distributions of the negative muons (μ^-) at TOF1 when varying the selection momentum p_{D1} in dipole 1 while $p_{D2} = 238$ MeV/c is fixed.

lations have been normalised to the MICE data by integration. The cuts are especially important for the higher momenta, which have longer tails.

When analysing the MICE data the momentum distributions are approximated from the time-of-flight between TOF0 and TOF1, removing all particles in the TOF electron peak and assuming the rest of the particles to be muons. The muon momentum distribution from MICE data and G4BL at TOF1 are compared in figure 4.13 and the agreement is fairly good.

The mean momentum at detector TOF1 lies in the interval $p \in [215, 235]$ MeV/c when varing p_{D1}, as shown in figure 4.14.

The standard deviation of the momentum distribution is shown in figure 4.15 and the maximum distribution width is found at 325 MeV/c for the simulations, and falls when going to higher momenta. For the MICE data the maximum is found at the lowest p_{D1}.

When calculating the skewness of the distribution the cuts are especially important. It is sensitive to outliers and therefore they are eliminated from the distribution. The most symmetric distribution is found when $p_{D1} = 330$ MeV/c and for the MICE data the lowest data point at $p_{D1} = 339$ MeV/c has the lowest skewness as shown in figure 4.16. MICE data for lower D1 selection momentum is needed to confirm the simulation results.

If the MICE data can be extrapolated to agree with the simulations, then a symmetrical momentum distribution can be found when D1 is set to select pions with $p_{D1} \approx 330$ MeV/c. The standard deviation of that beam is $s_p \approx 30$ MeV/c and the mean momentum is $\bar{p} \approx 225$ MeV/c. The mean momentum will decrease further between TOF1 and the cooling section, further downstream, where some detector material and a diffuser will be placed. The ST2 beam has a standard deviation $s_p \approx 28$ MeV/c and mean momentum $\bar{p} \approx 207$ MeV/c, the symmetrical momentum muon beam better resembles the ST2 beam than the nominal 6-200 beam.

4.2.3 D1 scan pion contamination

Some pion contamination is expected in the beam, but to minimise the pion contamination level the selection momentum in dipole D2 $p_{D2} < p_{D1}$ is set to select the muons that decay backwards in the pion reference frame. The MICE beam line must deliver a beam with a pion contamination lower than a few percent [36]. According to the
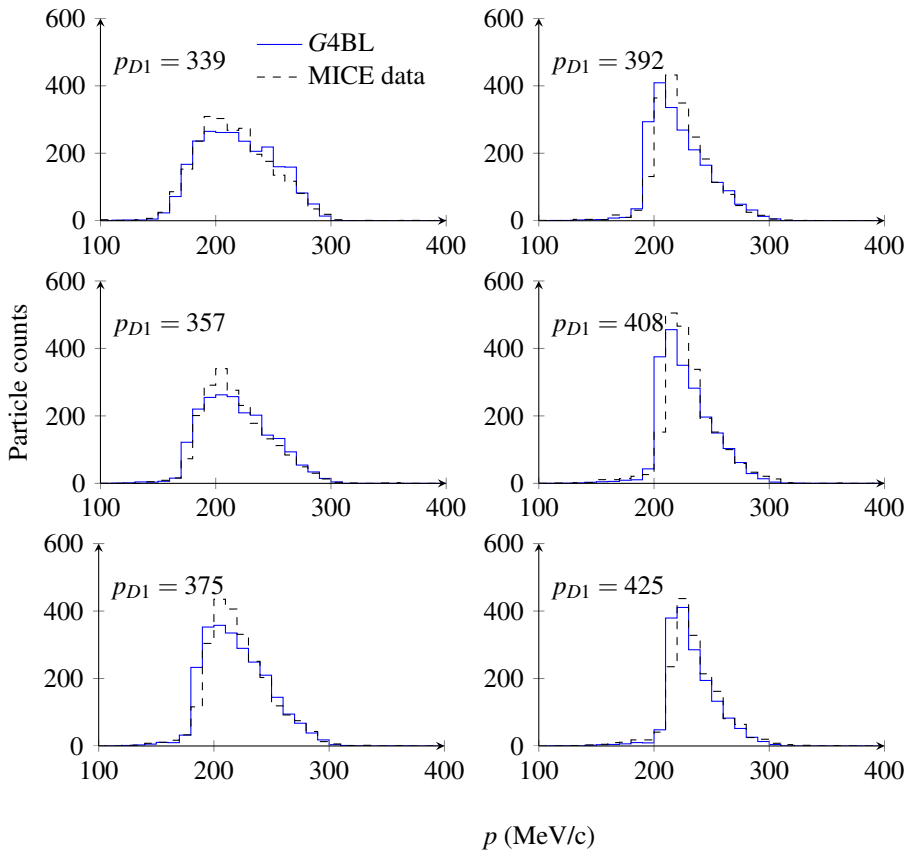
Figure 4.13: Momentum ditribution vs p_{D1} at TOF1. The distribution get more symmetrical when p_{D1} is lowered, the variance increase and the mean momentum is lowered.
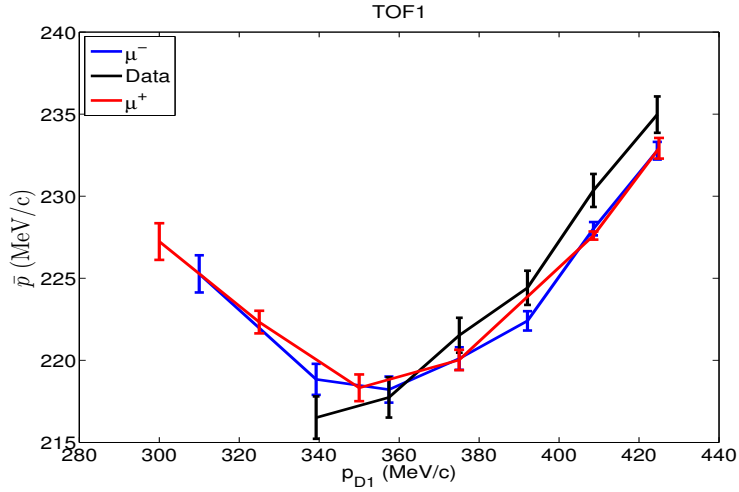
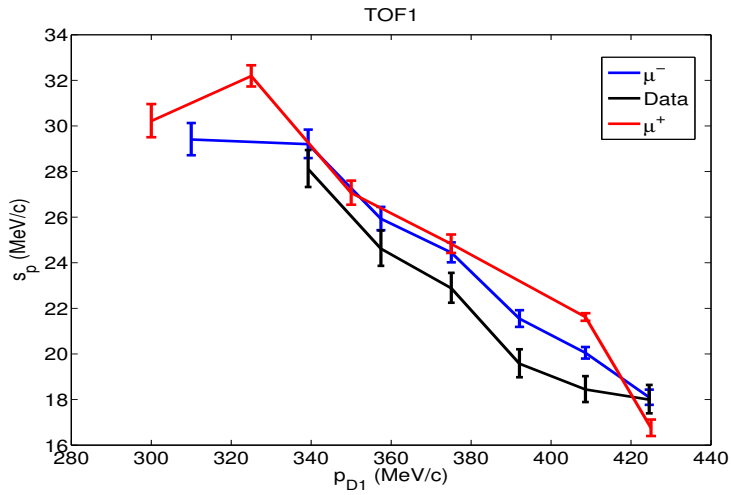Figure 4.14: The mean momentum at TOF1 as a function of p_{D1}. The ST2 muon beam has $\bar{p} = 207$ MeV/c.

Figure 4.15: The momentum standard deviation vs p_{D1} at TOF1. The ST2 beam has $s_p = 28$ MeV/c. The error bars correspond to 95 % confidence intervals.
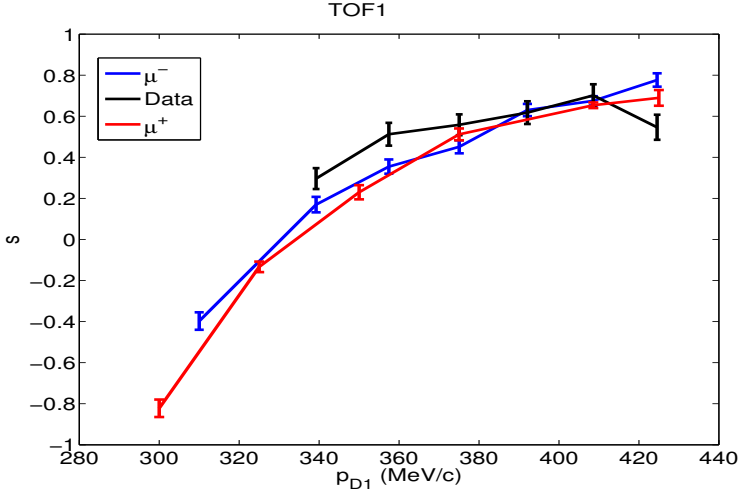
Figure 4.16: The momentum skewness vs. p_{D1}. The beam is symmetrical when $s = 0$, found when $p_{D1} \approx 330$ MeV/c. The error bars are statistical.

D1-scan simulations the pion contamination is low in the interval $p_{D1} \in [300, 425]$, shown in figure 4.17. The worst case is approximately 2.7 %, if one selects the most pessimistic value of the error bar from $p_{D1} = 300$.

Selecting pion momentum smaller than $p_{D1} < 300$ MeV/c increases the pion contamination to unacceptably high values, the pion selection momentum p_{D1} and the muon selection momentum $p_{D2} = 238$ are too close, resulting in transportation of both species to TOF1. For the negative beam with $p_D1 = 280$ MeV/c the pion contamination is 29% and for the positive beam with $p_{D1} = 275$ MeV/C the pion contamination is 39 %.

The pions can readily be distinguished from the muons when the momentum is known, as shown in figure 4.18, MICE Step IV will deliver measurements of energy[45].

4.3 The MICE muon beam

The MICE beam line delivers a muon beam to MICE when $p_{D2} \sim \frac{1}{2} p_{D1}$ as opposed to a pion beam when $p_{D2} \sim p_{D1}$. The focus will be on the nominal $\varepsilon_N = 6$ mm rad
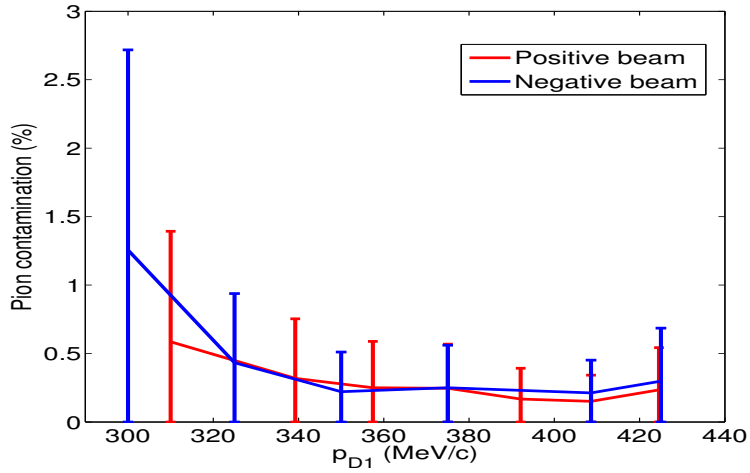
Figure 4.17: Pion contamination vs. p_{D1} at TOF1, error bars are statistical.
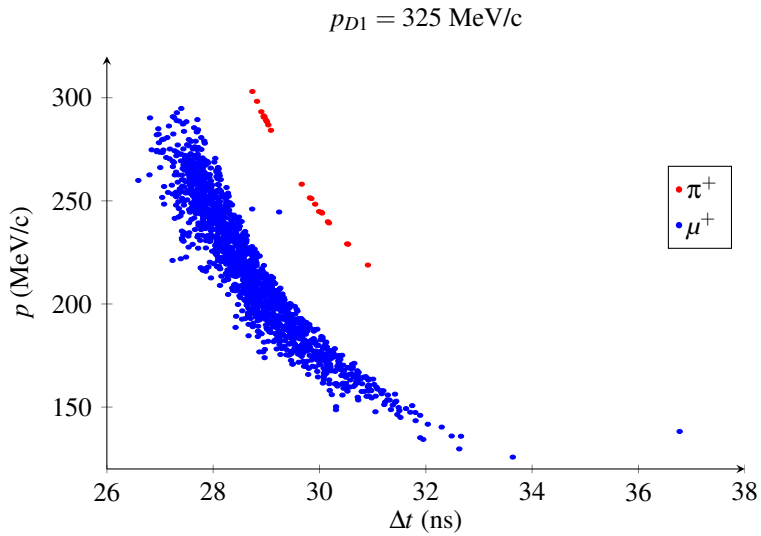
$$p_{D1} = 325 \text{ MeV/c}$$

Figure 4.18: Time-of-flight versus momentum at TOF1.

muon beams. The beam momentum distribution for the nominal 6-140, 6-200 and 6-240 beams are shown in figure 4.19. The beams contain pions in the higher momentum
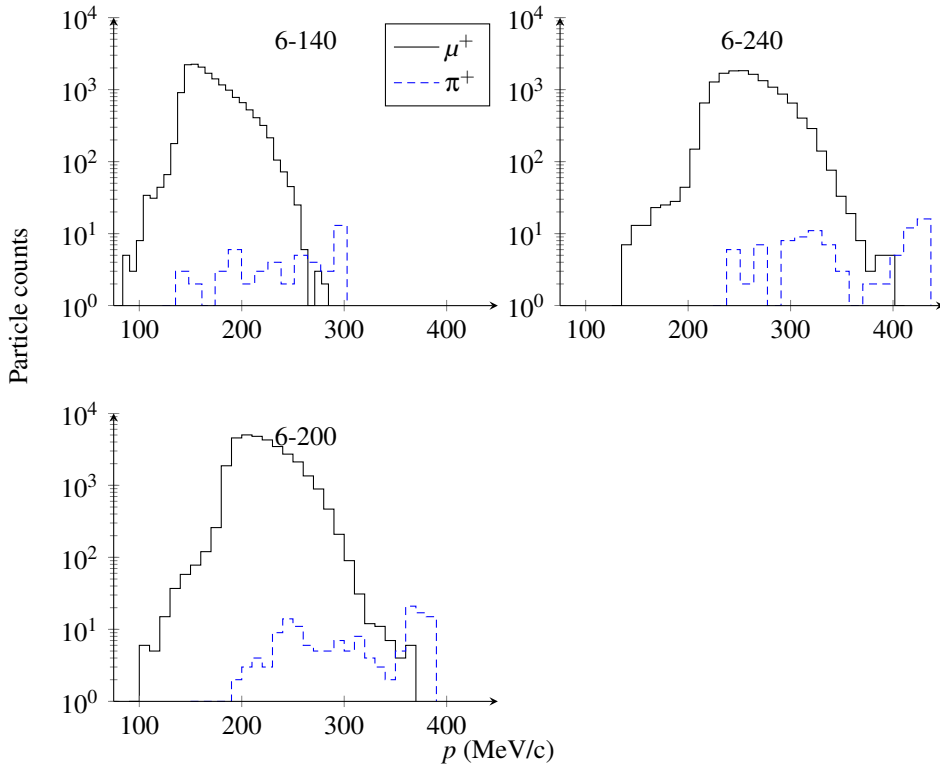

Figure 4.19: Time-of-flight versus momentum at TOF1 for the positive beams.

region, the *y*-axis follows a logarithmic scale to make the small pion fraction visible.

The evolution of the mean muon momentum along the beam line, at TOF0, TOF1 and TOF2, is listed in table 4.7 where p_μ is the nominal mean muon beam momentum and p_{D2} is the muon selection momentum. The values in parenthesis are the values obtained when inserting a proton absorber in the beam line. For the $p_\mu = 140$, 200 and 240 MeV/c beams the corresponding absorber thickness' are t=44, 83 and 147 mm.

Table 4.7: The 9 nominal beam settings with the corresponding mean muon momentum along the MICE beam line. The higher mean momentum for higher emmittance settings compensate for the increasing diffuser thickness.

p_μ (MeV/c)	ε_N (π mm·rad)	p_{D2} (MeV/c)	p_{TOF0} (MeV/c)	p_{TOF1} (MeV/c)	p_{TOF2} (MeV/c)
140	3	185	178 (171)	153 (148)	138 (132)
140	6	189	183 (174)	157 (149)	142 (134)
140	10	195	189 (179)	165 (160)	150 (149)
200	3	231	226 (214)	203 (190)	190 (184)
200	6	238	233 (220)	211 (204)	198 (190)
200	10	251	247 (240)	224 (219)	212 (202)
240	3	265	261 (256)	239 (232)	227 (223)
240	6	276	272 (268)	250 (247)	238 (234)
240	10	285	281 (276)	259 (253)	248 (242)

4.3.1   Pion contamination

The MICE beam line must deliver a beam with a pion contamination lower than a few percent, as already mentioned. The investigation of pion contamination and the results are derived from Monte Carlo simulations.

The evolution of pion contamination along the MICE beam line, from TOF0 to TOF2 is shown in figure 4.20 and listed in table 4.8 for both signs $\varepsilon_n = 6$ mm rad muon beams. The pion contamination decreases along the beamline, the points are at TOF0, TOF1 and TOF2. The positive beam has higher pion contamination than the negative beam. The error bars are statistical.

In table 4.8 the particle count and pion contamination from monte carlo simulations, for the six $\varepsilon_N = 6$ mm rad beams, are compared; the beam contains three particle types. Time-of-flight between TOF0 and TOF1 cuts are applied, only particles within the interval $\Delta t_{TOF1-TOF0} \in [26.2, 36]$ for the 140 beams and $\Delta t_{TOF1-TOF0} \in [26.2, 33]$ for the 200 and 240 beams are accepted. The pion contamination is higher when increasing the muon beam momentum and the positive beam has a higher pion contamination. **All $\varepsilon_N = 6$ mm nominal beams have acceptable pion contamination levels lower than**
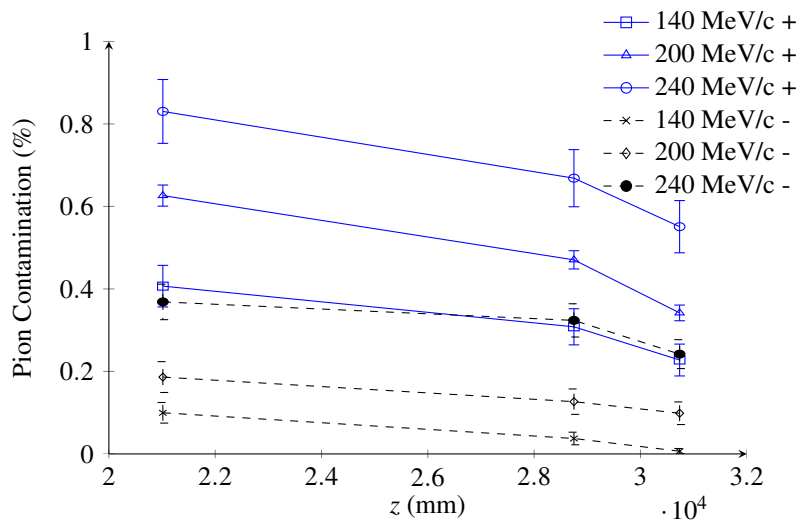
Figure 4.20: Pion contamination at TOF0, TOF1 and TOF2 for the $\varepsilon_N = 6$ mm rad beams.

Table 4.8: Pion contamination and particle counts for the nominal $\varepsilon_N = 6$ beams.

p_μ (MeV/c)	No. e	No. μ	No. π	π contamination (%)
140 (-ve)	14	16025	6	0.04 ± 0.02
200 (-ve)	10	13392	17	0.13 ± 0.03
240 (-ve)	15	20000	65	0.32 ± 0.04
140 (+ve)	4	16171	50	0.31 ± 0.04
200 (+ve)	59	97041	459	0.47 ± 0.02
240 (+ve)	15	14102	95	0.67 ± 0.07

1%.

4.3.2   MICE data compared with simulations

When analysing the MICE data the momentum distributions are approximated from the time-of-flight between TOF0 and TOF1, removing all particles in the TOF electron peak and assuming the rest of the particles to be muons.

The time-of-flight distributions are shown in figures 4.21 and 4.22 for the 6-140 and 6-200 beams, the MICE data for the 6-240 beam was not available for analysis at the time of writing. The MICE beam from the simulations can be split into three
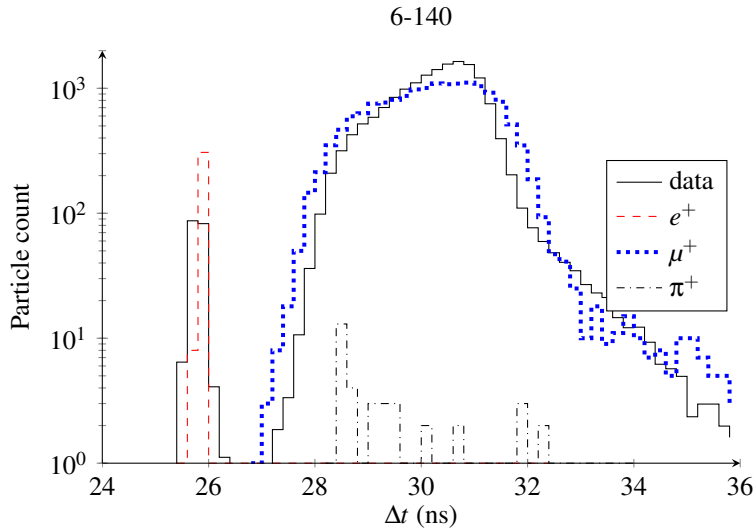

Figure 4.21: Time-of-flight distribution between detectors TOF0 and TOF1 for the positive 6-140 beam.

particles e^+, μ^+ and π^+ while for the MICE data such distinctions were not possible. Simulations are normalised to the MICE data by integration.

The e^+ peaks are located at $\Delta t \sim 25.8$ ns which can easily be distinguished from the pions and muons, the applied time-of-flight cuts removed this e^+ peak from the pion contamination calculations. The pions, however, are found under the muon peak which makes them difficult to distinguish from muons without knowing the particle
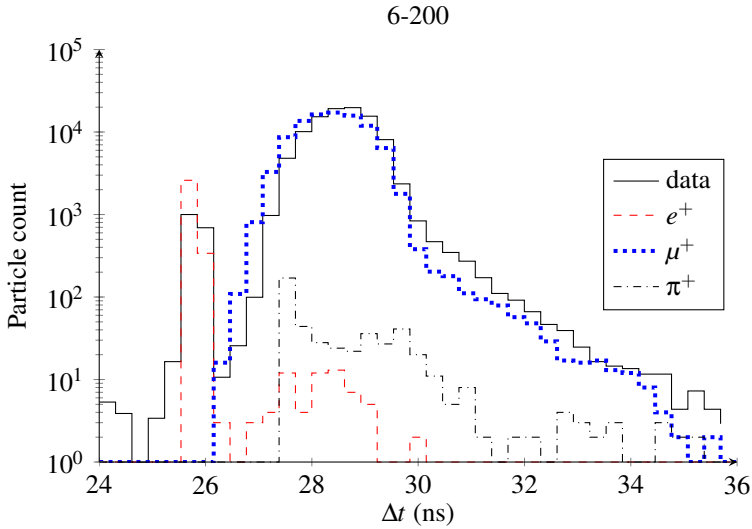
momentum.

Figure 4.22: Time-of-flight distribution between detectors TOF0 and TOF1 for the positive 6-200 beam.

4.4 Summary

MICE is expected to deliver the proof-of-principle for ionisation cooling, with that failing some novel cooling technique has to be invented for both the NF and μC.

A D1-scan of the nominal 6-200 beam for both positive and negative beams was performed. If the MICE data can be extrapolated to agree with the simulations, then a symmetrical momentum distribution can be found when D1 is set to select pions with $p_{D1} \approx 330$ MeV/c. The standard deviation of that beam is $s_p \approx 30$ MeV/c and the mean momentum is $\bar{p} \approx 225$ MeV/c. The mean momentum will decrease further between TOF1 and the cooling section, further downstream, where some detector material and a diffuser will be placed. The ST2 beam has a standard deviation $s_p \approx 28$ MeV/c and mean momentum $\bar{p} \approx 207$ MeV/c, the symmetrical momentum muon beam better resembles the ST2 beam than the nominal 6-200 beam while keeping the pion contamination low.

The MICE muon beams with emittances of $\varepsilon_N = 6$ mm has been studied. Monte Carlo simulations showed that the MICE muon beams contain pions, but pion contamination for all $\varepsilon_N = 6$ mm nominal beams were acceptable and below 1%. Comparing the distributions of time-of-flight from simulations with the MICE data showed good agreement.

Chapter 5

Summary and Outlook

The Neutrino Factory uses primary protons bombarding a free-flowing mercury-jet target for the production of the secondary pions. The pions then decay to muons which are accelerated and stored. The neutrinos are then obtained from decay of the circulating muons in the storage ring.

The Neutrino Factory is widely regarded as the ultimate neutrino facility, providing better parameter sensitivities than current alternatives. Ionisation cooling is an integer part of the NF, constituting the main outstanding technical challenge.

A detailed assessment of the optimisation of particle production in the Neutrino Factory by Monte Carlo simulations is made in chapter 2. The focus was on the production of secondary particles from the interaction between primary protons and the mercury target. Optimising the production of secondary particles is important to increase the muon density in the storage ring which ultimately decides the neutrino beam intensity.

The optimisation of the beam's impact position and impact angles on the short mercury target showed that the intercept angle between the beam and the target θ_{BT} should be kept between 10 and 15 mrad and the beam should enter the target from the top for optimal performance. In addition, when varying the intercept angle between the beam and the target θ_{BT} the performance varied by up 6%, while when varying the azimuth angle ϕ the performance varied by up to 5%, as shown in subsection 2.4.1. Shape fluctuations of the free-flowing mercury jet target as seen in the MERIT experiment was investigated and the effect was shown to reduce the performance of 3% or less, as shown in subsection 2.4.2.

In subsection 2.4.3 a full length mercury jet target was introduced and replaced the short target. In addition an improved measurement of the proton beam trajectory in the

target, the proton path length λ_{IR} was introduced. The optimisation with respect to the azimuth angle ϕ showed that the proton beam should enter the target from the top for optimal performance, when the intercept angle is held fixed. In addition it was shown that the effect of shape fluctuations on the long target in a high magnetic field reduces the performance by a maximum of only 1.3 %.

In subsection 2.4.5 centring the proton beam-target interaction region in the beam pipe resulted in a centred secondary beam which increased the flux of secondary particles after the target by 10.8 %. The proton path length in the jet was increased which gave an increased muon count of 6.8% after the target, giving an accumulated increase of 17.3 %.

The optimised proton beam parameters, the accumulated effect of all target optimisation studies, increased the performance by approximately 6 % when applying acceptance cuts as shown in figure 2.33. Changes and improvements at this level are very significant and important when discussing cost and performance for a future neutrino facility.

Optimisation of the magnetic field and magnet shielding layout in the capture, the tapering and the drift sections for an alternative (to the baseline) set-up is performed in chapter 3.

In subsection 3.1 the optimisation without any shielding showed that a shorter magnetic field tapering is a good alternative to the longer adiabatic tapering. The alternative set-up with a short magnetic field allows for lower currents in the solenoid magnets and may allow for a larger solenoid radius thereby exposing it to less radiation.

A short and rapidly decreasing magnetic field tapering allows for solenoid magnets with lower magnetic field strength and smaller aperture. To conserve the magnetic flux through the capture, tapering and drift sections, the shielding thickness was decreased according to the short magnetic field tapering, by increasing the shielding inner radius and shortening the shielding cone length. The magnetic field tapering was optimised for the new alternative shielding.

The optimised alternative set-up gives a higher yield compared to the baseline set-up. Two Monte Carlo simulation tools were used, G4beamline and FLUKA. As shown in figure 3.30, the alternative set-up performs 10% better than the baseline set-up and 6% better than the baseline set-up with the alternative shielding according to the G4beamline simulations. The results from FLUKA shows that the alternative set-up performs 14% better than the baseline set-up. The baseline with the alternative shielding performs 10% better than the alternative set-up. However, reducing the shielding thickness for the baseline set-up increases the energy deposition in the magnets. In addition the length of the drift section could be shortened by approximately 20 m, delivering a denser muon beam, without performance loss at the buncher as shown in figure 3.24. The performance of the buncher when receiving a denser muon beam

needs further study.

The optimised alternative set-up has a 10% higher yield than the baseline. Combining the optimisations of chapter 2 (optimised beam parameters for particle production) and chapter 3 (optimised capture and tapering sections) the optimal set-up increases the muon yield by another 6 %, up to a total increase of approximately 16 % compared to the baseline set-up as shown in figure 3.32.

These studies show what is possible to achieve by optimisation. Incremental changes to the baseline were implemented and resulted in significant performance improvements.

Future work should include a study of the energy deposition in the solenoid magnets for the new shielding layout. The pre-accelerator, including the buncher, the phaserotator and the cooler, should be optimised to the new alternative set-up. In addition the effect of shortening the drift section should be studied, specifically the implications of delivering a denser longitudinal muon beam to the pre-accelerator.

A detailed assessment of MICE and the MICE beam line was made in chapter 4. The magnetic field in the first dipole of the MICE beam line was varied using the nominal MICE beam to find a muon beam with a symmetrical muon momentum distribution which better resembled the baseline beam. If the MICE data can be extrapolated to agree with the simulations, then a symmetrical momentum distribution can be found when dipole 1 is set to select pions with momentum $p_{D1} \approx 325$ MeV/c, as shown in figure 4.16. The standard deviation of that beam is $s_p \approx 30$ MeV/c and the mean momentum is $\bar{p} \approx 225$ MeV/c, as shown in figures 4.15 and 4.14. The baseline beam has a standard deviation $s_p \approx 28$ MeV/c and mean momentum $\bar{p} \approx 207$ MeV/c, the symmetrical momentum muon beam better resembles the baseline beam than the nominal MICE beam while keeping the pion contamination low.

The MICE muon beams with emmittances of $\varepsilon_N = 6$ mm has been studied. Monte Carlo simulations showed that the MICE muon beams contain pions, but pion contamination for all $\varepsilon_N = 6$ mm nominal beams were acceptable and below 1% as shown in table 4.8. Comparing the distributions of time-of-flight from simulations with the MICE data showed good agreement.

Bibliography

[1] S. Bilenky. *Introduction to the Physics of Massive and Mixed Neutrinos*. Lecture Notes in Physics. Springer, 2010. ISBN 9783642140426. URL `http://books.google.fr/books?id=wa89ypyicA0C`.

[2] J. Beringer and others (Particle Data Group). 2012 review of particle physics. *Phys. Rev. D86*, 010001 (2012).

[3] S. Choubey et al. International design study for the neutrino factory, interim design report. Technical Report BNL-96453-2011, CERN-ATS-2011-216, FERMILAB-PUB-11-581-APC, RAL-TR-2011-018, 2011.

[4] R. Fernow et al. Front-end design for neutrino factory study 2a. Technical Report MUC-NOTE-COOL_THEORY-296., 2004.

[5] S. Ozaki, R. Palmer, M. Zisman, J. Gallardo, et al. Feasibility study-II of a muon-based neutrino source. Technical Report BNL-52623, 2001.

[6] IDS-NF collaboration. Figure of NF complex. 2012. URL `https://www.ids-nf.org/wiki/FrontPage/Accelerator/Documentation/attachment:IDS-NuFact-121025`.

[7] The IDS-NF collaboration. Reference design report v0.1, the international design study for the neutrino factory draft. Technical report, 2013. URL `https://www.ids-nf.org/wiki/FrontPage/Documentation/RDR?action=AttachFile&do=get&target=IDS-NF-RDR-v0.1.pdf`.

[8] V. B. Graves et al. Design of the mercury handling system for a muon collider/neutrino factory target. 2013. URL `http://oraweb.cern.ch/pls/ipac2013/TOC.htm`.

[9] K. T. MacDonald et al. The MERIT high-power target experiment at the CERN PS. *FERMILAB-CONF-10-212-APC*, 2010.

[10] A. Ferrari, P.R. Sala, A. Fassò, and J. Ranft. Fluka a multi-particle transport code. 2012. URL `http://www.fluka.org/`.

[11] T. Roberts. G4beamline user's guide. 2012. URL `http://g4beamline.muonsinc.com`.

[12] J. Allison et al. Geant4 developments and applications. *Nuclear Science, IEEE Transactions on*, 53(1):270–278, 2006. ISSN 0018-9499. doi: 10.1109/TNS.2006.869826.

[13] A. Blondel. The mice experiment. IPAC2013. URL `http://oraweb.cern.ch/pls/ipac2013/TOC.htm,document=TUPFI046.pdf`.

[14] IDS-NF collaboration. IDS-NF-RDR-v1.0. 2013. URL `https://www.ids-nf.org/wiki/FrontPage/Documentation/RDR`.

[15] Pilar Coloma, Andrea Donini, Enrique Fernandez-Martinez, and Pilar Hernandez. Precision on leptonic mixing parameters at future neutrino oscillation experiments. *JHEP*, 1206:073, 2012. doi: 10.1007/JHEP06(2012)073.

[16] MICE collaboration. Mice first rf cavity. . URL `http://mice-overview.web.cern.ch/mice-overview/html/Layout.htm`.

[17] O. M. Hansen et al. A simplified magnetic field tapering and target optimisation for the neutrino factory capture system. *Conf. Proc.*, page TUPFI018., 2013. URL `http://accelconf.web.cern.ch/accelconf/IPAC2013/papers/tupfi018.pdf`.

[18] H. J. Park. *Experimental Investigation of Magnetohydrodynamic Flow for An Intense Proton Target*. PhD thesis, 2009. Dissertation presentation.

[19] T. R. Edgecock et al. Overview of solid target studies for a neutrino factory. 2010. URL `http://accelconf.web.cern.ch/accelconf/IPAC10/papers/thpec089.pdf`.

[20] O. Caretta, T. W. Davies, C. J. Densham, and R. M. Woods. Preliminary experiments on a fluidised powder target. 2008.

[21] N. Charitonidis et al. A feasibility experiment of a w-powder target in the hiradmat facility at cern. 2013. URL `http://accelconf.web.cern.ch/accelconf/IPAC2013/papers/thpfi053.pdf`.

[22] R. C. Fernow and J. C. Gallardo. Front-end: Magnetic channel and rf cavity parameters. *Brookhaven National Laboratory*, 2004. URL http://www.cap.bnl.gov/mumu/study2a/rf-properties.pdf.

[23] X. Ding, J. S. Berg, D. Cline, and H. G. Kirk. Optimization of a mercury jet target for a neutrino factory or a muon collider. *Phys. Rev. ST Accel. Beams*, 14:111002, Nov 2011. doi: 10.1103/PhysRevSTAB.14.111002. URL http://link.aps.org/doi/10.1103/PhysRevSTAB.14.111002.

[24] K. Wille. *The Physics of Particle Accelerators, an introduction*. Oxford University Press, 2000. ISBN 0198505493.

[25] R. C. Fernow. Physics analysis performed by ecalc9. *Neutrino Factory and Muon Collider Notes MUC-NOTE-COOL THEORY-280, Brookhaven National Laboratory*, 2003. URL http://www-mucool.fnal.gov/notes/notes.html.

[26] R. C. Fernow et al. ICOOL reference manual, version 3.30. *Brookhaven National Laboratory*, 2012. URL https://pubweb.bnl.gov/~fernow/icool/v330/ICOOLman.pdf.

[27] D. Neuffer et al. Muon capture in the front end of the ids neutrino factory. *IPAC10 Conference Proceedings*, 2010. URL accelconf.web.cern.ch/accelconf/IPAC10/papers/wepe068.pdf.

[28] Pavel Snopok. IDR front-end v1.1 discrete, 2011. URL http://hepunx.rl.ac.uk/uknf/wp1/idsfrontend/Beams_and_Lattices/FrontEnd_v1.1_IDR_discrete/G4BL-2011-05-27/.

[29] W. H. Press, S. A. Teukolsky, W. T. Vetterling, and B. P. Flannery. *Numerical Recipes, The Art of Scientific Computing*. Cambridge University Press, third edition, 2007. ISBN ISBN-10: 0521880688.

[30] E. W. Weisstein. "Standard Error". From MathWorld-A Wolfram Web Resource, . URL http://mathworld.wolfram.com/StandardError.html.

[31] O. M. Hansen and I. Efthymiopoulos. Optimizing the neutrino factory capture section. 2012. NuFact12, Williamsburg, USA 2012.

[32] M. Apollonio et al. Comparison of large-angle production of charged pions with incident protons on cylindrical long and short targets. *Phys. Rev. C*, 80:065204, Dec 2009. doi: 10.1103/PhysRevC.80.065204. URL http://link.aps.org/doi/10.1103/PhysRevC.80.065204.

[33] A. Bolshakova et al. HARP-CDP hadroproduction data: comparison with FLUKA and GEANT4 simulations. *The European Physical Journal C*, 70(3): 543–553, 2010. ISSN 1434-6044. doi: 10.1140/epjc/s10052-010-1486-0. URL http://dx.doi.org/10.1140/epjc/s10052-010-1486-0.

[34] HARP collaboration. Harp website, . URL http://harp.web.cern.ch/harp/.

[35] O. M. Hansen, A. Blondel, and I. Efthymiopoulos. Towards a Symmetric Momentum Distribution in the Muon Ionisation Cooling Experiment. *Conf. Proc.*, C130512(CERN-ACC-2013-0281):TUPFI020. 4 p, May 2013.

[36] M Bogomilov et al. Measurement of the pion contamination in the mice beam. 2013. URL http://mice.iit.edu/micenotes/public/pdf/MICE0416/MICE0416.pdf.

[37] A. Skrinsky and V. Parkhomchuk. Methods of cooling beams of charged particles. *Accelerator Science and technology 1*, pages 237–257, 2008.

[38] D Neuffer. Multi-TeV Muon Colliders. *AIP Conf. Proc.*, 156:201–208, 1987.

[39] F. Ambrosino et al. Calibration and performances of the kloe calorimeter. *Nucl. Instrum. Meth. A*, 598(1):239 – 243, 2009. ISSN 0168-9002. doi: http://dx.doi.org/10.1016/j.nima.2008.08.097.

[40] M. Bogomilov et al. The MICE Muon Beam on ISIS and the beam-line instrumentation of the Muon Ionization Cooling Experiment. *JINST*, 7:P05009, 2012. doi: 10.1088/1748-0221/7/05/P05009.

[41] M. Appolonio. Pion-muon beam line magic table. URL http://mice.iit.edu/bl/.

[42] M. A. Rayner. *The development of a novel technique for characterizing the MICE muon beam and demonstrating its suitability for a muon cooling measurement.* PhD thesis, 2011. URL http://mrayner.web.cern.ch/mrayner/docs/MICE/papers/MarkRayner_thesis.pdf.

[43] E. Weisstein. "Skewness". From MathWorld-A Wolfram Web Resource, . URL http://mathworld.wolfram.com/Skewness.html.

[44] MICE collaboration. MICE documentation, . URL http://mice.iit.edu/bl/Documentation/index_doc.html.

[45] D. Kaplan. Progress towards completion of the MICE demonstration of muon ionization cooling. 2013.

Appendix A

Conference Papers

A.1   Optimizing the neutrino factory capture section

Oral presentation at NuFact12, July 2012, Williamsburg, USA [31].

Optimizing the neutrino factory capture section

Ole Martin Hansen[*] and Ilias Efthymiopoulos[†]

[*]*University of Oslo, Oslo, Norway & CERN, Genéve, Switzerland*
[†]*CERN, Genéve, Switzerland*

Abstract. The *capture section* is studied using the simulation tools `FLUKA` and `G4beamline`. Protons hit a Hg-target producing charged secondary particles in a region with a high magnetic field. The pions and muons are focused by a tapered magnetic field produced by a series of solenoids. The goal of the study is to improve the capture efficiency, by using alternative magnetic field tapering, solenoid geometry and solenoid shielding.

Keywords: Neutrino factory, capture section, solenoid, magnetic field, taper
PACS: 41.85.Lc, 13.25.-k

INTRODUCTION

The Neutrino Factory (NF) will provide intense, high energy neutrino beams from the decay of muons [1]. The majority of the muons will be created from the decay of pions, produced by a proton beam impinging on a Hg-target. It will be important to capture a large fraction of the produced pions, then let them decay to muons and transport them through the NF *front-end* to maximize the particle flux into the accelerator. The NF front-end consists of the target and capture section, a longitudinal drift, a buncher, a rotator and finally a muon cooling section.

In the baseline design the capture section consists of a series of high magnetic field solenoids (see figure 1), making a magnetic field tapered from 20 T to 1.75 T over a distance of 12 m [2]. Charged particles from the target are captured in the 20 T magnetic field to form a beam. The beam's divergence is then gradually decreased by the tapered magnetic field, before it enters the constant 1.75 T field in the drift section. Here pions decay and the particles develop a position and energy correlation. The longitudinal phase space is then manipulated in the buncher and phase rotation section to reduce the beam momentum spread. Finally the transverse phase space is reduced in the cooling section.

The number of pions captured depends on the magnetic field strength, the shape of the tapering and the geometry of the shielding. To maximize the muons flux into the accelerator an optimization study is performed for these key concepts and the results are presented here.

OPTIMIZATION METHOD

The results presented are produced using G4beamline, a particle tracking program based on Geant4 [3]. A Hg-target is used with length $l = 30$ cm and radius $r = 0.5$
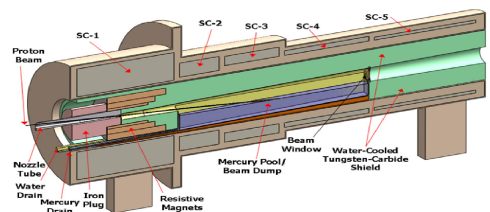
FIGURE 1. Baseline layout of the target and capture section of the NF. The proton beam is focused on the Hg-target to produce pions in a 20 T magnetic field made by superconducting solenoid magnets. The pions are then transported downstream towards the frond-end [2].

cm. The target center is placed at $z = -37.5$ cm and tilted an angle $\theta_T = 96.68$ mrad with respect to the z-axis. The impinging 8 GeV kinetic energy proton beam has an angle $\theta_{BT} = 30$ mrad with respect to the target axis at the center of the target ($z = -37.5$ cm). All these parameters are held constant for each setup.

The accelerator can only accelerate a fraction of the muons arriving from the front-end. To find this fraction a setup of the full front-end for G4beamline is used. The muon flux is counted at $z = 50$ m and at the end of the front-end (at $z = 271.1$ m). Then the emmitance calculation tool *ecalc9f* [4] is applied at the end of the frond-end to find the muons accepted for the accelerator, defined as *good muons*. G4beamline labels each of the particles in such a way that the momentum, position and time distribution can be traced back and found at 50 m for these good muons within the *acceptance cuts*. See table 1. This makes it possible to compare different capture systems by the particle flux at 50 m while being confident that the particles within the cuts have a high probability of being good muons. The results are compared with the capture section from Study 2A (ST2a) [2].

TABLE 1. Acceptance cuts at 50 m and the input parameter for the ecalc9f routine at 271.1 m. The acceptance cuts were found by using the survivors from the ecalc9f routine and finding their momentum, time and position distributions at 50 m.

Position (m)	p_z (MeV/c)	p_T (MeV/c)	t (ns)	r (mm)
50	100-300	< 50	160-240	< 200

Position (m)	p_z (MeV/c)	A_T (m rad)	A_L (m rad)	Input for ecalc9f
271.1	100-300	< 0.030	< 0.150	

Optimization without magnet shielding

First the magnetic field tapering for 5 different setups is studied, all without any magnet shielding. There is one variant of *13sol*, three variants of the *3sol* setup that is compared with the *ST2a* setup. The 3sol layout, figure 2, has 3 superconducting (SC)solenoid magnets. The large SC1 magnet will generate the high 20 T field with help from the normal resistive inner solenoids and SC3 generates a 1.5 T field. The SC2 generate fields that can be read from figure 3. The *13sol* setup has 13 SC
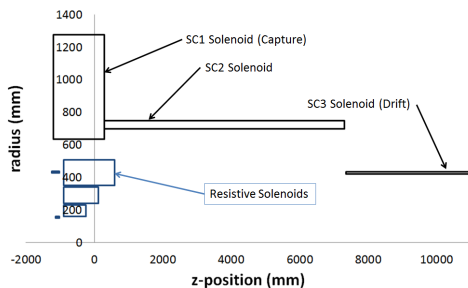

FIGURE 2. The 3sol solenoid magnet setup. The picture shows the upper half of a vertical cut of the solenoids. The black boxes are the superconducting solenoids and the blue boxes are the resistive solenoids. Here we have no magnet shielding.

solenoids and a long field tapering. The magnetic fields on axis can be seen in figure 3. The simulation stoped tracking any particle that hits the solenoids.

The results can be seen in figure 4. The 3sol_1 setup (28513 $\mu^{\pm}$) has the highest muon flux, an increase of 9% compared with the ST2a (26262 $\mu^{\pm}$).
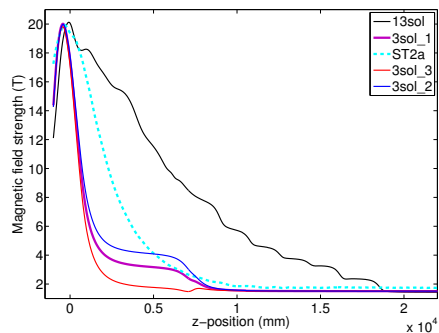
FIGURE 3. Magnetic field tapering for all the setups. The 3sol_1 setup is the thick purple line and the ST2a setup is the thick cyan dashed line.
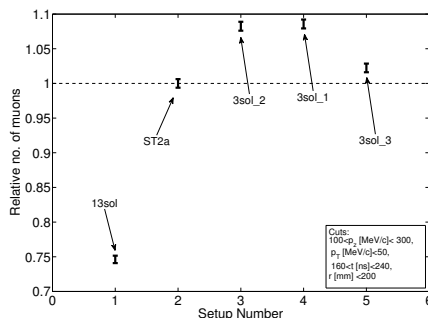
FIGURE 4. Relatice muon flux at 50 m, see figure 3. The 3sol_1 setup give the highest muon flux.

Optimization with magnet shielding

Shielding is needed to protect the magnets from radiation, the radius of the shielding is found as follows. The inner radius of the magnet shielding is calculated assuming an adiabatic tapering and conservation of magnetic flux $\Phi = \pi B R^2$. Where B and R are the magnetic field strength and the inner shielding radius, respectively. From flux conservation

$$\pi B_1 R_1^2 = \pi B_2 R_2^2, \qquad (1)$$

where the subscrips refer to different points along the tapering where the flux is conserved. This helps to calculate the inner shielding radius as a function of position along the z-axis, taking account of the field taper. The inner shielding radius in the ST2a setup is 7.5 cm in the 20 T field region around the target. Using equation 1, with $B_1 = 20T$, $R_1 = 7.5$ cm, $B_2^{ST2a} = 1.75$ T and

$B_2^{3sol} = 1.5$ T, the radii are found to be $R_2^{ST2a} = 25.4$ cm and $R_2^{3sol} = 27.4$ cm. In figure 5 there is the two different
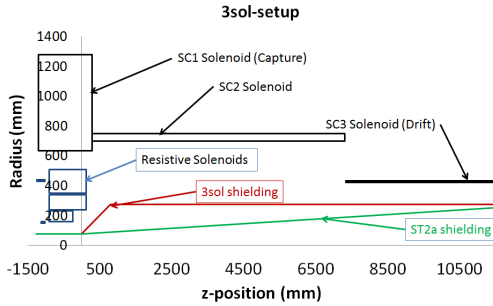
FIGURE 5. The 3sol solenoid magnet setup. The picture shows the upper half of a vertical cut of the solenoids. The black boxes are the superconducting solenoids and the blue boxes are the resistive solenoids. The shielding used in the ST2a is showed in green and the 3sol shielding is in red.

magnet shieldings, naming the new shielding made for the 3sol setup for *shielding3*. The shielding for SC1 is not changed, but for SC2 a quickly expanding shielding cone is prefered since the field tapering is shorter. With less shielding the magnet will be more exposed to radiation. Assuming that a low field SC2 magnet can have an increased inner radius the radiation exposure can be decreased.

Varying the SC1 magnet strength

The optimisation of the SC1 magnet strength was studied by varying the trength of the SC1 magnet from 10 T to 40 T while observing the muon flux. During this study the SC2 and SC3 magnetic field strengths are held constant at 1.5 T and the 3sol setup and shielding are used. The ST2a muon flux is used as normalization and the relative number of muons is shown in figure 6. Errorbars are statistical only, calculated as the square-root of the muon flux.

The muon flux graph flatens out around 25 T. We choose to set a maximum for SC1 at 20 T, taking into account the technical challenges of making a magnet producing a field higher than 20 T and the increased cost. The relative difference in muon flux between 20 and 25 T is 13%.
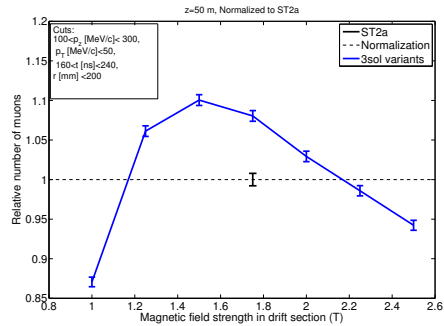
Varying the SC3 magnet strength

The magnet strength of SC2 is set equal to SC3, the magnet strength of SC3 (and therefore SC2) is then varied from 1 to 2.5 T. SC1 is at 20 T. Again we use
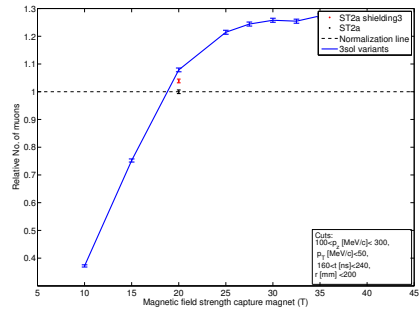
FIGURE 6. Relative muon flux at 50 m when varying the SC1 magnet strength from 10 to 40 T are shown in blue, normalized with the muon flux from the ST2a (shown in black). The red point is the ST2a setup with the 3sol shielding. All points include errorbars.

the ST2a muon flux as the normalization(see figure 7). The SC3 magnet should create a field of 1.5 T.

FIGURE 7. Relative muon fluxes when varying the SC3 magnet strength from 1 to 2.5 T are shown in blue, normalized with the muon flux from the ST2a (shown in black). Errorbars are statistical.

Varying the SC2 magnet strength

SC1 is set to 20 T and SC3 to 1.5 T and the magnet strength of SC2 is varied from 1.75 to 9 T. In figure 8, the results are normalized with the ST2a muon flux. The maximum is found when SC2 is at 4.8 T with an increase in particle flux of about 10 %. Going down to an even lower field is possible without a huge particle loss.

The momentum distributions for the ST2a and the 3sol, both with shielding3, are compared in figure 9. They are similar, with the 3sol having a slight advantage over the ST2a.
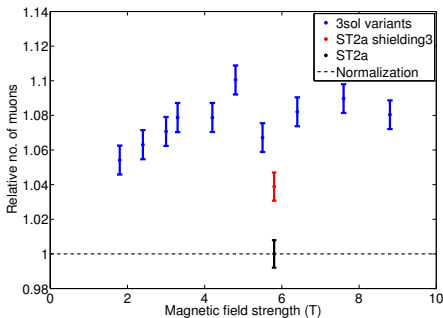
FIGURE 8. Relative muon flux when varying the SC2 magnet strength from 1.75-9 T are shown in blue, normalized with the muon flux from the ST2a (shown in black). The ST2a with shielding3 shown in red. Errorbars are statistical only.
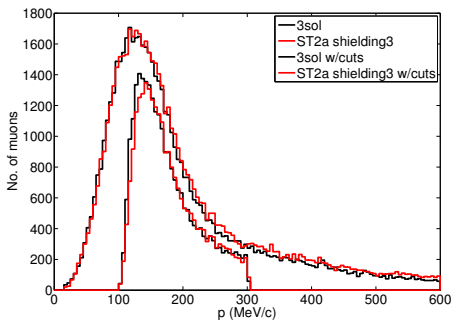
FIGURE 9. Muon momentum distribution for the ST2a and the 3sol setups shown in red and black, respectively. We can see that the distributions are similar and the 3sol captures a higher number of muons. The two upper lines show the momentum distribution without any cuts applied while the two lower lines show the distribtion with the acceptance cuts.

A study with FLUKA is done in order to compare the results with G4beamline. Table 2 shows some comparisons between the two monte-carlo simulation tools.

TABLE 2. Relative no. of total muons and the relative no. of muons within the acceptance cuts for the ST2a and the 3sol. Both have shielding3.

Setup	No cuts		w/cuts	
	G4BL	FLUKA	G4BL	FLUKA
ST2a shielding3	1.09	1.57	1.04	1.24
3sol	1.05	1.38	1.10	1.14

According to the G4beamline simulations, the 3sol setup is better than both the ST2a and the ST2a-shielding3. The results from FLUKA suggests that the

3sol is better than the ST2a and the ST2a-shielding3 is even better than the 3sol. However, reducing the shielding thinkness for the ST2a magnet layout may cause an increase in the radiation exposure to the magnets. For the 3sol the increased inner magnet radius means there can be more shielding between the beampipe and the magnets. FLUKA seems to be more sensitive to a change in shielding layout than G4beamline, increasing the muon flux with 24 % for the ST2a-shielding3.

Summary and outlook

The magnetic field tapering and the shielding layout for the Neutrino factory was studied. The study of the magnetic field tapering without any shielding, showed that a faster magnetic field tapering is a good alternative to the longer adiabatic tapering. The lower current in SC2 may allow this solenoid, expected to receive the peak of the radiation from the target, to have a larger radius thereby exposing it to less radiation.

When the magnetic field in SC3 is decreased, an increased shielding radius is needed to conserve the magnetic flux. A shortening of the magnetic field tapering, an increase of the shielding inner radius and a shortening of the cone length was done. Then the field strength was optimized in each of the three SC magnets, but varying the field in 1 magnet at a time. This altenative 3sol setup gives a higher yield compared to the ST2a setup, for both FLUKA and G4beamline.

A study of the energy deposition in the magnets to check if the magnets are properly shielded with the new shielding3 is needed. A study with the 30 cm mercury target replaced by, the baseline, full liquid mercury jet target included is needed.

ACKNOWLEDGMENTS

REFERENCES

1. S. Choubey, et al. (2011), bNL-96453-2011, CERN-ATS-2011-216, FERMILAB-PUB-11-581-APC, RAL-TR-2011-018.
2. R. Fernow, et al. (2004), mUC-NOTE-COOL_THEORY-296.
3. G4beamline, G4beamline web site (2012), URL http://www.muonsinc.com/muons3/G4beamline.
4. R. Fernow (2003), mUC-NOTE-COOL_THEORY-280.

A.2 Towards a Symmetric Momentum Distribution in the Muon Ionisation Cooling Experiment

Poster presentation at IPAC13, Shanghai, China [35].

Report

Towards a Symmetric Momentum Distribution in the Muon Ionisation Cooling Experiment

O.M. Hansen
Univ of Oslo, Oslo, Norway, CERN, Geneva, Switzerland
A. Blondel
Univ. of Geneva, Geneva, Switzerland
I. Efthymiopoulos
CERN, Geneva, Switzerland

Keywords: Circular and Linear Colliders, Muon, Neutrino

Abstract

The Muon Ionisation Cooling Experiment (MICE) is under development at Rutherford Appleton Labratory (UK). It is a proof-of-principle experiment for ionisation cooling, which is a prerequisite for a future Neutrino Factory (NF) or a Muon Collider. The muon beam will have a symmetrical momentum distribution in the cooling channel of theNF [1]. In the MICE beamline pions are captured by a quadrupole triplet, beam momentum is selected by dipole 1 (D1) before the beam traverses the decay solenoid. After the decay solenoid the beam momentum is selected by dipole 2 (D2), the beam is focused in two quadrupole triplets and characterised by time-of-flight (TOF) detectors TOF0 and TOF1 before entering the cooling channel. By doing a so-called D1-scan, where the optics parameters are scaled according to the upstream beam momentum, the purity and momentum distribution of the decay muons are changed. In this paper simulation results from G4Beamline (G4BL) [2] and data from MICE are presented and compared.

Presented at: IPAC13, 12-17 May 2013, Shanghai, China

Geneva, Switzerland
June, 2013

TOWARDS A SYMMETRIC MOMENTUM DISTRIBUTION IN THE MUON IONISATION COOLING EXPERIMENT

Ole Martin Hansen, University of Oslo, Oslo, Norway and CERN, Geneva, Switzerland
Alain Blondel, University of Geneva, Geneva, Switzerland
Ilias Efthymiopoulos, CERN, Geneva, Switzerland

Abstract

The Muon Ionisation Cooling Experiment (MICE) is under development at Rutherford Appleton Labratory (UK). It is a proof-of-principle experiment for ionisation cooling, which is a prerequisite for a future Neutrino Factory (NF) or a Muon Collider. The muon beam will have a symmetrical momentum distribution in the cooling channel of the NF [1]. In the MICE beamline pions are captured by a quadrupole triplet, beam momentum is selected by dipole 1 (D1) before the beam traverses the decay solenoid. After the decay solenoid the beam momentum is selected by dipole 2 (D2), the beam is focused in two quadrupole triplets and characterised by time-of-flight (TOF) detectors TOF0 and TOF1 before entering the cooling channel. By doing a so-called D1-scan, where the optics parameters are scaled according to the upstream beam momentum, the purity and momentum distribution of the decay muons are changed. In this paper simulation results from G4Beamline (G4BL) [2] and data from MICE are presented and compared.
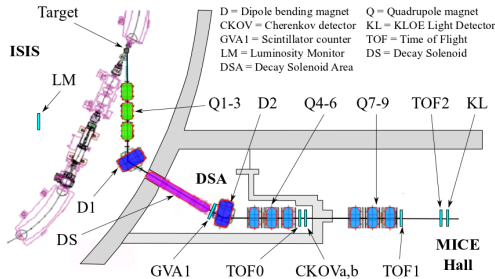
Figure 1: The MICE beamline at step 1.

INTRODUCTION

The short lifetime of muons demands cooling which is several times shorter than the decay time [3]. Ionisation cooling is generated as the muon beam enters and passes through a low-Z absorber in the MICE beam line, losing energy through ionisation [4]. The beam momentum is reduced in the transverse and the longitudinal direction and the longitudinal momentum is restored by acceleration. Ionisation cooling has been proposed for reducing the phase space volume of an intense muon beam for a NF and a Muon Collider. The change in normalised beam emittance ϵ_N in a medium is [5]:

$$\frac{d\epsilon_N}{dX} \approx -\frac{\epsilon_N}{\beta^2 E_\mu}\left\langle \frac{dE}{dX} \right\rangle + \frac{\beta_t(0.014GeV)^2}{2\beta^3 E_\mu m_\mu X_0}, \quad (1)$$

where X is the material thickness, X_0 is the radiation length of the medium, β is the velocity, β_t is the betatron function, E_μ is the muon energy and m_μ is the muon mass. The negative part gives emittance reduction through energy loss of beam particles and the positive part emittance increase through multiple scattering. It is therefore important that the energy loss is dominant to achieve cooling.

SYMMETRICAL MOMENTUM DISTRIBUTION

The MICE cooling channel is based on Feasibility study 2 (ST2)[1]. It consists of liquid hydrogen absorbers and accelerating cavities in a magnetic field. The muon momentum distribution of the beam used in ST2 is symmetrical, with a mean momentum of $\bar{p} = 207$ MeV/c and momentum standard deviation of $s_p = 28$ MeV/c, as shown in figure 2.
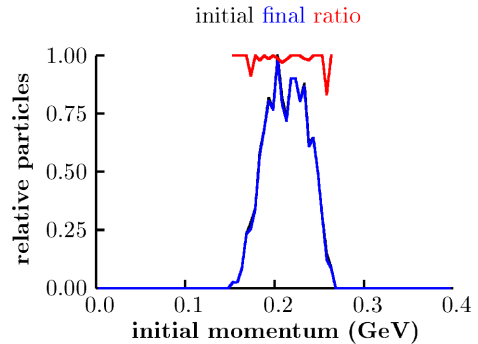

Figure 2: Momentum distribution of the ST2 muon beam [1].

The D1-scan is performed by holding the magnet strengths of D2 and the two quadrupole triplets Q4-Q6 and Q7-Q9 constant, while varying the strengths of the capture quadrupoles Q1-Q3, D1 and the decay solenoid proportionally to the reference pion momentum p_{D1}.

The standard 6 mm - 200 MeV/c beam is used, the magnet currents can be found in [6]. The conversion from currents to fields are done by interpolating values from a magnet data sheet, it can be found in the MICE documentation [7]. D2 is set to select muons with momentum $p = 238$ MeV/c.

The skewness

$$s = \frac{\frac{1}{n}\sum_{i=1}^{n}(x_i - \bar{x})^3}{(\frac{1}{n}\sum_{i=1}^{n}(x_i - \bar{x})^2)^{\frac{3}{2}}}, \quad (2)$$

Table 1: Skewness for the positive and the negative beam calculated from the simulations. The positive/negative beam is on the left/right side of the slash.

p_{D1} +/-(MeV/c)	300/310	325/339	375/375	408/408
s	-0.82/-0.40	-0.13/0.17	0.51/0.45	0.65/0.68

is used to indicate how symmetrical the momentum distribution is. A perfectly symmetric distribution will have $s = 0$. The distribution is negative skew if the left tail is more pronounced than the right, and positive skew if the opposite [8].

SIMULATIONS

D1-scan simulations have been performed for beams of both signs. The skewness is observed to decrease when the ratio between the pion momentum at D1 and muon momentum at D2 p_{D1}/p_{D2} decrease and at some point become 0, such that the beam becomes symmetrical. The momentum distributions after the decay solenoid for $p_{D1} = 310$ and $p_{D1} = 408$ MeV/c are shown in figure 3 and the pion peaks are where one should expect them to be. To get a muon beam with a low pion contamination $p_{D2} < p_{D1}$ can be set to select the muons that decay backwards in the pion reference frame.
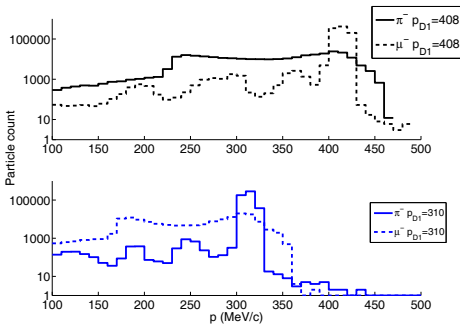

Figure 3: The momentum distribution after the decay solenoid, for the negative beam, with $p_{D1} = 310$ MeV/c and $p_{D1} = 408$ MeV/c.

The skewness values vs. p_{D1} for both signs beams are shown in the table. According to these simulations one would expect the beams to be close to symmetrical when $p_{D1} \approx 325$ MeV/c.

Some pion contamination is expected in the beam, according to the simulations the pion contamination is low in the interval $p_{D1} \in [300, 425]$, shown in figure 4. The worst case is approximately 2.7 %, if one selects the most pessimistic value of the error bar from $p_{D1} = 300$.

The muon momentum distribution from MICE data and G4BL at TOF1 are compared in figure 5 and the agreement is fairly good.
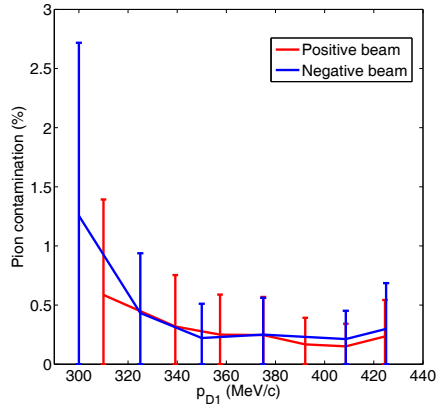
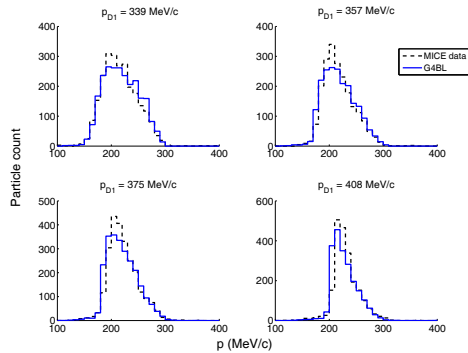Figure 4: Pion contamination vs. p_{D1} at TOF1, error bars are statistical only.

Figure 5: Momentum ditribution vs p_{D1} at TOF1. The distribution get more symmetrical when p_{D1} is lowered, the variance increase and the mean momentum is lowered.

SIMULATIONS AND MICE DATA

The statistics from the MICE data is low and it only exists for the negative beam at the moment, these results are therefore only preliminary. Higher statistics runs are expected to be taken and analysed in the near future. However, the statistics should be high enough to give estimates for the beam mean, skewness and standard deviation with reasonable error calculations.

Cuts are applied to eliminate the longest tails of the momentum distributions, a cut on the particle count was used, eliminating 2.5 % of the particles on each tail. Simulations have been normalised to the MICE data by integration. The cuts are especially important for the higher momenta, which have longer tails.

When analysing the MICE data the momentum distributions are approximated from the time-of-flight between TOF0 and TOF1, removing all particles in the TOF electron
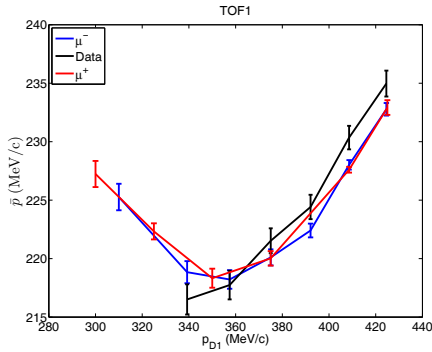
Figure 6: The mean momentum at TOF1 as a function of p_{D1}. The ST2 muon beam has $\bar{p} = 207$ MeV/c.

peak and assuming the rest of the particles to be muons.

The mean momentum at detector TOF1 lies in the interval $p \in [215, 235]$ MeV/c when varing p_{D1}, as shown in figure 6.

The standard deviation of the momentum distribution is shown in figure 7 and the maximum distribution width is found at 325 MeV/c for the simulations, and falls when going to higher momenta. For the MICE data the maximum is found at the lowest p_{D1}.
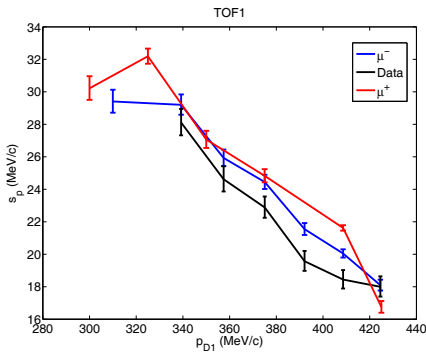

Figure 7: The momentum standard deviation vs p_{D1} at TOF1. The ST2 beam has $s_p = 28$ MeV/c. The error bars correspond to 95 % confidence intervals.

When calculating the skewness of the distribution the cuts are especially important. It is sensitive to outliers and therefore they are eliminated from distribution. The most symmetric distribution is found when $p_{D1} = 330$ MeV/c and for the MICE data the lowest data point has the lowest skewness.

CONCLUSION

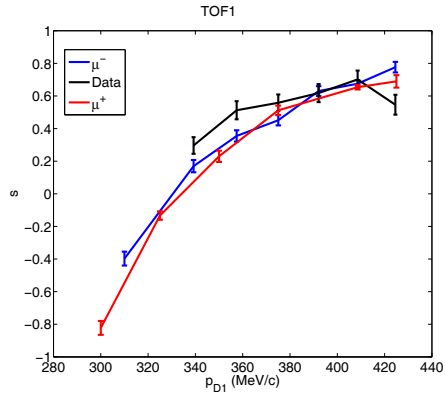If one argues that the MICE data can be extrapolated to agree with the simulations, then a symmetrical momentum

Figure 8: The momentum skewness vs. p_{D1}. The beam is symmetrical when $s = 0$. The error bars are only statistical.

distribution can be found when D1 is set to select pions with $p_{D1} \approx 325$ MeV/c, the standard deviation of that beam is $s_p \approx 30$ MeV/c. The mean momentum is $\bar{p} \approx 225$ MeV/c, but the mean momentum will decrease further between TOF1 and the cooling section, further downstream, where some detector material and a diffuser will be placed.

ACKNOWLEDGMENT

REFERENCES

[1] S. Ozaki, R. Palmer, M. Zisman, and J. Gallardo, (2001), "Feasibility Study-II of a Muon-Based Neutrino Source", BNL-52623.

[2] T. Roberts, (2012), "G4beamline", http://g4beamline.muonsinc.com.

[3] A. Skrinsky and V. Parkhomchuk, "Methods of cooling beams of charged particles", Accelerator Science and technology 1 (2008), 237-257.

[4] M. Bogomilov et al., JINST 7 (2012) P05009

[5] D. Neuffer, "Multi-TeV muon colliders", AIP Conf.Proc. 156 (1987), 201-208.

[6] M. A. Rayner, (2011), The development of a novel technique for characterizing the MICE muon beam and demonstrating its suitability for a muon cooling measurement, PhD-thesis.

[7] http://mice.iit.edu/bl/Documentation/index_doc.html.

[8] E. Weisstein, "Skewness." From MathWorld–A Wolfram Web Resource.

A.3   A Simplified Magnetic Field Tapering and Target Optimisation for the Neutrino Factory Capture System

Poster presentation at IPAC13, Shanghai, China [17].

A SIMPLIFIED MAGNETIC FIELD TAPERING AND TARGET OPTIMISATION FOR THE NEUTRINO FACTORY CAPTURE SYSTEM

I. Efthymiopoulos, S. Gilardoni, O. M. Hansen*, G. Prior †, CERN, Geneva, Switzerland.

Abstract

In a Neutrino Factory, a 4 MW proton beam with a kinetic energy between 5 and 15 GeV interacts with a free floating liquid mercury jet target in order to produce pions which after capturing are let to decay forming a muon beam, input to the front-end accelerator system of the facility. The baseline capturing layout consists of a series of normal and superconducting solenoids producing a tapered magnetic field from 20 T, near the target, down to 1.5 T at the entrance of the drift pion decay section. An alternative layout is studied, where the magnetic field is rapidly squeezed from 20 T to 1.5 T using only three solenoids. This new layout showed to produce similar, and even slightly better performance than the baseline, having the additional advantage of being simpler and could potentially be made more robust to radiation. In this paper we report on further optimisation studies taking into account the beam interaction path length in the mercury jet and shape fluctuations of the jet.

INTRODUCTION

The Neutrino Factory (NF) [1] is designed to provide intense high-energy neutrino and anti-neutrino beams, ν_e, $\overline{\nu}_\mu$ ($\overline{\nu}_e$, ν_μ) from the decay of stored μ^+ (or μ^-). To probe the very sensitive oscillation parameters, the neutrino mass hierarchy and CP-violation, a high flux of neutrinos, and therefore muons is required. In the baseline design of the NF a total of 10^{21} muon decays per year is envisaged. The muons are produced as tertiary particles from pion decays, in turn produced in a sufficiently heavy target bombarded by an intense 4 MW proton beam. In the baseline design the target is a free-floating liquid-mercury jet target operating in a solenoid-focusing pion-capture channel. This is followed by a solenoidal transport channel in which the pions decay to muons. The emerging muon beam is then bunched, and rotated in phase space to produce a beam with small energy spread. In the last stage of the front-end systems the muon beam is "cooled", i.e. reduced in the transverse dimensions, to match the injection parameters of the accelerators.

The pion-capture channel consists of a series of superconducting solenoids with varying strength starting from 20 T around the target centre to 1.5 T in the constant-field transport decay channel about 15 m downstream. The smooth changing strength of the solenoids or "tapering", each at slightly lower field than the previous, exchanges transverse for longitudinal momentum thus gradually focus the pions and produce a small divergence beam, input to the

decay pipe and front-end systems [2]. The design of these solenoid magnets presents severe engineering challenges as most of the 4 MW beam power is dissipated in this region around the target. An internal shield composed of high-Z material is included around the target to protect the superconducting solenoids that extends all the way down to the muon front-end.

THE 3-SOL LAYOUT

The 3 solenoid layout and magnetic field tapering that was proposed [3] showed to preserve and even give slightly better muon yield than the baseline design. In this, the magnetic field rapidly decreases from 20 T around the target to 1.5 T in two steps using two sets of solenoids - therefore the naming 3SOL.
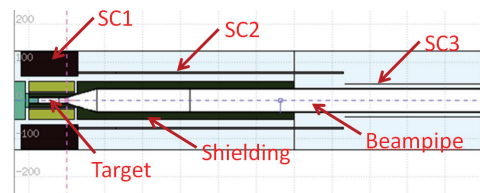

Figure 1: The 3SOL layout around the NF target. SC1, SC2 and SC3 are superconducting solenoids. The beampipe is the white region in the center, the radius is $r_{b1} = 75$ mm in the 20 T region around the target, then in the conical region increases to $r_{b2} = 274$ mm.
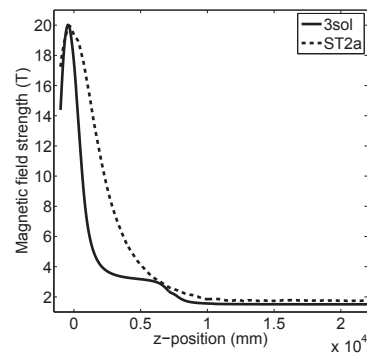

Figure 2: The magnetic field variation in the 3SOL and standard layout.

Compared to the baseline layout, the 3SOL offers the advantage of having the solenoids at much lower current in

* o.hansen@cern.ch, also at University of Oslo, Norway
† presently at University of Canterbury, Christchurch, New Zealand

01 Circular and Linear Colliders

A09 Muon Accelerators and Neutrino Factories

particular for the region just downstream the target where most of the energy is deposited. The low current for SC2 would potentially allow a larger radius solenoid thus reducing the effect of radiation. From initial studies the performance of the new layout seems comparable and better than the baseline ST2a design [3]. A complete engineering study needs to be done to fully validate this solution and quantify potential cost and complexity savings.

OPTIMISATION STUDIES

The interaction region of the target where the secondary pions are produced can be considered as the particle source therefore the optics of the focusing system with the solenoids should match to the entrance of the decay volume and the accelerator front-end. The effective interaction region is determined by the entry and exit points and directions of the primary beam and the mercury jet both affected by the high magnetic field of the 20 T solenoid. The trajectory of the beam can be chosen to vary the proton path-length inside the target, and therefore the secondary particle production yield, or make the interaction region close to the central axis, i.e. closer to the focal point of the optics system of the solenoids. From hydrodynamics studies of the mercury jet as it traverses the high gradient magnetic field of the central solenoid a quadrupole effect may be present [4] that can distort the jet to an elliptical shape. In the next section the result on further optimisation studies addressing these effects for the 3SOL layout are reported. The studies are done using the G4beamline (G4BL) simulation tool [5]. The input proton beam has a kinetic energy of 8 GeV and $\sigma = 1.5$ mm.
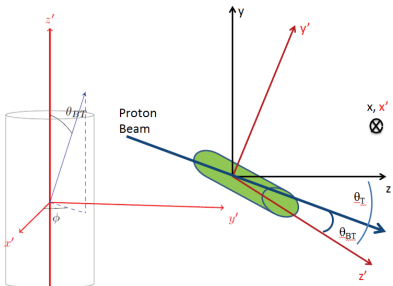
Figure 3: Target and beam. Left: the angle definitions of θ_{BT} and ϕ in the target reference frame. Right:the target reference frame rotation of θ_T around the x-axis. The centre of the target is defined to be in the (0,0,-375) mm.

Elliptical Hg-jet

The distorted jet was simulated by increasing the height and squeezing the width, compared to the circular jet with radius $r = 5$ mm, to form an elliptically shaped jet. The jet height increase has been reported to be $\sim 1.15 \times r$ in a 15 T magnetic field [4]. Here it's assumed that the height increases to $1.2 \times r$ when in a 20 T field. The major semi-

axis of the ellipse should be $a = 6$ mm, therefore and from conservation of mass for the jet, the minor semi-axis is calculated to be $b \sim 4.2$ mm.
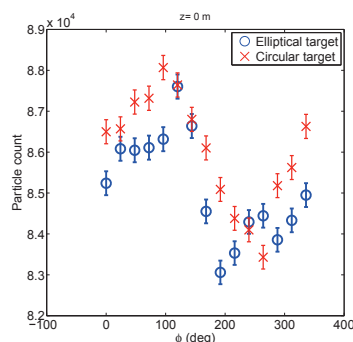
Figure 4: Muon and pion count vs. the azimuth angle ϕ.

To approximate the elliptically shaped jet in G4BL, three cylinders were used: one at the center with radius $r_1 = b$ mm and two placed at $y \pm 2$ mm with $r_2 = 3.8$ mm. The cylinders were then tilted by $\theta_T = 96.68$ mrad. The polar angle between the beam and target is fixed to $\theta_{BT} = 30$ mrad while the azimuth angle is varied from $\phi \in [0, 360]$ degrees, in steps of 24, using the target reference frame, see Fig. 3. The results are presented in Fig. 4 where the maximum particle count variation is 5.5 % for both cases and the elliptical jet has a lower count, on average. The comparisons of particle count are done downstream of the jet in the plane at position $z = 0$ mm, or at +37.5 cm from its centre. The error bars are only statistical.

Particle production center

The jet is now circular. Figure 5 shows the distribution of the y-position of each individual proton interaction point in the jet. The black dashed line shows the case for $\phi = 0$ from the previous section, for the circular jet. The distribution peak, or the particle production center, is off-centered in the positive y-direction. The secondary particles are therefore produced in the upper part of the beampipe, i.e. out of the focal centre therefore more particles will be lost from scraping in the shielding. The distribution peak was therefore shifted towards the center by making the proton beam enter the jet at a lower y-position. Then the secondary particles will have a smaller radial distribution, thus potentially increasing the muon yield at the front-end. In addition it makes the spreading of the energy deposition more even such that the upper part of the shielding doesn't get the peak of the radiation.

In Fig. 5 the y-distribution is skewed and non-gaussian, the median was therefore chosen over the mean to indicate the central tendency. The results are shown in Fig. 6, where the highest count is found when the beam's median is -4mm.
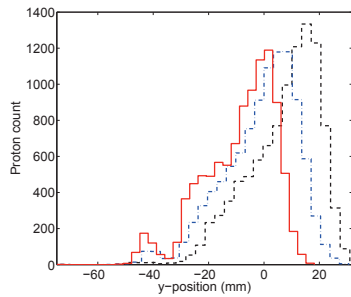
Figure 5: The y-distribution of the interaction between the proton beam and the jet. The black dashed line has median 8.6 mm, the blue dash-dotted line has median 1.25 mm and the red line median -6.1 mm which can be found in Fig. 6.
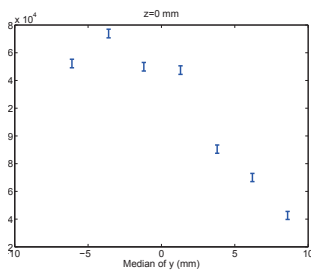

Figure 6: Median of y vs. particle production.

Interaction region length

To increase the interaction region length (pathlength) the angle θ_{BT} is varied from 20 to 35 mrad, while keeping the optimal median value ≈ -4 mm, found in the previous section. The particle count increases for a longer pathlength, the highest average pathlength found was 100.8 mm and the particle count is then increased another 6.8 % giving a total increase of 17.3 % compared to the maximum from Fig. 4.

In summary the production of the secondary particles has been centered in the beampipe and the pathlength was increased. The particle flux has this far been found in the plane at $z = 0$ mm. To make sure the optimisation increases the output of the front-end, the particle flux is now found at $z = 50$ m, where acceptance cuts are applied as described in [3]. The results are shown in Fig. 8 and compared to the ST2a layout [6]. The non-optimised 3SOL and ST2a both used the the maximum value from Fig. 4.

CONCLUSION

Optimisation studies of the proton beam interaction with the mercury jet target have been performed in the 3SOL layout. Changing the jet shape from a cylinder to an ellipse
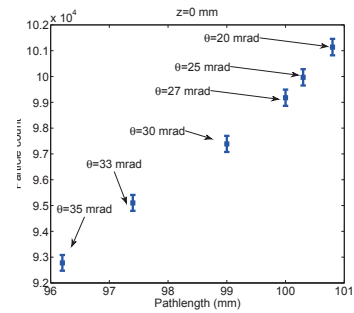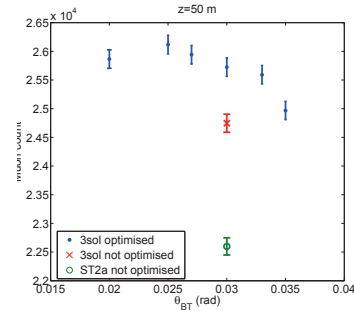

Figure 7: Pathlength vs. particle production.

Figure 8: The optimised angle, θ_{BT}, compared to the non-optimised 3SOL and the non-optimised ST2a.

alters the particle production slightly, a decrease of a few percent is expected.

It is found that the muon yield could be maximised if the secondary particles a produced in the center of the beampipe. The optimal angle between beam and target was found to be $\theta_{BT} = 25$ mrad to get the longest path-length and therefore the highest particle flux. Combining these optimisations give an increased muon count of 5.5% (16%) compared to the non-optimised 3SOL (ST2a).

REFERENCES

[1] S. Choubey, et al. (2011), BNL-96453-2011, CERN-ATS-2011-216, FERMILAB-PUB-11-581-APC, RAL-TR-2011-018.

[2] M. Green *et al.*, ICFA workshop on beam dynamics, vol 372, AIP conference proceedings, AIP, 1996.

[3] O. M. Hansen, I. Efthymiopoulos, (2012), "Optimizing the capture section of the Neutrino factory", NuFact12 conference preceedings, AIP.

[4] H. J. Park, (2009), Experimental Investigation of Magnetohydrodynamic Flow for An Intense Proton Target, Dissertation presentation, Stony Brook University.

[5] T. Roberts (2012), G4beamline, http://g4beamline.muonsinc.com.

[6] R. Fernow, et al. (2004), MUC-NOTE-COOL_THEORY-296.

01 Circular and Linear Colliders

A09 Muon Accelerators and Neutrino Factories